Investigations into the Electronic States of 2D Quantum Material WTe_2

Elliott Runburg

A dissertation

submitted in partial fulfillment of the

requirements for the degree of

Doctor of Philosophy

University of Washington

2024

Reading Committee:

David H. Cobden, Chair

Matthew Yankowitz

Mark Rudner

Program Authorized to Offer Degree:

Physics

University of Washington

Abstract

Investigations into the Electronic States of 2D Quantum Material WTe_2

Elliott Runburg

Chair of the Supervisory Committee:
Prof. David H. Cobden
Physics

Quantum materials are those whose properties cannot be explained without invoking quantum mechanics. This broad class of materials includes superconductors, topological insulators, magnets, and Weyl semimetals. These materials are of great research interest to both better understand nature as well as to harness their unique properties for further technological development. With the successful isolation of graphene, the field of 2D materials was born. The restriction in dimension changes the physics of the electrons, in addition to allowing for increased control over the material properties using electrostatic gates, whose effectiveness is highly limited in 3D.

This thesis focuses on the electronic properties of the 2D quantum material WTe_2. Following a brief background on the history of WTe_2, I will discuss our studies of the spin-axis of

the edge states of monolayer WTe_2, demonstrating the helical nature of these states and thus confirming that WTe_2 is a 2D topological insulator. Next, I will report on our experiments to study the edge states at millikelvin temperatures, where the linear conductance of the edges freezes out. From there, I will report on new data from high-quality crystals grown from the so-called “horizontal flux” technique. I will show how WTe_2 has a stronger superconducting state than previously reported, showing strong density dependence while having a critical temperature larger than 1.5 K. We also report unambiguous evidence of the presence of Shubnikov-de Haas oscillations in monolayer WTe_2.

TABLE OF CONTENTS

LIST OF FIGURES

LIST OF TABLES

ACKNOWLEDGEMENTS

First and foremost, I want to express my gratitude to my parents for their unconditional love and support, both during my graduate studies and throughout my entire upbringing. They have always supported me in my many endeavors, making plentiful sacrifices along the way in ways that were both visible and invisible to me then and now. Despite their preference for me to stay nearby for graduate school, they were very understanding and supportive of my decision to move across the country and start my adult life in Seattle. These past 7 years of graduate school have been challenging for me in a litany of ways, between classes, COVID, and the rigors of academic research, but they have always been there to lend an ear and give advice when I needed it, and I struggle to imagine where I would be today without them.

Next, I would like to thank my advisor, Prof. David Cobden. I joined Dave's lab shortly after joining the University and have not looked back since. Dave is a great advisor, and his kindness, patience, scientific curiosity, wit, and humor shaped my experience through graduate school in incredibly positive ways. The process of research can be slow and arduous, as I've experienced during my Ph.D., but Dave was understanding and supportive when things would not go as planned or I made mistakes. I have a deep appreciation for the way Dave runs his lab.

Of course, I couldn't have made it through the day-to-day grind of lab work without having a great team of people working alongside me, from the previous generation of graduate students and postdocs who taught me all the experimental techniques in the lab, to the current group who make the lab a pleasant and comfortable place to work. Specifically, I'd like to thank (in no particular order) postdoc Tauno Palomaki, graduate students Paul Nguyen, Joshua Kahn, Wenjin Zhao, Bosong Sun, Arnab Manna, Eric Lester, Gianluca Delgado, and Ruhee Nirodi. Additionally, I'd be remiss to not thank some of the undergraduates that have come through the lab. They helped both by doing the dirty work of 2D materials research as well as expressing an eagerness to be involved in science that was refreshing, and pushed me to become a better scientific communicator and mentor. To name a few, I'd like to thank Emily Toph, Andrew Barkley, Yuva Belarbia, Shreya Pekety, and Viru Sharma for their positive contributions to the lab.

Our lab does not operate in a vacuum in the 2D materials space in the department, and the presence and impact of this larger community of condensed matter experiment made this journey much easier. From our crystal growers- Paul Malinowski, Jonathan DeStefano, and Chaowei Hu in Prof. Jiun-Haw Chu's lab- to the many members both present and past in both Prof. Xiaodong Xu's and Prof. Matthew Yankowitz's lab, having good people around to collaborate, commiserate, and socialize with in my subfield is a blessing I do not take for granted.

Graduate school also introduced me to my roommates and best friends in Seattle, and I feel so grateful for having met such amazing people while navigating through a Ph.D., a pandemic, and the start of real, independent adult life. I'd like to especially thank Kade Cicchella, Andy Goldschmidt, Katie Goldschmidt, Christian Pederson, Jared Canright, and Anthony Ciavarella for their friendship. While we will be taking different paths through life from here, I know we will remain friends forever.

I would also like to thank the rest of my committee: Matthew Yankowitz, Mark Rudner, Subhadeep Gupta, Ting Cao, and Jess Werk. I have nothing but positive things to say about my experiences with everyone on my committee, and I'm lucky to have been in a supportive environment.

Finally, I'd like to thank many other friends and family, both here in Seattle, back in the Midwest, and elsewhere. Truly, I could not have gotten to, or through, this chapter without my entire community, who have shaped the person I am today and the person I continue to strive to become going forward.

DEDICATION

To my parents, Jan Bonavia and Gregg Runburg

Chapter 1. Introduction

1.1 PHYSICS IN TWO DIMENSIONS

A two-dimensional electron gas (2DEG) is an electronic system in which the electrons are free to move in two dimensions but are confined in the third. These systems have been of interest for decades; the metal-oxide-semiconductor field-effect-transistor (MOSFET) and the high-electron-mobility transistor (HEMT) are two important realizations of a 2DEG.

The MOSFET is one of the most important technological breakthroughs of the modern day, as it is the basis for all the microprocessors that run our world. MOSFETs are composed of a metal, oxide insulator, and semiconductor. By holding the semiconductor at ground and applying a voltage to the gate, charges will accumulate on the surface of the semiconductor facing the oxide. Application of an electric field across the oxide will bend the energy bands of the semiconductor as a function of real space; given a large enough field, the band will cross the Fermi energy and there will be a non-zero mobile charge population restricted to a small physical space, creating a 2DEG.

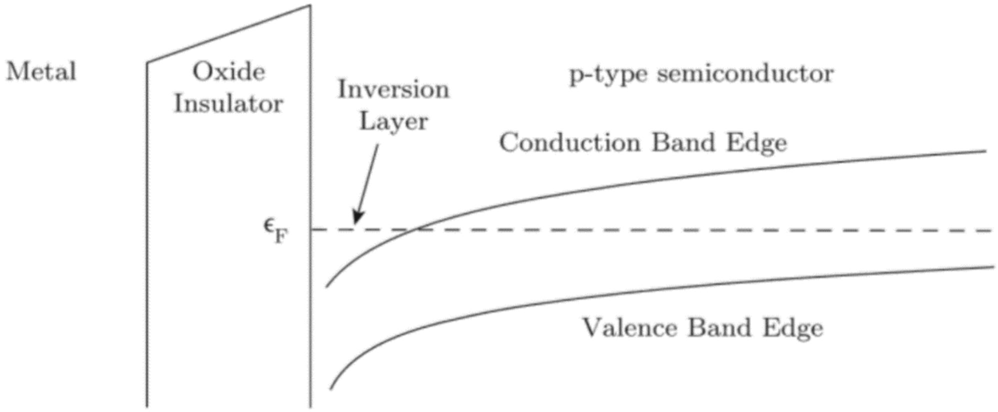

Figure 1.1. Band diagram of a MOSFET as a function of real-space along the horizontal axis. Reproduced from [1].

The archetypal HEMT is a GaAs/AlGaAs heterostructure quantum well. These quantum well heterostructures are made from the two component semiconducting materials typically grown via molecular beam epitaxy [2]. When *n*-doped AlGaAs is brought into contact with GaAs charges will be transferred into the GaAs, forming a PN junction that creates the quantum well, with potentially high mobility [3,4]. Through careful engineering, the Fermi level can be aligned within this band, creating a 2DEG. Similar systems, such as $SrTiO_3$/$LaAlO_3$ and HgTe quantum wells have been extensively studied and have proven to be fruitful platforms for studying novel 2D electronic behavior [5,6].

1.1.1 *Graphene*

The field of 2D electronic systems was revolutionized in 2004 when Geim and Novoselov first isolated monolayer graphene via scotch tape exfoliation [7]. Graphene is a monolayer of graphite, a layered material with a hexagonal crystal structure made entirely of carbon. Their discovery spawned the field of 2D materials. 2D materials are crystals that have strong covalent bonds within one plane of the crystal, with weaker van der Waals forces adhering the planes together in the 3D crystal. Through mechanical exfoliation and the standard dry-transfer technique, these materials can be isolated and stacked onto each other to produce new and highly tunable electronic systems [8,9]. Graphene is a semimetal and alone hosts a plethora of interesting electronic properties, and is the archetypal platform to study a 2DEG.

1.1.2 *Layered 2D materials*

Beyond graphene, there are a host of other 2D materials with a large variety of electronic properties. Hexagonal boron nitride (hBN) is a honeycomb lattice of alternative boron and nitrogen sites that is a wide bandgap material and the archetypal dielectric for 2D heterostructures [10]. One family of materials of particular interest to this thesis is the transition metal dichalcogenides. These crystals have the crystal formula MX_2, where M is a metal atom (i.e. Mo or W) and X is a chalcogen atom (i.e. S or Se). Materials in this family run the gamut of electronic phases: there are direct-gap semiconductors (MoS_2, WSe_2, e.g.) whose optical properties have generated much interest [11–15], superconductors ($NbSe_2$) [16], and charge density wave materials (TaS_2) [17,18]. Other crystals have been shown to be magnetic, such as CrI_3 [19] and Fe_3GeTe_2 [20]. The ability to form heterostructures by stacking different materials in a vertical configuration provides an entirely new set of tools to manipulate and study fundamental physics. Furthermore, the ability to electrostatic gate the 2DEG provides an immense advantage to 2D materials over previous 2DEGs such as HEMTs, where the charge density is defined upon creation of the quantum well.

1.1.3 *Topology in two dimensions*

Topology is a mathematical field that classifies systems by their closeness, and ability to be continuously deformed into each other. The common example of a donut being transformed into a coffee mug highlights this idea of closeness: a chosen region on one side of the donut cannot be deformed to include within it points on the other side of the donut without closing the hole. In fact, the transformation of the donut into a mug will map the original region into a new region that contains exclusively the transformed points contained within the original region. In electronic systems, topological order is encoded in the electronic bands [21].

In 2005, Kane and Mele introduced a Z_2 topological invariant to describe the quantum spin Hall (QSH) phase, a time-reversal symmetric electronic state with a bulk band gap and gapless helical edge states, extending the TKNN classification of quantum Hall states to time-reversal symmetric systems [22,23]. They showed that adding a spin-orbit term into graphene's

Hamiltonian gives the QSH phase. The topological nature of the phase results in it being insensitive to disorder, as the gap and edge modes cannot be destroyed without changing the topological order. These systems have drawn great interest in their potential to be used for more reliable quantum computation [24,25].

1.1.4 *Excitonic insulators*

It has been predicted that Coulomb interactions between free electron and hole carriers in a crystal could result in spontaneous formation of a bound pair between the two, known as an exciton [26,27]. While electrons and holes individually obey fermion statistics, excitons have bosonic statistics, meaning they can form a condensate. This charge-neutral condensate is an insulating state, known as an excitonic insulator, which has the effect of opening a gap at the Fermi surface of a semimetal in a manner analogous to the formation of a BCS gap in a superconductor. While many systems have been hypothesized as candidates to host an excitonic insulating state, they present challenges to detect experimentally, as they are charge neutral [28–30].

1.2 WTE$_2$

The work of this thesis focuses on the electronic properties of WTe$_2$, another crystal in the family of transition metal dichalcogenides. Unlike the aforementioned semiconducting TMDs that share the hexagonal 2H crystal structure with graphene, WTe$_2$ has 1T’ crystal structure, a distorted rhombohedral lattice. This is a low-symmetry lattice, hosting only a screw axis along the *x*-axis and a mirror plane in the *y*-*z* plane, along with an inversion center in odd-numbered layer stackings (Figure 1.2).

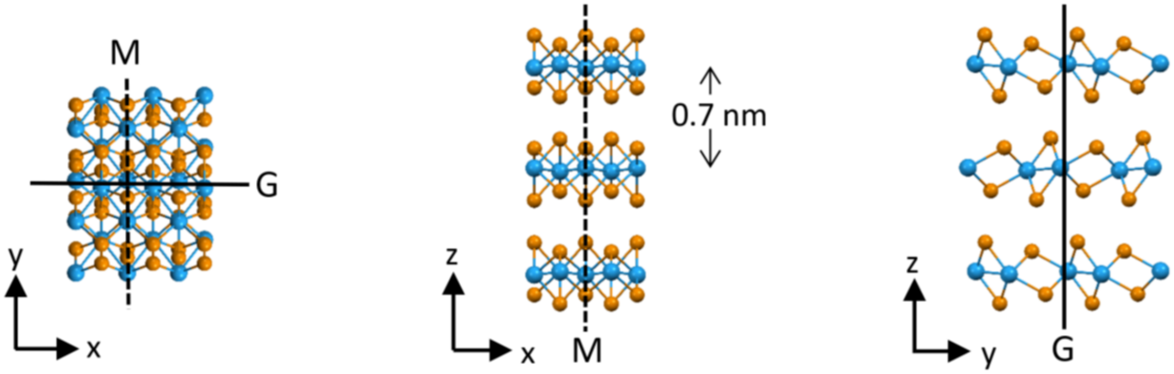

Figure 1.2. Crystal structure of WTe_2. Mirror plane denoted by *M* and glide plane (screw axis) denoted by *G*. Reproduced from reference [31].

Particular interest in WTe_2 was sparked in 2014 when Qian et. al. predicted that monolayer WTe_2 could host the quantum spin Hall insulator phase if it had a gap separating the conduction and valence bands. The heavy W and Te atoms have strong spin-orbit coupling, required for the band inversion necessary to form topological bands. While Qian et. al. predicted WTe_2 could host topological states, their calculations suggested that WTe_2 had finite band overlap [32]. Preliminary ARPES measurements done on monolayer WTe_2 were unable to conclusively determine if there was an energy separation between the conduction and valence bands, though recent spectroscopy suggests a ~45 meV gap [33,34]. In the following subsections, I will summarize some foundational work on 2D WTe_2 done by our group and others, though that is by no means the extent of interesting results published on this system; bulk WTe_2 is a type-II Weyl semimetal [35] that has large Fermi arcs [36,37] and was found to have large, non-saturating magnetoresistance [38]. Various nonlinear Hall effects have been proposed and reported in few-layer WTe_2 [39,40], and higher-order topological order has been observed via hinge states in thicker WTe_2 [41,42].

1.2.1 *Monolayer WTe_2*

The prediction of potential topological states drove interest in studying monolayer WTe_2, and in 2017 our group published transport results on monolayer WTe_2 demonstrating that it did have a gap and hosted edge states, and the following description comes from results published in Fei, et. al. [43].

Figure 1.3a shows transport data for monolayer device MW1. Conductance data is plotted versus gate voltage for a variety of temperatures. Below 100 K, the conductance reaches a finite minimum value over a range of gate voltage, which grows upon further cooling. The conductance minimum is shy of the quantized conductance value of $2\frac{e^2}{h}$ predicted for the helical edge modes of a quantum spin Hall insulator. In order to study the origin of this conductance plateau further, subsequent devices were fabricated with so-called ‘pincer’ electrode geometries as shown in Figure 1.3b. The flake is aligned so the edge of the flake intersects all three electrodes, with the heads of the two pincer electrodes separated a short distance from each other through the bulk of the flake. A voltage is applied between the two large pincer electrodes, while the middle electrode is alternatively floated and grounded. When the middle electrode is floated, a similar conductance trace is retrieved as in the previous device, showing an approximately constant conductance plateau over a range of gating. However, when the middle contact is grounded, the conductance instead goes to zero over the range of gate where the plateau existed. The difference in conductance levels between these two measurement configurations is approximately a constant value over all gate voltages, indicating that this conductance is coming from a channel confined to the physical boundary of the flake that is conductive for all available doping regimes.

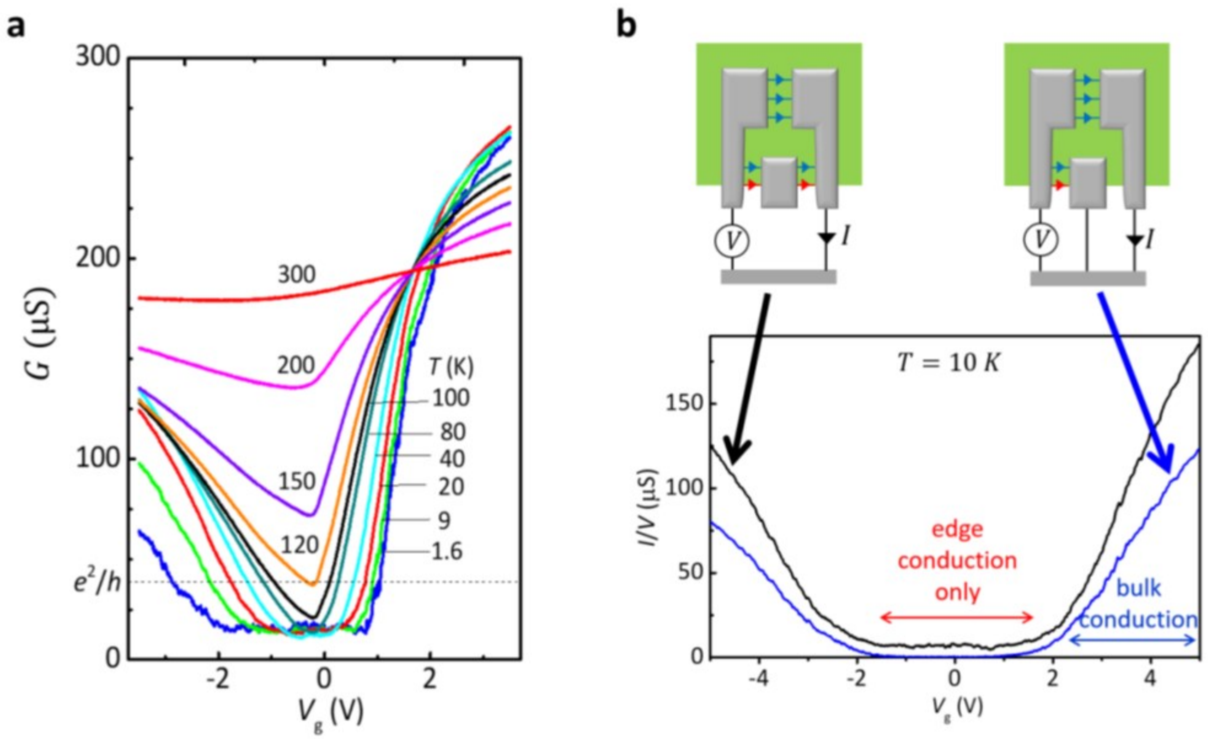

Figure 1.3. Edge transport of monolayer WTe_2. **a**, Gate dependence of the conductance for a variety of temperatures. Below 100 K a plateau in conductance forms, indicative of edge conduction. **b**, Schematic of the ‘pincer’ geometry. Conductance data at 10 K is shown for the alternate cases of floating and grounding the middle contact, confirming the current as being confined to the edge. Reproduced from reference [43].

Helical edge states, such as those belonging to a quantum spin Hall insulator, should have particular sensitivity to in-plane magnetic field, while the bulk states should be insensitive to the field in this configuration. Data was published in the same work showing the difference in behavior with a 14 T in-plane field applied versus no field applied, again showing a suppression of the plateau over the available gate range.

The lack of quantization of the edge conduction persisted for all devices and edges reported in Fei, et. al. [43]. In 2018, Wu et. al. published further transport data on monolayer WTe_2

measured against the edge length that connected the electrodes. They posit that their conductance values trend towards the quantized value of $2\frac{e^2}{h}$ for edge lengths <100 nm [44].

While these two studies give evidence that WTe_2 is a topological insulator, the helical nature of the edge states was not conclusively proven. In Chapter 2 of this thesis, I will present measurements on the angular anisotropy of the magnetoconductance. We identify the spin axis of the edge states, proving their helical nature, and confirming that monolayer WTe_2 hosts the quantum spin Hall state.

While the topological nature of monolayer WTe_2 drove initial interest in the material, further studies showed that it hosts other interesting electronic properties. In 2018, two different reports showed that at millikelvin temperatures, monolayer WTe_2 undergoes a metal-to-superconductor transition. Reports agreed on a critical electron doping level of $\sim 5\times10^{12}$ cm^{-2} while estimates of the critical temperature ranged from ~400-900 mK, with these two quantities being highly dependent on one another [45,46]. Another report showed signatures of the vortex Nernst effect in the superconducting state [47]. In Chapter 4, I will report on further studies into the nature of the superconducting state.

The nature of the insulating state has also proven to be of particular interest. In 2022, two reports were published together providing evidence of formation of equilibrium excitons, suggesting monolayer WTe_2 is an excitonic insulator [48,49].

In Sun et. al., conductance as a function of gate voltage was measured. The insulating state of monolayer WTe_2 has peculiar properties. Upon cooling to 100 K, the conductivity develops a sharp V-shaped dependence on the electrostatic doping, while the chemical potential μ exhibits a $\sim$43 meV step at charge neutrality. This behavior cannot be understood in a standard picture of independent electrons with given band structure and disorder. The authors calculated electron n

and hole p densities for a single-particle model chosen to match the low-temperature behavior of μ and the corresponding conductance calculated simply using $\sigma = ne\mu_e + pe\mu_h$ with fixed mobilities μ_e and μ_h (bottom, blue dotted line). A much better match to the measurements (black line) is obtained if we assume all minority carrier are bound as excitons at density $n_x = \min(n, p)$, so that $\sigma = (n - n_x)e\mu_e + (p - n_x)e\mu_h$, (Figure 1.4d) [49].

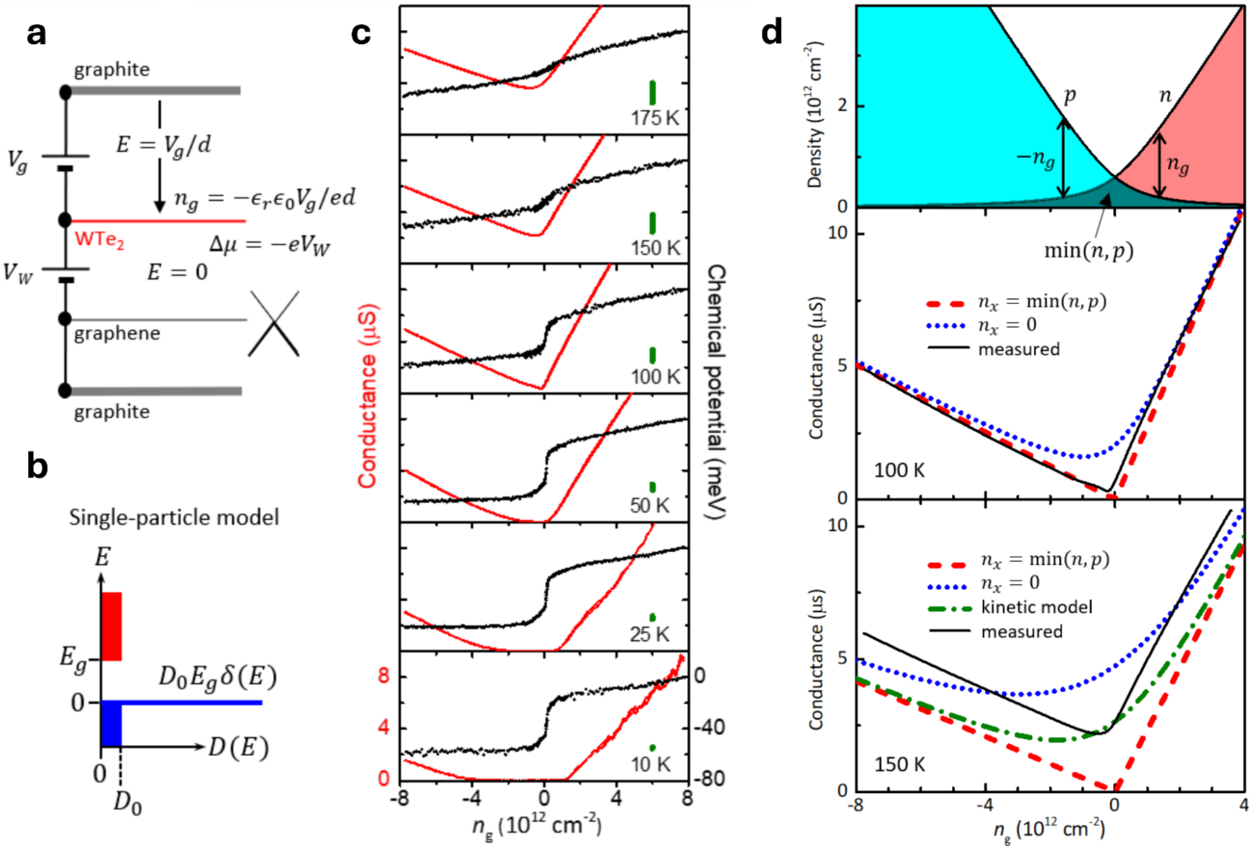

Figure 1.4. Evidence of equilibrium excitons in monolayer WTe$_2$. **a**, Experimental scheme used to measure the chemical potential. **b**, Experimentally-derived density of states. **c**, Conductance data (red) and chemical potential (black) at a variety of temperatures. **d**, Calculated n and p carrier densities for temperatures of 100 K and 150 K. The best match for the conductance features observed at 100 K come from calculating only the excess carriers of the dominant carrier type at each doping level (red dashed line). Content reproduced from [49].

1.2.2 *Bilayer WTe_2: a ferroelectric metal*

Unlike its monolayer form, bilayer WTe_2 is topologically trivial and does not have edge states. Bilayer hosts an insulating state similar to monolayer, as well as having an insulator-to-metal transition upon sufficient electron doping. The stacked form does not have an inversion center, and as such permits a polar axis. In 2018 Fei et. al. reported the observation of ferroelectric switching in bilayer and trilayer WTe_2 [50]. In a bulk metal, free electrons in the crystal will screen out external electric fields from the bulk of the material, making polarization switching in a metal nearly impossible. In two dimensions, the screening of the electric field by each layer can be small enough to allow for penetration of the field and thus ferroelectric switching. Reproduced in Figure 1.5 is conductance data as a function of gate voltage which shows hysteresis upon reversing the sweep direction, evidence of a ferroelectric state. By replacing one graphite gate with a graphene layer, the strength of the ferroelectric polarization can be measured through transport signatures in the graphene, confirming the out-of-plane polarization.

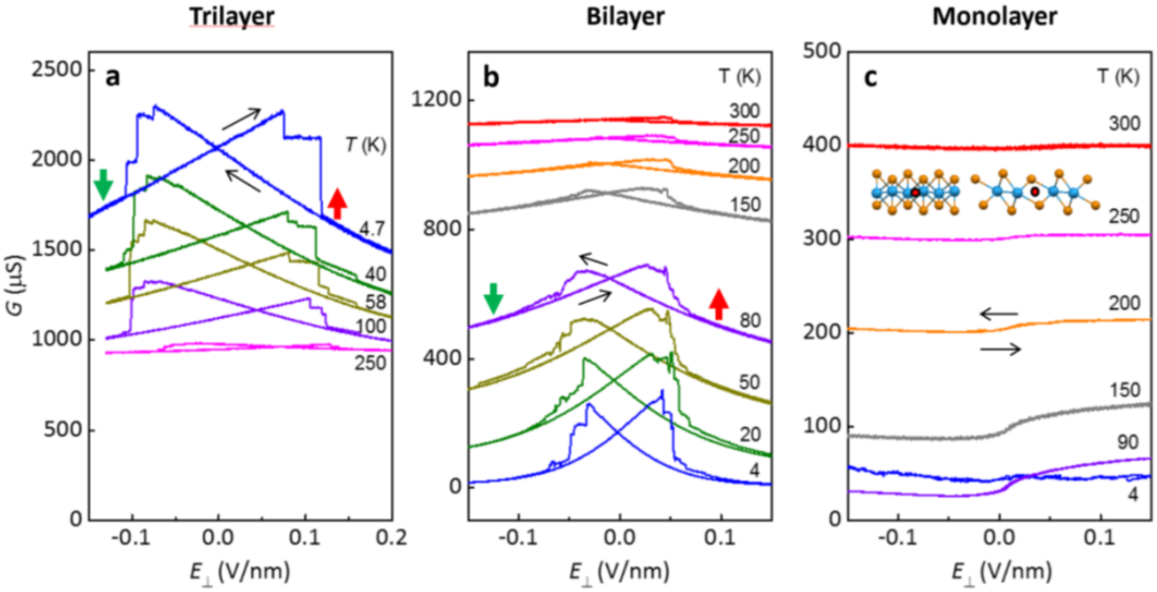

Figure 1.5. Ferroelectric switching of multilayer WTe_2. Trilayer (**a**) and bilayer (**b**) show hysteresis upon reversing of the sweep direction, while monolayer (**c**) does not. Reproduced from [50].

1.3 OUTLINE AND SUMMARY

The emergence of 2D materials provides a rich playground for exploring and studying novel electronic phenomena in order to better understand the physical world around us and to foster widespread future technological applications. This thesis focuses on the electronic properties of one seemingly endlessly interesting 2D material, tungsten ditelluride.

In Chapter 2, I will discuss the results of our experiments studying the spin axis of the edge states of monolayer WTe_2. We measure the angular anisotropy of the magnetic field dependence of the edge states and from these measurements are able to identify a spin axis of the electrons, which confirms their helical nature. We develop a theoretical model of the system to explain the particular magnetic response from the edges in both the linear and nonlinear cases.

In the following chapter, I will present work done to study the edge states of WTe_2 at millikelvin temperatures, in a regime when the linear conductance of the edge has frozen out. We study the mesoscopic dependence of the edge as a function of gate voltage and demonstrate that the nonlinear conductance at millikelvin temperatures displays a similar angular anisotropy of the magnetic response as in the linear regime.

In Chapter 4, I present new results on the superconducting state of WTe_2. With new, higher-quality crystals, we observe much different behavior in the superconducting state than has previously been reported. We observe a much smaller critical density for the onset of superconductivity, a dramatic density dependence on the critical field and temperature, and much higher critical temperature than previously seen. Additionally, we conclusively establish the existence of Shubnikov-de Haas oscillations in the metallic state of WTe_2 in both the electron- and hole-doped regimes, and see metallicity in the hole conduction.

Finally, in Chapter 5, I report on some intriguing measurements done on bilayer WTe_2 along with measurements done on WTe_2 coupled to an oxide substrate, namely strontium titanate. These measurements demonstrate that there is still much to be learned in this system in the future.

Chapter 2. Determination of the spin axis in quantum spin Hall insulator monolayer WTe_2

As covered previously, monolayer WTe_2 supports edge conduction, consistent with the presence of non-trivial topology. However, this fact alone is not sufficient to show that WTe_2 is a topological insulator: in two dimensions, a topological insulator will host the quantum spin Hall effect, in which the edge modes are helical. This chapter will explore evidence that the edge states in monolayer WTe_2 are indeed helical by examining their spin character as reported in Zhao, W.; **Runburg, E.**, *et al*. Determination of the Spin Axis in Quantum Spin Hall Insulator Candidate Monolayer WTe_2. *Phys. Rev. X.* **11**, 041034 (2021) [51], along with additional theoretical support published in Chen, Y,; Zhao, W.; **Runburg, E.**, *et al.* Magnetotransport on quantum spin Hall edge coupled to bulk midgap states. *Phys. Rev. B.* **8**, 085436 (2023) [52], and Chen, Y.; Quaresima, G.; Zhao, W.; **Runburg, E.**, *et al.* Magnetochiral anisotropy on a quantum spin Hall edge, (in preparation) [53].

2.1 EXPERIMENTAL TECHNIQUES

The natural way to investigate the spin character of the edge states is through the application of a magnetic field. Through the use of a PPMS fitted with a two-axis sample rotator, we are able to study the edge conductance as a function of the magnitude and angular orientation of the magnetic field at temperatures down to 2 K. We would like to study the magnetic anisotropy of the edge relative to the edge orientation and the crystal axes. For this, we employ two other experimental techniques: microwave impedance microscopy, or MIM for short, and Raman spectroscopy.

2.1.1 *Microwave impedance microscopy*

Microwave impedance microscopy is a near-field scanning probe technique in which a metallic tip is rastered near the surface to study the local complex permittivity of a sample. A microwave signal is generated and applied to the tip. The tip emits the microwave signal to the sample, and measures the system's reflectance, which leads to the inference of the local conductivity. By scanning the tip across the surface of the sample, it generates a real-space map of the sample conductivity [54].

This technique is powerful in studying WTe_2. While the WTe_2 is gated into its bulk insulating regime, the only conductive features of the device will be the contacts and any edges. A MIM image of a monolayer WTe_2 device is shown in Figure 2.1. We can see the Pt contacts lit up brightly, along with bright lines running across and around the device where there are edges. This allows us to know how the edges are oriented in space relative to the contacts, and through Raman spectroscopy, the crystal axes. Additionally, MIM allows us to probe for the existence of cracks within the crystal that permit edge channels connecting contacts where we don't expect there to be edges based on the optical image [55].

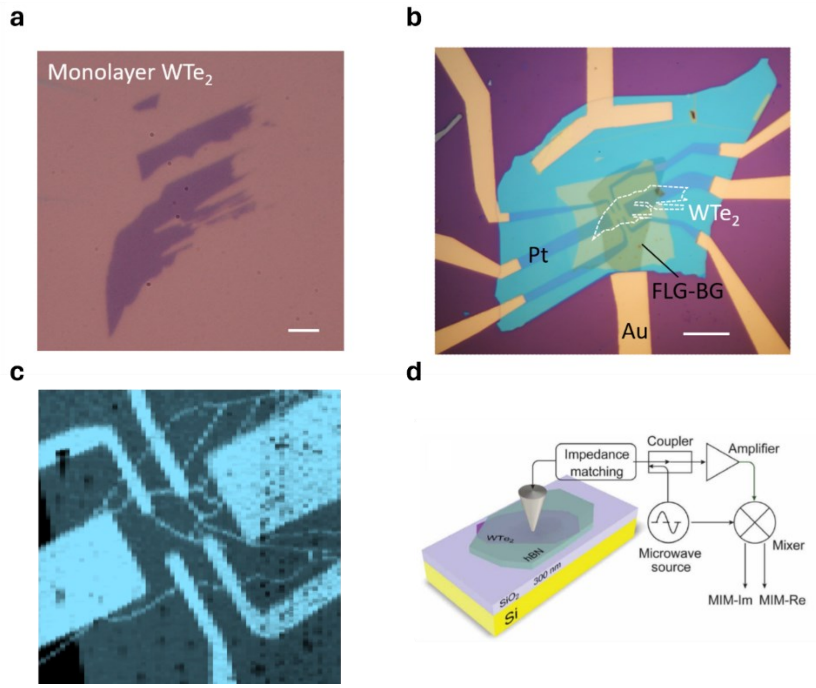

Figure 2.1. MIM on device MW5. **a**, Optical image of the monolayer WTe_2 flake on SiO_2 used to make the device. **b**, Optical image of the device. The WTe_2 flake is outlined in white for clarity. **c**, MIM image of the device, zoomed in around the central channel. We can see bright lines representing the conducting edges around the boundary of the flake, in addition to internal cracks providing other conducting edges between contacts. **d**, Schematic of the MIM experimental procedure.

2.1.2 *Raman spectroscopy*

Raman spectroscopy is a technique used to study the vibrational modes, or phonons, of a system. Here, we use it to infer the orientation of the crystal axes of our monolayer WTe_2 devices. In 2016 Kim et. al. studied the Raman spectrum of WTe_2 accompanied by in-situ TEM imaging of the crystals [56]. They found that polarization dependence of peak P11 is sensitive to the direction of the crystal axes; namely, that the signal is peaked along the *x*-axis (perpendicular to the mirror plane) of WTe_2.

To study the magnetic anisotropy of the WTe_2 edge conductance, we fabricate monolayer devices with a bottom graphite gate, thin (~7 nm) Pt contacts to the WTe_2, and a top encapsulating hBN without a gate, as the presence of a gate would screen the MIM signal from the WTe_2. We send our devices to our collaborator at the University of California, Riverside, Prof. Yongtao Cui and his group for MIM measurements. We perform polarized Raman spectroscopy measurements locally, in collaboration with Prof. Xiaodong Xu's lab. The Raman spectroscopy was performed in vacuum at room temperature. A He-Ne laser, with a wavelength of 632.8 nm, was focused down to a ~2 μm spot. For thick WTe_2, a laser power of 1 mW was used along with an integration time of 30 seconds, while thinner flakes were measured with 150 μW and integrated for 3 minutes. To resolve polarization dependence, a linear polarizer and a half-wave plate were placed before the objective. The Raman spectrum was taken on both the monolayer device as well as local bulk flakes, identified optically as having been exfoliated from the same bulk crystal. By comparing the polarization dependence of the two flakes, the orientation of the crystal axes can be determined, as shown in Figure 2.2.

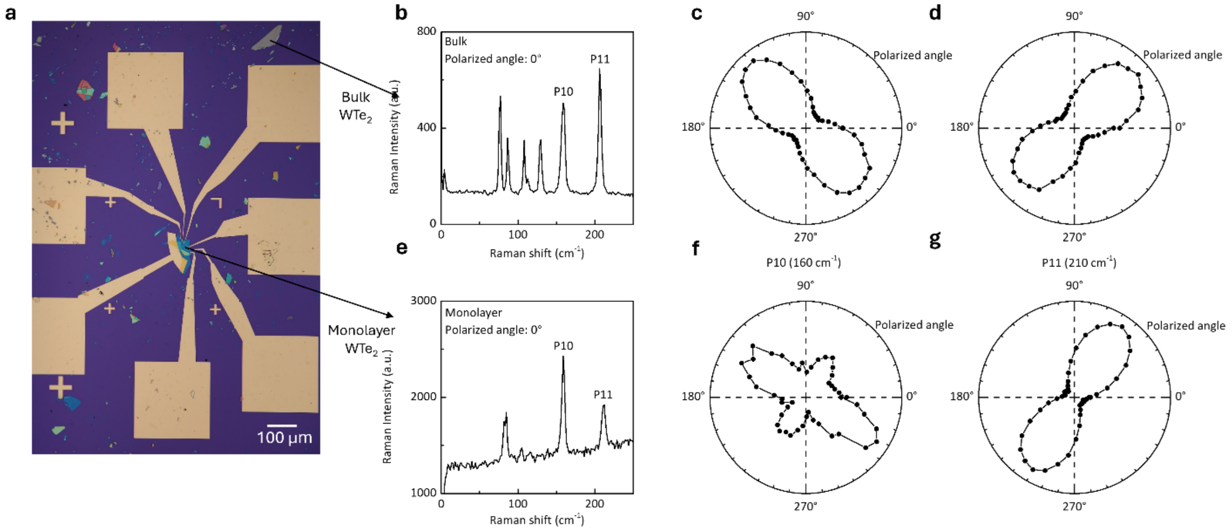

Figure 2.2. Raman spectroscopy on device MW7. **a**, Optical image of the monolayer WTe_2 device. A nearby bulk WTe_2 flake was identified from the exfoliation, in addition to the monolayer

in the device, for Raman to be performed on. **b-d**, Raman spectroscopy on the bulk flake. **b** shows the spectrum with peaks P10 and P11 identified, while **c** and **d** show the polarization dependence of peaks P10 and P11, respectively. **e-g**, Raman spectroscopy on the monolayer flake. The intensity of the Raman signal for P11 is smallest along the x-axis and largest along the y-axis.

2.2 ANGULAR ANISOTROPY OF THE EDGE MAGNETORESISTANCE

We measure our devices in a constant magnetic field, using a two-axis rotator to change the angle of our sample relative to the field. We define our angles θ and φ relative to the crystal axes of the WTe_2 as shown in Figure 2.3. We cool our device down to 4 K and choose a gate voltage such that the bulk is insulating. We choose to measure between contacts that we can identify through MIM as having only one (preferably straight) edge connecting the contact pair.

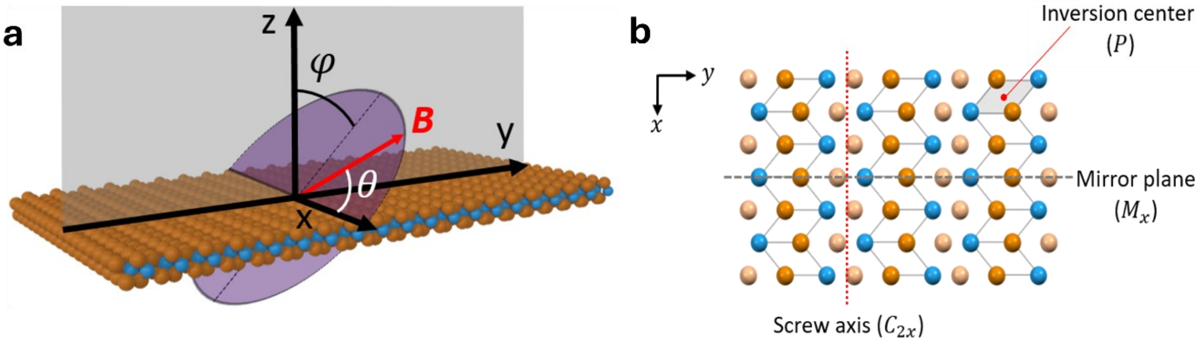

Figure 2.3. Illustration of coordinate choice. **a**, Crystal axes with angles θ and φ drawn. x-axis is chosen as our polar angle in these coordinates. **b**, Schematic of monolayer WTe_2 crystal structure from the positive z-axis, with the crystal symmetries noted.

In Figure 2.4a we show data taken on MW5 at $V_g = -2.7$ V with $B = 3$ T. We fix the value of φ and sweep θ through 360°. We observe that, for each value of φ, the conductance is maximum when B lies in the mirror plane, and the overall conductance is maximized when φ is tilted 40° from the z-axis. We measure the φ dependence in the mirror plane for a variety of contact pairs with edges in different orientations, and observe a similar angular dependence, as shown in Figure 2.4b. We label this angle, $\theta = 90°$ in the mirror plane and $\varphi = 40°$ from the z-axis, as $\boldsymbol{d}_{so}$.

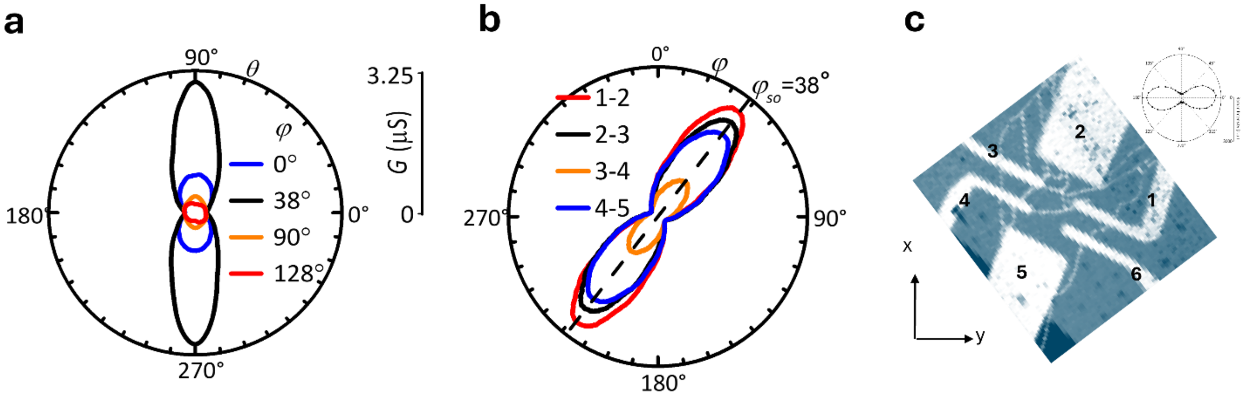

Figure 2.4. Angular dependence of the conductance. **a**, Conductance data taken for fixed values of φ with θ swept. **b**, Field is set into the mirror plane, i.e. $\theta = 90°$, and φ is swept for different contact pairs. The angle of φ that maximizes the conductance is the same for each pair. **c**, MIM image of device MW7 with the contacts used in **b** labelled. The axes indicate the crystal axes, with the polarized Raman spectrum inset.

We consider the symmetries of monolayer WTe_2 to explain the orientation of $\boldsymbol{d}_{so}$. Monolayer WTe_2 is a low-symmetry system, having a mirror plane in the *y*-*z* plane (as shown in Figure 2.3b) as well as having a screw axis along the *x*-axis, running along the Te chains. The crystal symmetries thus restrict the spin axis to the mirror plane, but do not constrict it within the mirror plane; the *z*-axis is not a special direction. In terms of the coordinates we choose to describe the system, the mirror symmetry can be written as $G(90° + \theta, \varphi) = G(90° - \theta, \varphi)$. Additionally, Onsager symmetry requires that $G(\theta, \varphi) = G(\theta + 180°, \varphi)$. The observed angular anisotropy of the edge conductance respects both symmetries.

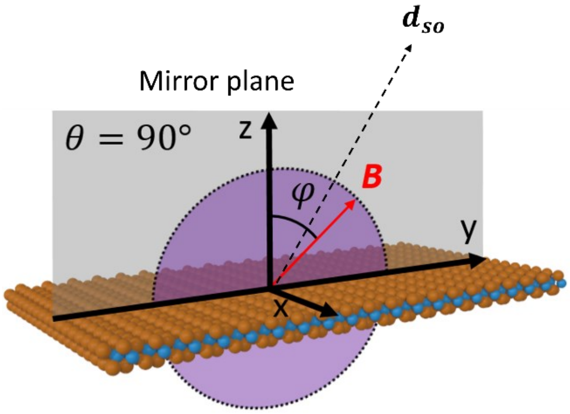

Figure 2.5. Schematic drawing the orientation of $\boldsymbol{d}_{\mathrm{so}}$ in our coordinates, relative to the crystal axes.

2.2.1 *Rigidity of the spin-axis*

We measure multiple monolayer devices in this same way, made at different times and grown with different batches of crystal. Images of these devices are shown in Figure 2.6. We observe a similar angular anisotropy of the conductance for each device. Beneath each device image is a plot of the conductance versus θ at different values of φ. The value of φ that maximizes the conductance is listed for each device. The shape, length and orientation relative to the crystal axes changes dramatically between devices and edges, and yet the angle $\boldsymbol{d}_{so}$ remains approximately the same. We might expect that the specifics of the edge may matter, since the edge should break the spatial symmetry of the crystal. However, since it does not, we infer that the edge spin orientation is inherited from the bulk band structure.

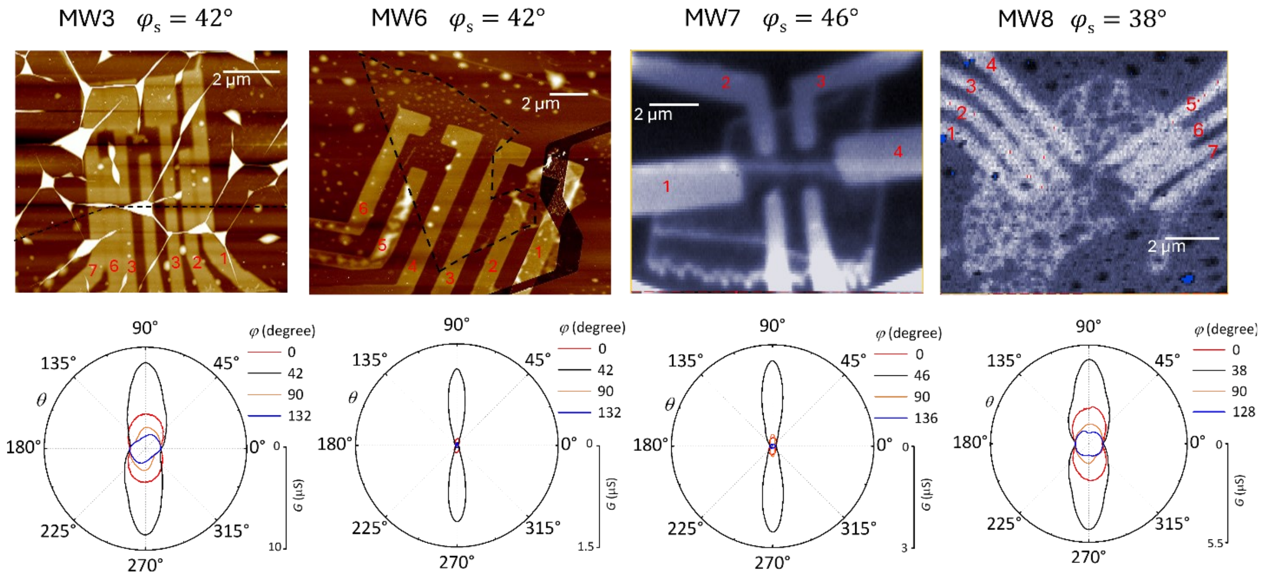

Figure 2.6. List of devices on which $\boldsymbol{d}_{\mathrm{so}}$ was measured. The value of $\boldsymbol{d}_{\mathrm{so}}$ is similar from device-to-device, independent of crystal batch or device quality.

Table 2.1. Details of devices for which the angular anisotropy was measured

Device label	WTe_2 layers	Top hBN (nm)	Bottom hBN (nm)	C_g (mF/m^2)
MW3	1	11.4	14	2.53
MW5	1	16	36	0.98
MW6	1	8	22	1.61
MW7	1	12	8	4.43
MW8	1	22	17	2.08
BW7	2	8	25	1.42

We measure the dependence of the edge anisotropy on gate voltage. At zero field, we observe significant mesoscopic modulation of the edge conductance with respect to gate voltage. Here, we set the back gate voltage V_g and sweep φ in the mirror plane with a constant magnitude magnetic field. We plot the results for three devices in Figure 2.7. We see little sensitivity of $\boldsymbol{d}_{so}$ to the gate voltage, varying by only $\pm 1°$.

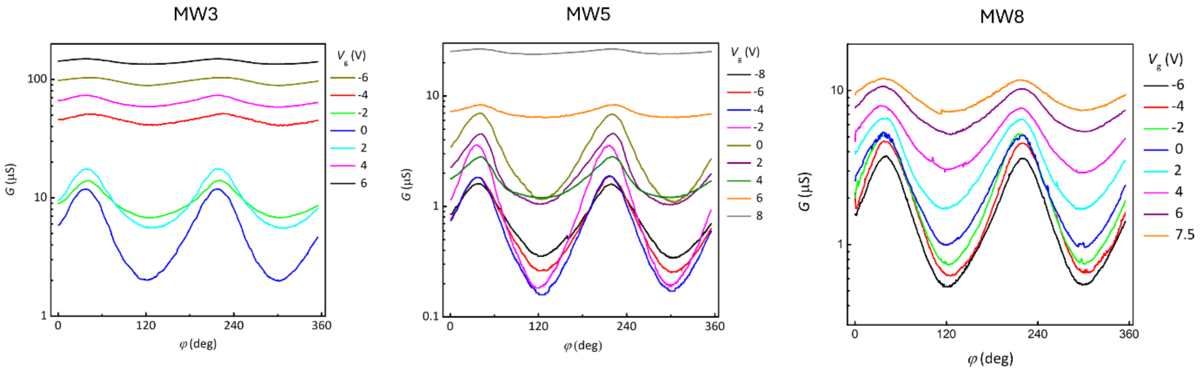

Figure 2.7. Gate dependence of φ_{so} for devices MW3, MW5, and MW8. We observe slight variation in the location of the conductance maxima of around $\pm 1°$.

The anisotropy of conductance is also measured at different temperatures. The bulk of monolayer WTe$_2$ is insulating under 100 K, though the QSH state exists even above these temperatures. In Figure 2.8a we show the effects of cooling on G. We see some weak angular anisotropy at 140 K, where the bulk conductance is dominant. Upon cooling, there is an overall reduction in the conductance. Along $\boldsymbol{d}_{so}$, at $\varphi = 40°$, we see a steady drop in conductance until ~50 K, at which conductance remains approximately constant upon further cooling. However, perpendicular to $\boldsymbol{d}_{so}$, around $\varphi = \varphi_s + 90°$, we observe a precipitous drop in conductance with decreasing temperature. The temperature dependence of the conductance along $\varphi = \varphi_s$ and $\varphi = \varphi_s + 90°$ is plotted in Fig Figure 2.8b. We note here that the minima and maxima are not separated by exactly 90°, but instead closer to ~85°. We understand this by considering the g-tensor of the edge states, which is not constrained by any symmetry. We find that the minimum value, φ_m, ranges from 83° to 90° between devices and contact pairs, consistent with g depending on microscopic details of the edge. However, the small variation of $\boldsymbol{d}_{so}$, together with the fact that φ_m is close to 90° implies that g can be treated as a scalar to a first approximation.

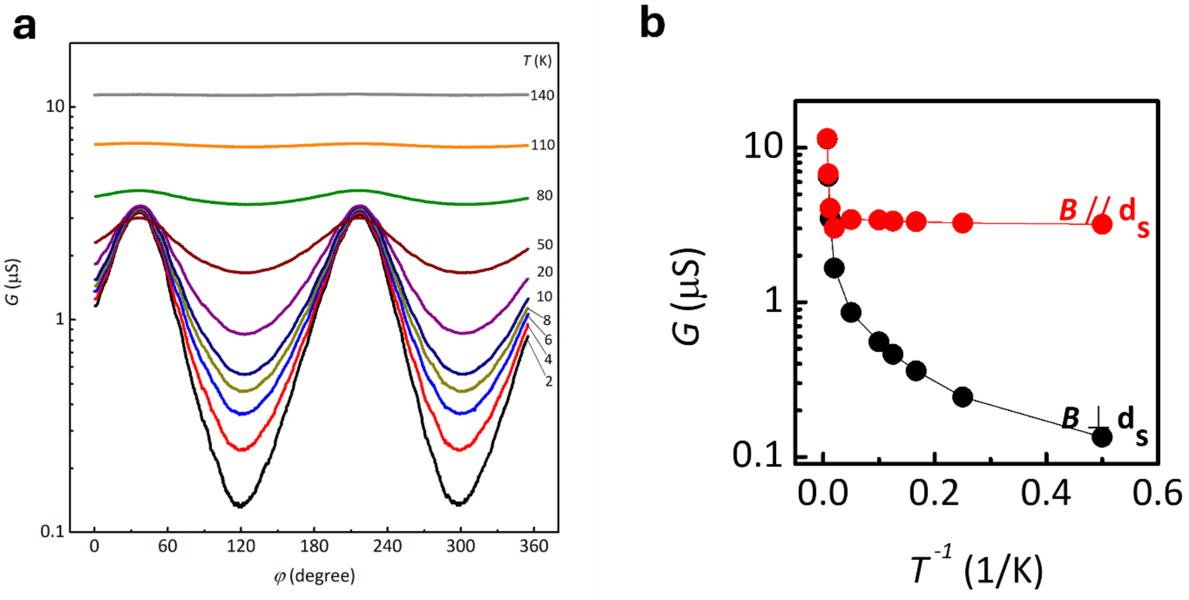

Figure 2.8. Temperature dependence of the angular anisotropy. **a**, Conductance plotted as a function of φ at fixed temperature. Below, ~100 K, our conductance becomes dominated by the edge. We observe no significant dependence on the location of the maxima and minima as a function of temperature. The maximum value plateaus below ~50 K, while the minimum value decreases monotonically with temperature. **b**, G plotted against T^{-1} for φ_{so} and $\varphi_{\mathrm{so}} + 90°$. Data taken with $B = 3$ T and $V_g = -2.7$ V on MW5.

Finally, we study the effect of the magnitude of the field on the angular anisotropy. In Figure 2.9a, we plot the conductance versus angle for field magnitudes ranging from 0 to 3 T. We then sweep the magnetic field between ±3 T aligned parallel to and perpendicular to $\boldsymbol{d}_{\mathrm{so}}$. We plot the conductance on a logarithmic scale in Figure 2.9b. The conductance drops roughly linearly with field magnitude on this scale parallel to $\boldsymbol{d}_{\mathrm{so}}$, and much more dramatically perpendicular to $\boldsymbol{d}_{\mathrm{so}}$.

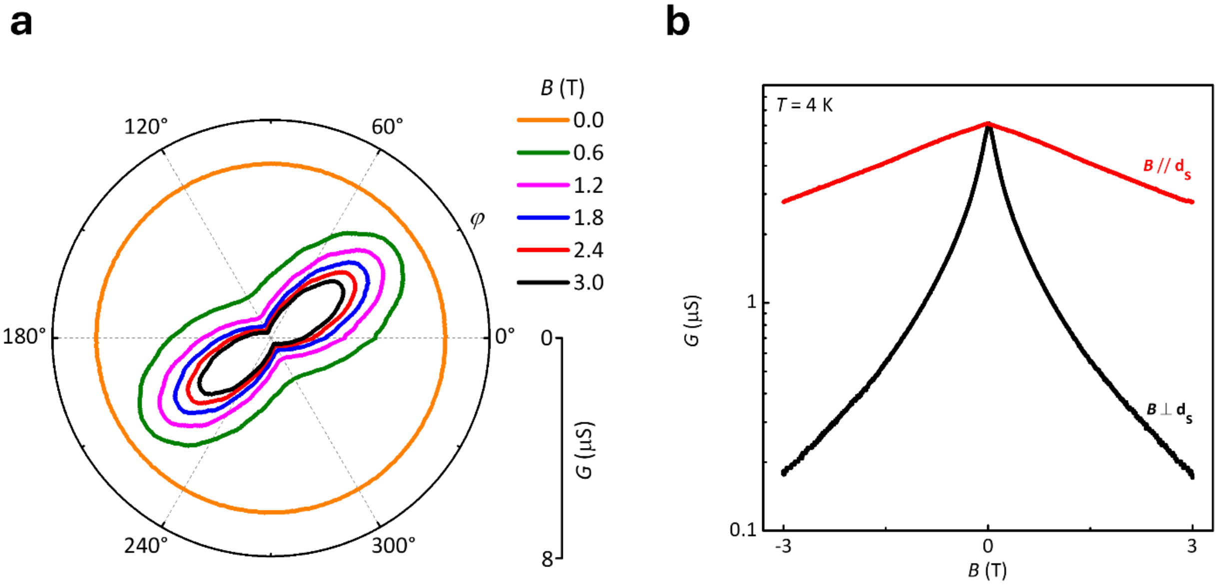

Figure 2.9. Angular anisotropy as a function of the field magnitude. **a**, Conductance plotted on a polar plot versus φ for fixed field magnitudes in the mirror plane. **b**, G plotted against B for situations with the field oriented parallel to $\boldsymbol{d}_{\mathrm{so}}$ and perpendicular to $\boldsymbol{d}_{\mathrm{so}}$, in red and black, respectively.

2.3 NONLINEAR MAGNETOTRANSPORT

Helical edge modes are also expected to exhibit a characteristic nonlinear magnetotransport effect [57–59]: In the Taylor expansion of the current-voltage relation, $I(V,\boldsymbol{B}) = G(\boldsymbol{B})V + \gamma(\boldsymbol{B})V^2 + \cdots$, the coefficient γ describes nonreciprocal conduction, allowed because the edge breaks inversion symmetry. Its $\boldsymbol{B}$-odd part, $\gamma_a(\boldsymbol{B}) = [\gamma(\boldsymbol{B}) - \gamma(-\boldsymbol{B})]/2$, is sensitive to the edge spin texture. Two main mechanisms contribute to $\gamma_a(\boldsymbol{B})$ at low temperature (see Section 2.4.1). In one, an exchange field proportional to the current-induced spin polarization (CISP) [60], which is along $\boldsymbol{d}_{\boldsymbol{so}}$, adds to the applied field to modify the conductance. In the other, nonlinear dispersion and broken inversion symmetry in the edge energy spectrum together lead to a lack of cancellation of quadratic-in-voltage currents carried by the two helical branches. For both mechanisms, $\gamma_a(\boldsymbol{B})$ should vanish under the same condition that the suppression of G is maximal.

Motivated by this prediction, we apply a large a.c. bias such that the $I - V$ traces become nonlinear. In Figure 2.10 we show $I - V$ traces over a range of +/- 30 mV in different magnetic fields. In red, there is a +0.3 T magnetic field applied, while in black, a -0.3 T magnetic field is applied. The top traces are taken when $\boldsymbol{B}$ is aligned parallel to the *z*-axis- an orientation where the field has a non-zero component along $\boldsymbol{d}_{so}$. The bottom trace is taken when $\boldsymbol{B}$ is aligned perpendicular to $\boldsymbol{d}_{so}$. We observe that when $\boldsymbol{B}$ has a component parallel to $\boldsymbol{d}_{so}$ the current has a component even in V that changes sign when $\boldsymbol{B}$ is reversed, i.e. it has a symmetry of V^2B. When the field is aligned perpendicular to $\boldsymbol{d}_{so}$ this even component of the current is vanishingly small.

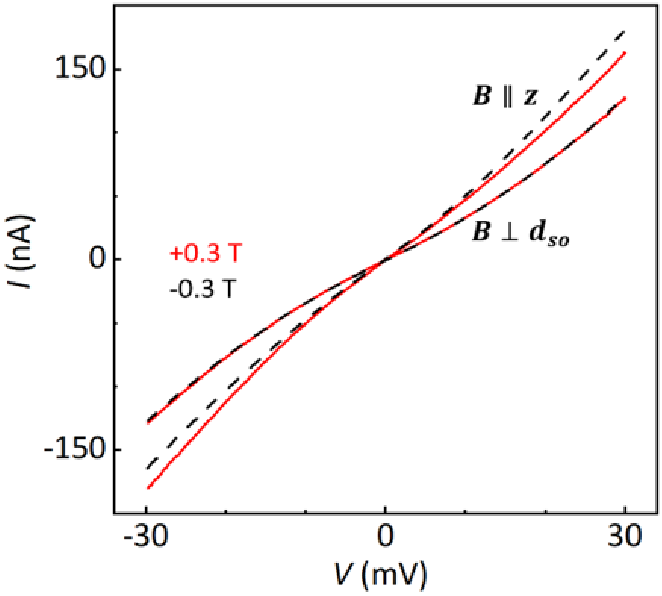

Figure 2.10. I-V measurements on device MW5. Red and black traces correspond to positive and negative field, respectively. We observe that the current has a component even in V and odd in $\boldsymbol{B}$, such that is has a symmetry of V^2B when the field is not perpendicular to $\boldsymbol{d}_{so}$. Measurements were taken at 5.5 K and at V_g = -2.7 V.

We then choose a bias voltage with amplitude $V_f = 15$ mV at a frequency of 101 Hz and measure the first-harmonic and second-harmonic responses (G and γ, respectively) separately, where $G = I_f/V_f$ and $\gamma = I_{2f}/2V_f^2$. In Figure 2.11 we plot G and γ as a function of out-of-plane magnetic field. Data is shown for contact pairs 1-2 in b and 3-4 in c. We observe this characteristic heartbeat shape in the second harmonic response, with it sharply changing sign with changing sign of the magnetic field. We note that this behavior does not depend on the orientation of the current path.

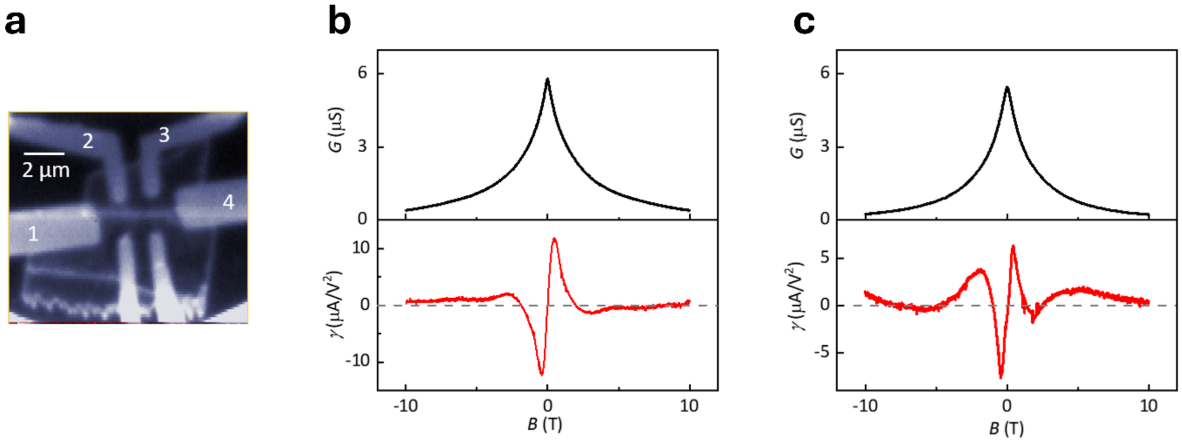

Figure 2.11. First- and second-harmonic response as a function of magnetic field. **a**, MIM image of device MW7. **b**-**c**, measurements of G and γ as a function of magnetic field. In **b**, the bias voltage is applied between contacts 1 and 2. In **c**, the voltage is applied between 3 and 4. We observe the same heartbeat pattern in the second harmonic response independent of the edge configuration. T = 4 K and $V_g = 0$ V.

Following this, we measure G and γ at various orientations of magnetic field. We set angle δ and sweep α with a fixed 0.3 T field magnitude, where δ is the angle in the x-y plane measured from the x-axis, and α is the angle measured down from the z-axis. We show the results of this measurement in Figure 2.12, plotting G in black and γ in red. We observe that for every measured value of δ, γ passes through zero at the angle in which G is minimized.

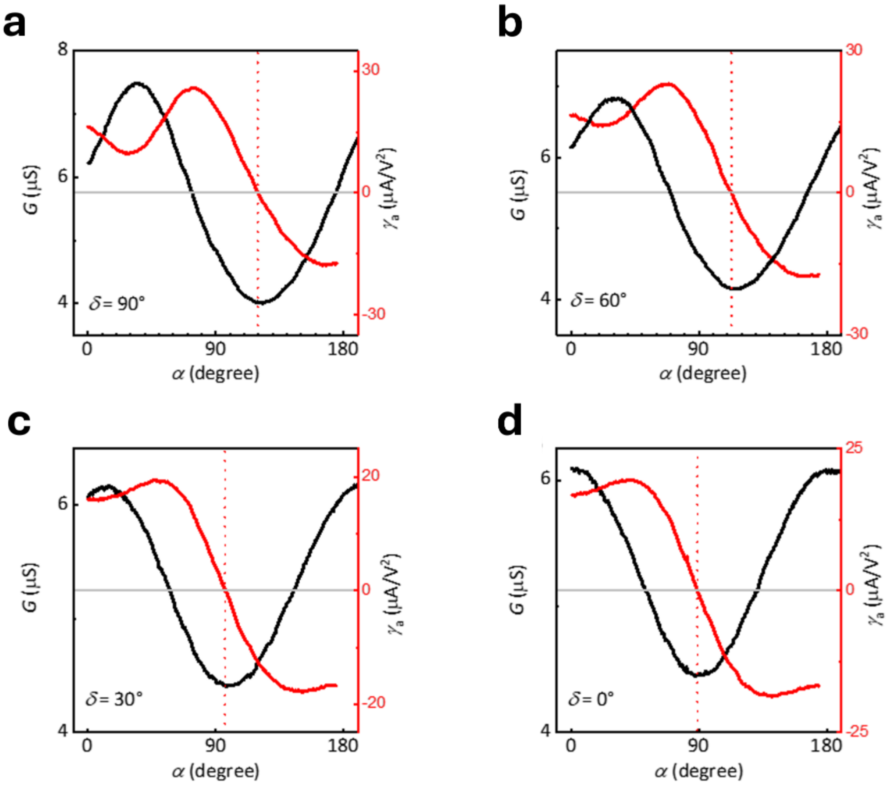

Figure 2.12. Nonlinear measurements for different magnetic field orientations. **a**-**d**, First-harmonic response (G, black) and second-harmonic response (γ, red) vs. α for B = 0.3 T at δ=90°, 60°, 30°, and 0°, respectively. The dashed lines show the angle at which $\gamma_\alpha = 0$.

2.4 THEORY OF EDGE RESISTIVITY

While it is still not known exactly which mechanisms dominate the resistivity and magnetoresistance of helical quantum wires (see Refs [61–65] and references therein), it is clear that the existence of a specific orientation in which $\boldsymbol{B}$ has minimal effect implies that the spins at the Fermi level E_F are aligned in this direction. Moreover, the constancy of $\boldsymbol{d}_{so}$ has a natural interpretation based on the symmetry properties of 1L WTe$_2$. The low-energy physics of bulk monolayer WTe$_2$ is captured by an effective $\boldsymbol{k} \cdot \boldsymbol{p}$ model constructed around the Γ-point in the Brillouin zone. The minimal model contains four bands, built from two orbitals (the bottom of the conduction band and the top of the valence band at Γ) and two spin states. Each orbital must have definite symmetry (even or odd) with respect $\mathcal{P}$, M_x, and C_{2x}. One group of first-principles studies [32,66–69] assumed that the two orbitals have opposite P and the same M_x symmetry (implying opposite symmetry under C_{2x}). In this case, the matrix elements of the $\boldsymbol{k} \cdot \boldsymbol{p}$ Hamiltonian that connect these basis states must be even under M_x and time-reversal $\mathcal{T}$, and odd under $\mathcal{P}$ (and C_{2x}) transformations. The leading-order allowed SOC terms then have the form $H_{SOC}^{\mathrm{I}} = \tau_x(v_x p_y \sigma_x + v_y p_x \sigma_y + v_z p_x \sigma_z)$, where the Pauli matrices τ_i (σ_i) act in the orbital (spin) space, and coefficients v_i have dimensions of velocity. SOC of this form projected into edge modes will produce an edge- and momentum-dependent spin axis that is not in the *y*-*z* mirror plane. This is not consistent with our findings.

Another group of first-principles studies [70–73] assumed instead that the orbitals have the same $\mathcal{P}$ but opposite M_x (and C_{2x}) symmetry. In this case the matrix elements connecting them must be even under $\mathcal{T}$ and $\mathcal{P}$, and odd under M_x (and C_{2x}). The leading-order SOC terms then have the form

$$H_{SOC}^{\mathrm{II}} = \tau_y(\lambda_y \sigma_y + \lambda_z \sigma_z) \equiv \tau_y \boldsymbol{D} \cdot \boldsymbol{\sigma} \,,$$

where coefficients λ_y and λ_z have dimensions of energy and $\boldsymbol{D} \equiv (0, \lambda_y, \lambda_z)$ can be thought of as a vector in the *y*-*z* plane making an angle of $\varphi_D = \tan^{-1} |\lambda_y/\lambda_z|$ with the *z*-axis. The bulk bands near Γ then consist of pairs related by the time reversal, whose spin expectation values are either along or opposite to $\boldsymbol{D}$ after tracing out the orbital components. Edge states near E_F will carry this same spin polarization as long as the coupling to bands far from E_F can be ignored. The presence of confining electric fields at the edge does not change this conclusion: even though they can modify the edge dispersion, their contribution to the spin-orbit coupling is small compared with that of the electric fields in the atomic orbitals that govern the bulk SOC. This is consistent with our findings if we identify $\boldsymbol{D}$ with $\boldsymbol{d}_{so}$, and hence φ_D with $\varphi_{so} = 40 \pm 2°$. Strictly speaking, the maximum conductance is expected when the direction of $\overleftrightarrow{g}\boldsymbol{B}$, not $\boldsymbol{B}$, coincides with the spin polarization direction. For a generic edge, the g-tensor $\overleftrightarrow{g}$ is not constrained by any symmetry and furthermore can depend on details of the edge. This can explain why the angular separation of the minima and maxima in G is not exactly 90°, but ranges down to 83° (in Figure 2.8a it is 85°.) However, the lack of variation of $\boldsymbol{d}_{so}$ implies either that $\overleftrightarrow{g}$ is nearly isotropic or, at least, that $\boldsymbol{d}_{so}$ remains close to a principal axis of $\overleftrightarrow{g}$ irrespective of the edge structure.

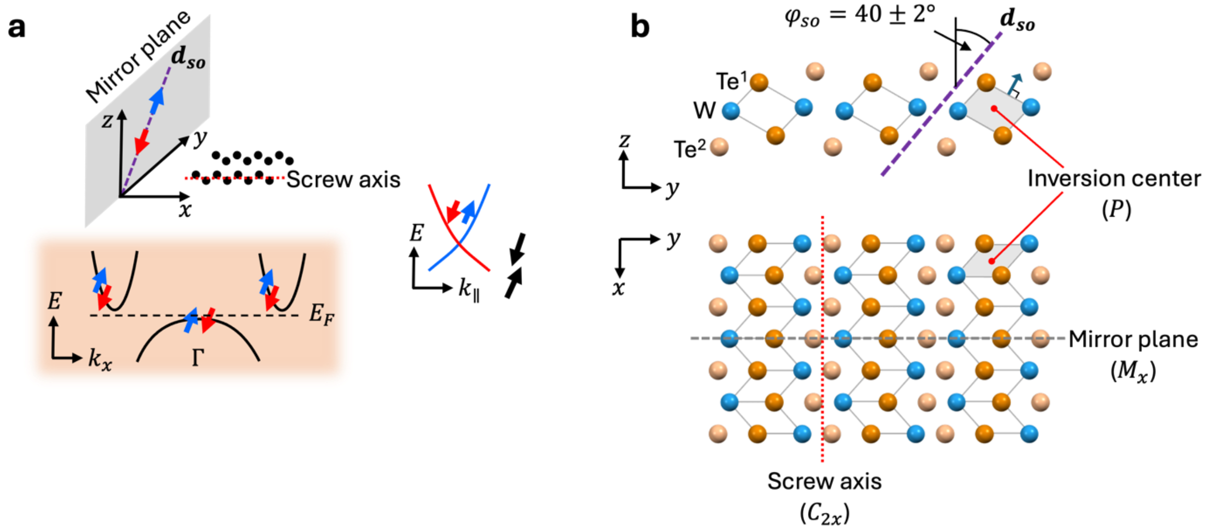

Figure 2.13. The spin axis of monolayer WTe$_2$. (a) Cartoon illustrating our key findings: the edge modes on monolayer WTe$_2$ are spin polarized along an axis $\boldsymbol{d}_{so}$ that is independent of edge orientation and shared with the bulk conduction and valence band edges, sketched here schematically near Γ. (b) Side and top views of the 1T′ monolayer structure indicating the three spatial symmetries (P, M_x and C_{2x}), and showing the direction of $\boldsymbol{d}_{so}$, which is in the y-z mirror plane making angle $\varphi_{so} = 40 \pm 2°$ with the z-axis. Tungsten atoms are shown blue, and the two inequivalent tellurium atoms, Te^1 and Te^2, are different shades of orange. The screw axis (red dotted line) is along the center of a zigzag tungsten chain.

The form of H_{SOC}^{II} can also be derived in a microscopic 8-band tight-binding model [70,73], in which it corresponds to the strongest spin-flip hopping process in the y direction along the Te^1-

W bonds (drawn as lines in Figure 2.13b). It is not possible to calculate $\boldsymbol{D}$ accurately since the parameters in the models are not known well enough. Nevertheless, it is worth noting that the two interfering hopping paths that involve intermediate Te sites on the adjacent Te^1-W bonds give the standard Haldane-Kane-Mele [23,74] contribution to $\boldsymbol{D}$. This turns out to be perpendicular to the Te^1-W bond, in the mirror plane at 29° from the z-axis (indicated with a blue arrow in Figure 2.13b), which is not too different from the measured value of φ_{so}. Near the bulk band edges, which occur at finite values of p_x, and zero p_y, the two types of the spin-orbit coupling described above are similar to each other, and lead to a quantum spin Hall state with a canted spin quantization axis. The properties of this state are described in Ref. [69].

Further theoretical work toward understanding the magnetoresistance of WTe_2 was done, led by our collaborators in Chen, Y,; Zhao, W.; **Runburg, E.**, *et al.* Magnetotransport on quantum spin Hall edge coupled to bulk midgap states. *Phys. Rev. B.* **8**, 085436 (2023) [52]. The central question of this work surrounds the magnitude of the effect of the magnetic field at small field values. Here, we argue that a small Zeeman field can have a large effect on the conductance of the edge state if it can cause long-lasting spin procession. The mechanism of conductance suppression is through edge electrons hybridizing with bulk mid-gap states due to impurities, such as Te-vacancies. The magnetic field will then cause large precession angles, creating significant backscattering, and strongly suppressing conductance.

In this work, it is argued that the magnetoconductance should follow one of two functional forms: so-called “coherent transport”, where the impurities are dilute and thus act independently on the edge electrons, and “incoherent transport,” where there is inelastic relaxation on the edge. The edge conduction in the coherent regime, for small fields, is calculated to follow this expression:

$$\frac{G(B)}{G(0)} \approx \exp\left[-\frac{L_x}{\ell}\frac{|B|}{B_0}(1-|\cos\theta|)\right],$$

where the overall factor of $(L_x/\ell)(B/B_0)$ is the number of midgap states located on an edge multiplied by an energy factor near the Fermi level. Meanwhile, edge conduction in the incoherent regime is expected to follow:

$$\mathrm{G}(B) \approx \frac{1}{G^{-1}(0) + \frac{h}{e^2}\frac{L_x}{\ell}\frac{|B|}{B_0}\sin^2\theta}.$$

In the small-field limit, both cases predict a linear rise in resistance with magnetic field, with a form of

$$R(B,\theta) = R(0,\theta)[1+\beta_1(\theta)|B|]$$

where $\beta_1(\theta)$ is given by:

$$\beta_1^{coh} \propto (1+|\cos(\theta-\theta_0)|),$$

$$\beta_1^{incoh} \propto \sin^2(\theta-\theta_0).$$

Given these predictions, we fit our low-field angular dependence measurements to these functional forms. We find that fitting to a form of

$$\beta_1(\theta) = c_0 + c_1\sin^2(\theta-\theta_0)$$

with $c_0 = 0.1\,T^{-1}$, $c_1 = 3.2\,T^{-1}$, $\theta_0 = 33.7°$ fits our experimental results very well, as seen below in Figure 2.14.

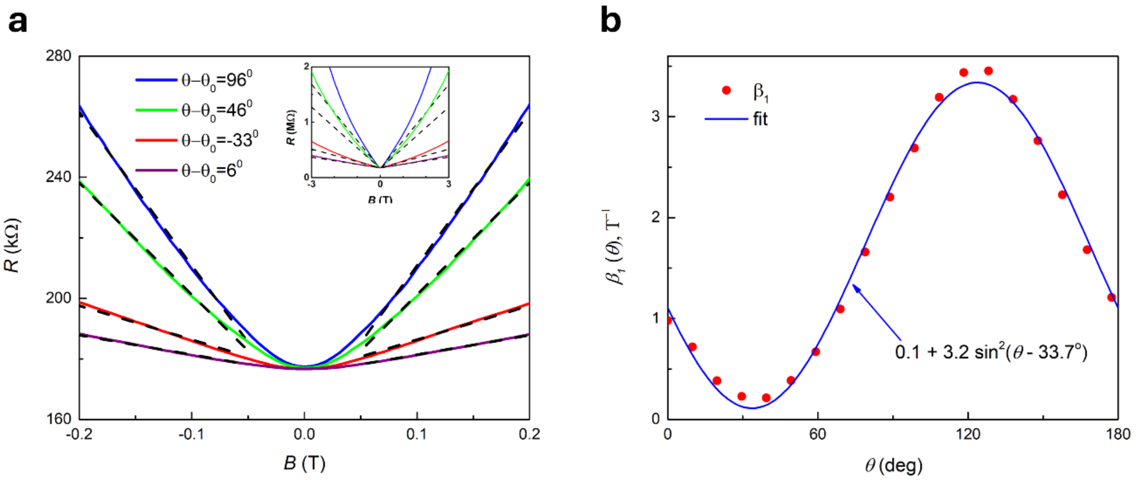

Figure 2.14. Fitting of the low-field angular magnetoresistance to the functional form described by incoherent transport. **a**, Low field data (colorized) with linear fits of R(B) from 0.05 T to 0.2 T taken for each dataset and overlaid. Inset shows the deviation from this small-field behavior at larger field magnitudes. **b**, Extracted slopes from the angular data (as shown in **a**) plotted against a fit to the angular form of β_1.

2.4.1 *Theory of the nonreciprocal response*

There is a peculiar nonlinear magneto-transport response in monolayer WTe$_2$, which is characterized by a contribution to the current that is odd in magnetic field $\boldsymbol{B}$ and even in the applied voltage V. In the Taylor expansion of the $I-V$ characteristic at small voltages, $I(V,\boldsymbol{B}) = G(\boldsymbol{B})V + \gamma(\boldsymbol{B})V^2 + \cdots$, this effect is present when $\gamma(\boldsymbol{B}) = -\gamma(-\boldsymbol{B}) \neq 0$. The origin of this effect can be traced to the Hamiltonian of the helical edge electrons in the presence of a magnetic field. The single-particle disorder-free edge Hamiltonian reads

$$H_{edge} = \epsilon_s(p) + \epsilon_a(p)\boldsymbol{d_{so}} \cdot \boldsymbol{\sigma} + \frac{1}{2} g\mu_B \boldsymbol{B} \cdot \boldsymbol{\sigma} \tag{1}$$

where p is the momentum along the edge, $\epsilon_{s,a}(p) = \pm\epsilon_{s,a}(-p)$, μ_B is the Bohr magneton, and g is the g-factor of the edge electrons. For the time being, we disregard its anisotropy for simplicity.

The g-tensor will be discussed in a bit more detail below, when we talk about the current-induced polarization on the edge. If we denote the component of $\boldsymbol{B}$ in the direction of $\boldsymbol{d_{so}}$ by $B_{\parallel}$, and the one perpendicular to $\boldsymbol{d_{so}}$ by $\boldsymbol{B}_{\perp}$, then the edge spectrum is given by

$$E_{\pm}(p) = \epsilon_s(p) \pm \sqrt{\left(\epsilon_a(p) + \frac{1}{2} g\mu_B B_{\parallel}\right)^2 + \left(\frac{1}{2} g\mu_B B_{\perp}\right)^2} \tag{2}$$

where " $\pm$ " pertain to the edge conduction and valence bands.

The sought-for nonlinear response arises from two features of H_{edge}. First, it is apparent that $B_{\parallel} \neq 0$ breaks the "inversion symmetry" in the edge spectrum, $E_{\pm}(p) \neq E_{\pm}(-p)$. It is known that such a property in general leads to a current response quadratic in the applied electric field [75], and hence to a nonzero $\gamma(\boldsymbol{B})$. For a helical edge, this response vanishes for a purely linear spectrum $\epsilon_a(p)$; therefore it is sensitive to the band curvature. In general, it is hard to microscopically evaluate the value of $\gamma(\boldsymbol{B})$ that stems from the lack of inversion in the edge spectrum without a reliable model of linear magneto-transport. We will not pursue mechanisms related to the spectrum asymmetry further, other than to point out that the contribution of such mechanisms to the nonlinear magneto-transport vanishes when $B_{\parallel} = 0$, i.e., $\boldsymbol{B} \perp \boldsymbol{d}_{so}$, which is consistent with our experimental findings. Instead, we will show below that a semi-phenomenological model based on the current-induced spin polarization provides an adequate understanding of the measured nonlinear signal with minimal tuning of parameters.

The second feature of H_{edge} relevant for the nonlinear transport is the edge spin-momentum locking due to a strong spin-orbit coupling and the lack of spatial inversion symmetry on the edge. Under such circumstances, there exists current-induced spin polarization (CISP) of the itinerant carriers. For H_{edge}, the spin polarization, $\boldsymbol{s}$, is directed along $\boldsymbol{d}_{so}$. We define it as the difference between the local densities of electrons with spins along or opposite to $\boldsymbol{d}_{so}$ thus: $\boldsymbol{s} =$

$\frac{1}{ev_{edge}}I\boldsymbol{d}_{so}$ (taking $\boldsymbol{d}_{so}$ to be a unit vector). Here e is the electron's charge, and v_{edge} is a coefficient with the dimensions of speed. For a clean non-interacting edge, v_{edge} can be extracted from H_{edge}, but in general should be kept as a phenomenological parameter. In the presence of electron-electron interaction, finite spin polarization leads to a self-energy that modifies H_{edge}. In the mean-field approximation, and for an $SU(2)$ invariant point-like interaction, the current-induced correction to H_{edge} has the form of an effective Zeeman coupling, and reads [60]

$$\delta H_Z = \frac{1}{2} g_{\parallel}\mu_B \beta I \boldsymbol{d}_{so} \cdot \boldsymbol{\sigma} \tag{3}$$

In δH_Z, we introduced $g_{\parallel}$, the effective g-factor in the direction of $\boldsymbol{d}_{so}$, which defines the Zeeman field for the actual externally applied B field, and a phenomenological coefficient β that defines the current-induced effective magnetic field felt by the edge electrons, $\boldsymbol{B}_{ex} = \beta I \boldsymbol{d}_{so}$. The coefficient β is related to the electron-electron interaction strength and is discussed below.

At this point we can discuss the influence of the CISP on the transport properties of the edge electrons. In what follows, we assume that one of the principal axes of the effective g-tensor of the edge electrons is directed along $\boldsymbol{d}_{so}$. This need not be the case in general, even if the bulk band structure consists of bands fully polarized along and opposite to $\boldsymbol{d}_{so}$, because of the orbital effects associated with the nontrivial geometry of such bands [76]. However, the fact that the directions of the $\boldsymbol{B}$ field that correspond to the minimum and maximum magneto-conductance on the edge are at almost 90° to each other suggests that such orbital effects are weak, and $\boldsymbol{d}_{so}$ is indeed a principal axis of the g-tensor. This is consistent with strong confinement of the edge states in WTe_2 [15,39,50]. It then follows that the total Zeeman field felt by the edge electrons corresponds to a certain total magnetic field, which is a simple vector sum of the external field, $\boldsymbol{B}$, and the current-induced effective field, $\boldsymbol{B}_{ex}$. Consequently, the current flow on the edge is described by the following (self-consistent, in principle) equation: $I(t) = G(\boldsymbol{B} + \beta I(t)\boldsymbol{d}_{so})V(t)$, where $G(\boldsymbol{B} + \beta I\boldsymbol{d}_{so})$ is the linear conductance evaluated at the total magnetic field. Under the experimental conditions, the nonlinear current was small compared with the linear one, hence we can assume that the CISP is determined only by the linear-response current. Further, assuming sinusoidal variation of the voltage with time, expanding to linear order in β, and switching to polar coordinates in the *y-z* mirror plane, we can obtain a relation between the amplitudes of the first- and second-harmonic signals and hence the coefficient $\gamma(\boldsymbol{B})$ in the Taylor expansion of the current as a function of the applied voltage:

$$\gamma(\boldsymbol{B}) = \beta G(\boldsymbol{B})\left(\frac{\partial G}{\partial B}\cos(\varphi - \varphi_{so}) - \frac{1}{B}\frac{\partial G}{\partial \varphi}\sin(\varphi - \varphi_{so})\right) \tag{4}$$

This expression for $\gamma(\boldsymbol{B})$ vanishes for $\boldsymbol{B} \perp \boldsymbol{d_{so}}$, when $\varphi = \varphi_{so} \pm \pi/2$, and $\frac{\partial G}{\partial \varphi} = 0$, since the linear conductance is minimal when $\boldsymbol{B} \perp \boldsymbol{d_{so}}$ at given B. Again, this property is observed in the experiment.

We show that the CISP mechanism explains qualitative features of the angular dependence of I_{2f} (at not too small magnetic fields) in Figure 2.15. This fact allows us to estimate the strength of the electron-electron interaction for edge electrons. Assuming long-range Coulomb repulsion, we note that the effective one-dimensional interaction has weak logarithmic dependence on the momentum transfer, $V_{1\mathrm{D}}(q) \approx \frac{e^2}{4\pi\epsilon_0\epsilon} \ln\left(\frac{1}{q^2a^2}\right)$, where a is a cut-off length scale of the order of the confinement length of the edge states, and $\epsilon \approx 4$ is the dielectric constant of the hBN surrounding the WTe$_2$. In real space, one can treat such an interaction as an approximately local one with strength $V = V_{1\mathrm{D}}\left(q \sim \frac{1}{d}\right)$, where $d \sim 25\,\mathrm{nm}$ is the distance to the metallic gate. These considerations lead us to estimate $\beta \sim \frac{e}{2\pi\epsilon_0\epsilon\, g\mu_B v_e} \ln\left(\frac{d}{a}\right)$, where g and v_e are the typical values for the g-factor and edge speed, at the Fermi wave vector for the edge electrons. For the typical values of $g \sim 5$, $v_F \sim 5 \cdot 10^5$ m/s, and $d/a \sim 5$, we obtain $\beta \sim 0.05\ \mathrm{T/nA}$. This figure is about an order of magnitude larger than the one needed to fit the data (see Fig. S12). It probably shows that the Coulomb interaction is screened more substantially than implied by the above estimate. Given that the parameters that enter into the estimate for β are not well known, one can turn it around to get an estimate for the dimensionless interaction strength on the edge, $V/v_e = \frac{e^2}{2\pi\epsilon_0\epsilon\,\hbar v_e}\ln\left(\frac{d}{a}\right)$ from the measured values of $\beta \sim 3 \cdot 10^{-3}\ \mathrm{T/nA}$: $V/v_e \sim eg\beta\mu_B/\hbar \sim 0.1$. That is, the edge is not strongly interacting.

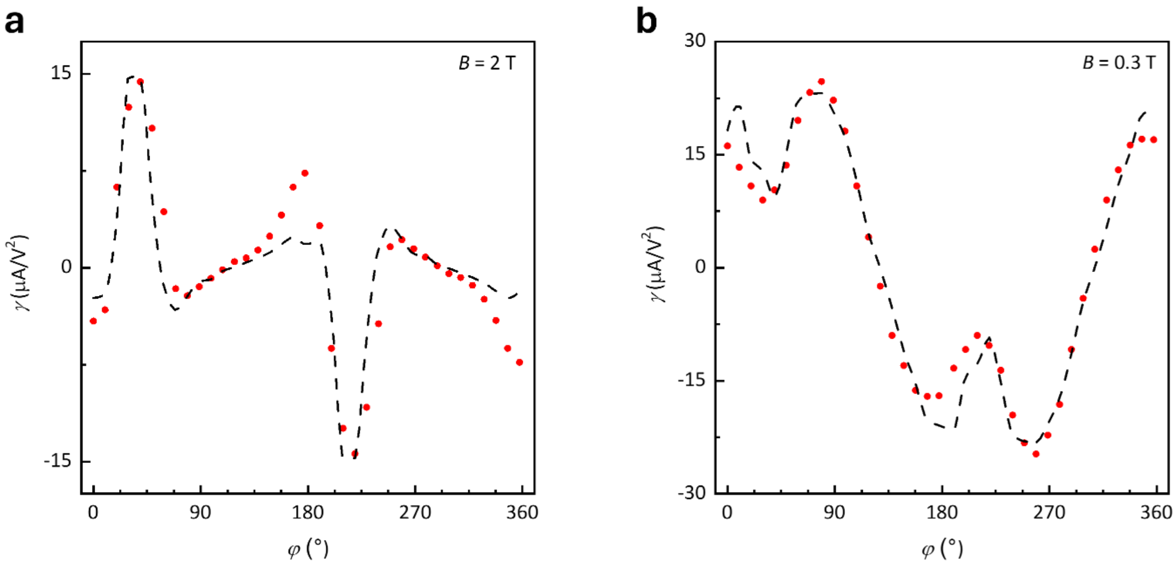

Figure 2.15. Fitting γ describing the CISP contribution to the nonlinear conductance against angle, compared to the experimental values. **a**, $B = 2$ T, using $\beta = 3.5 \times 10^{-3}$ T/nA in the fit for γ. **b**, using $\beta = 1.0 \times 10^{-3}$ T/nA in the fit for γ.

In order to better capture the low-field behavior of γ, further theoretical study was done with our collaborators in Chen, Y.; Quaresima, G.; Zhao, W.; **Runburg, E.**, *et al.* Magnetochiral anisotropy on a quantum spin Hall edge, (in preparation) [53]. Extending work from the previous section, we consider the effect of the edge electrons coupling to a midgap state on the nonlinear conductance- specifically on impact on γ_a, the even-in-V, odd-in-B component of the nonlinear conductance.

I will leave the specifics of the argument to the paper; the main result is a calculation of the functional form of γ_a to be:

$$\gamma_a(B,\theta) = \tilde{\gamma}(\sin^2(\theta-\theta_0)+\delta)\cos(\theta-\theta_0)\frac{B^3}{B^2+B_\Gamma^2},$$

where $\tilde{\gamma}$ is a constant proportional to the length of the channel, θ_0 is the direction of the spin axis with respect to the normal of the plane, δ is a parameter to account for the possibility of fluctuations of the local spin polarization axis due to midgap coupling, and B_Γ is a magnetic field scale corresponding to the midgap level width that affects the rounding of the conductance at small B. Given this result, we fit our data over a wide range of B and θ to this form to obtain the parameters $\tilde{\gamma}$, θ_0, δ, and B_Γ. The best fit to the experimental values are $\tilde{\gamma} \approx 2.1 \times 10^{-4}\ \mathrm{AV^{-2}T^{-1}}, \delta \approx 0.14, B_\Gamma \approx 0.1\ \mathrm{T}$, and $\theta_0 = 34.6°$. We plot the result of this fit in Figure 2.16 and find good agreement between the experimental results and the theoretical model.

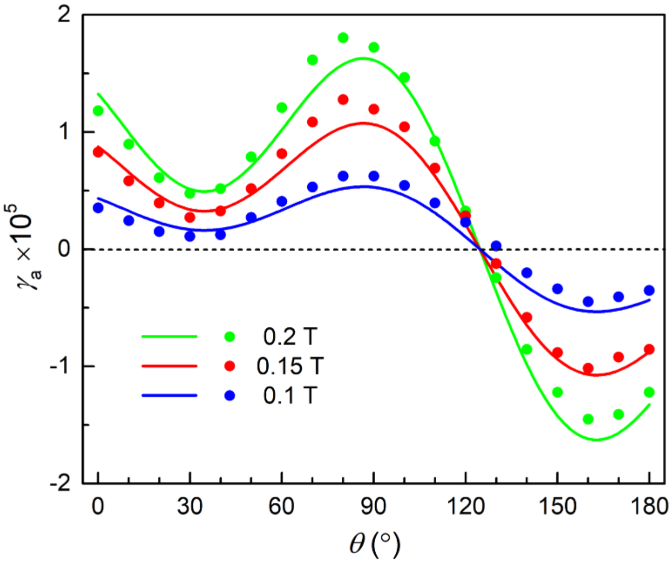

Figure 2.16. Fits of the functional form of $\gamma_a(B, \theta)$ (solid line) versus experimental data (dots) for different magnitudes of field.

2.5 MAGNETORESISTANCE OF BILAYER WTE$_2$

In order to confirm that this behavior is related specifically to the quantum spin Hall state of monolayer WTe$_2$, we perform the same magnetic anisotropy measurements on bilayer WTe$_2$, device BW7. Bilayer WTe$_2$ is topologically trivial and lacks protected edge states. In Figure 2.17, we show the results of these measurements. The magnetoconductance shows a peak when the magnetic field is rotated at either $\theta' = 90°$ or $\theta' = 0°$ depending on the gate voltage. Additionally, we see that there is no nonreciprocal conductance, as the $I - V$ traces at opposite signs of magnetic field lay directly on top of one another.

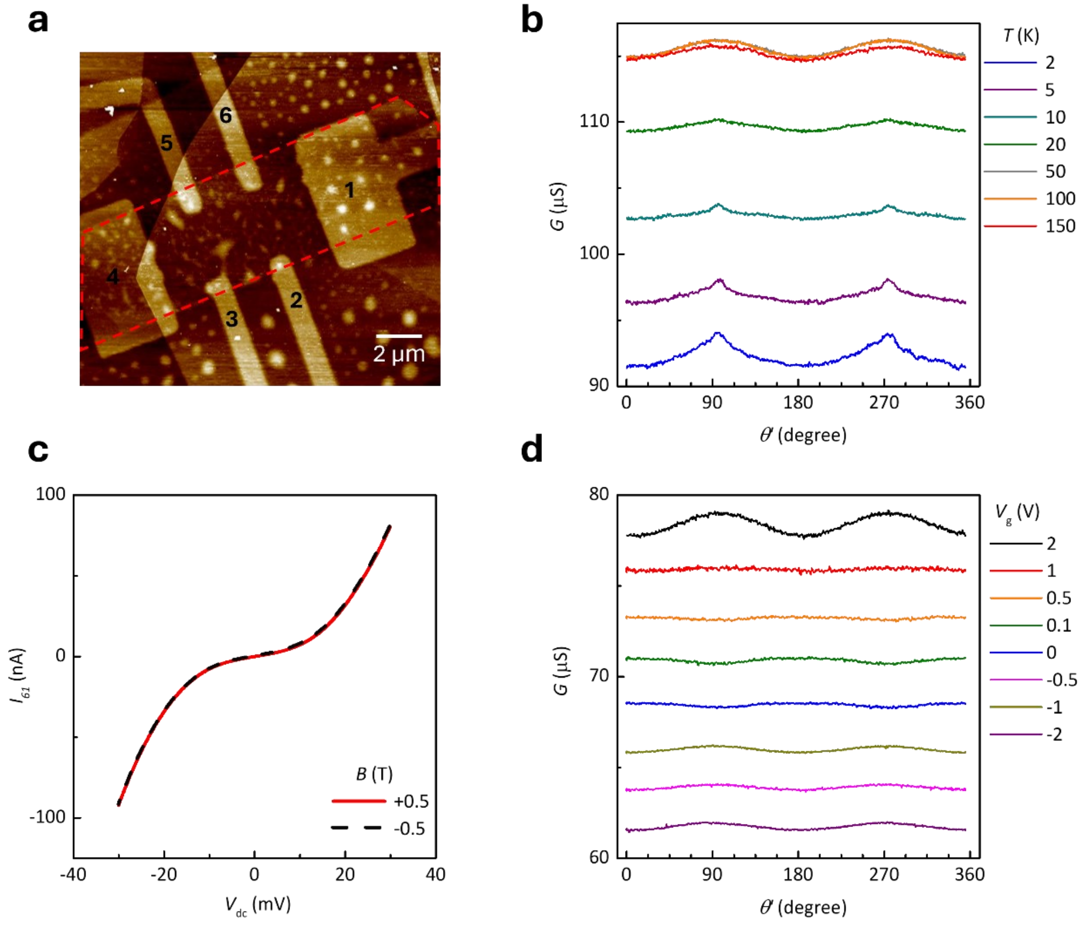

Figure 2.17. Angular anisotropy of bilayer WTe_2 device BW7. **a**, AFM image of the device. WTe_2 flake outlined in red. Contacts labelled, 1 and 6 used for subsequent measurements. **b**, Temperature dependence of the angular anisotropy. Traces vertically offset for clarity. **c**, $I - V$ traces at ±0.5 T. Unlike the case of monolayer WTe_2, the traces lie directly on top of each other, showing no sign of nonreciprocal conductance. **d**, Gate dependence of the angular anisotropy. Traces offset for clarity.

2.6 CONCLUSION AND OUTLOOK

In this chapter, we demonstrated that the edge states of WTe_2 have a particular spin texture, confirming their helical nature and showing it hosts the quantum spin Hall insulating state. The anisotropy of the conductance in a magnetic field indicated a preferred direction for the edge state that minimizes backscattering. This direction shows minimal dependence on the orientation of the edge, gate voltage, temperature, and magnitude of the magnetic field. We also observe a nonreciprocal component of the conductance as a function of field that is unique to helical edge states. We performed a control experiment with bilayer WTe_2 that demonstrated this anisotropy of the magnetic response is unique to the edge states of the monolayer.

We also developed a theoretical model to understand this behavior. We identify the correct form of the spin-orbit coupling based on our results. Further work was done to understand the low-field linear conductance behavior by considering the interaction of the edges with a midgap defect state in the bulk. Moreover, theoretical explanations were developed to explain the nonreciprocal response of the edge. The current-induced spin polarization can adequately explain the high-field data, while a similar model of midgap defect states can explain the low-field behavior.

Chapter 3. Nonlinear Edge Conductance of Monolayer WTe_2

As described in Chapter 1, monolayer WTe_2 has an insulating regime as a function of electron density, where current can flow through the edge of the crystal, but not through the interior (bulk) region. When performing a two-terminal conductance measurement on adjacent pairs, this bulk insulating regime will appear upon cooling to ~100 K, and the insulating regime will grow upon further cooling. Within this bulk insulating regime, there will be a non-zero edge conductance measured. The value of the edge conductance is sensitive to the mesoscopic arrangement of the device, but as a function of electron doping, tends to fluctuate around one average value, that we will call the 'edge plateau'. From its appearance at 100 K, down to around 10 K, the conductance of the edge plateau shows little temperature dependence. However, upon cooling the device past ~10 K, the conductance level of the plateau will decrease, until there is no measurable linear response from the device. We would like to be able to study the edge states in WTe_2 at millikelvin temperatures, where thermal effects on the device should leave it most stable.

3.1 TEMPERATURE DEPENDENCE OF WTE_2 EDGES

In order to study the WTe_2 edges at the coldest temperatures, we fabricated a device, MW17, with adjacent Pt contacts along one straight WTe_2 edge, shown in Figure 3.1a-b. This device has two graphite gates, above and below, allowing for independent control of the electron density n_e and displacement field $\boldsymbol{D}$.

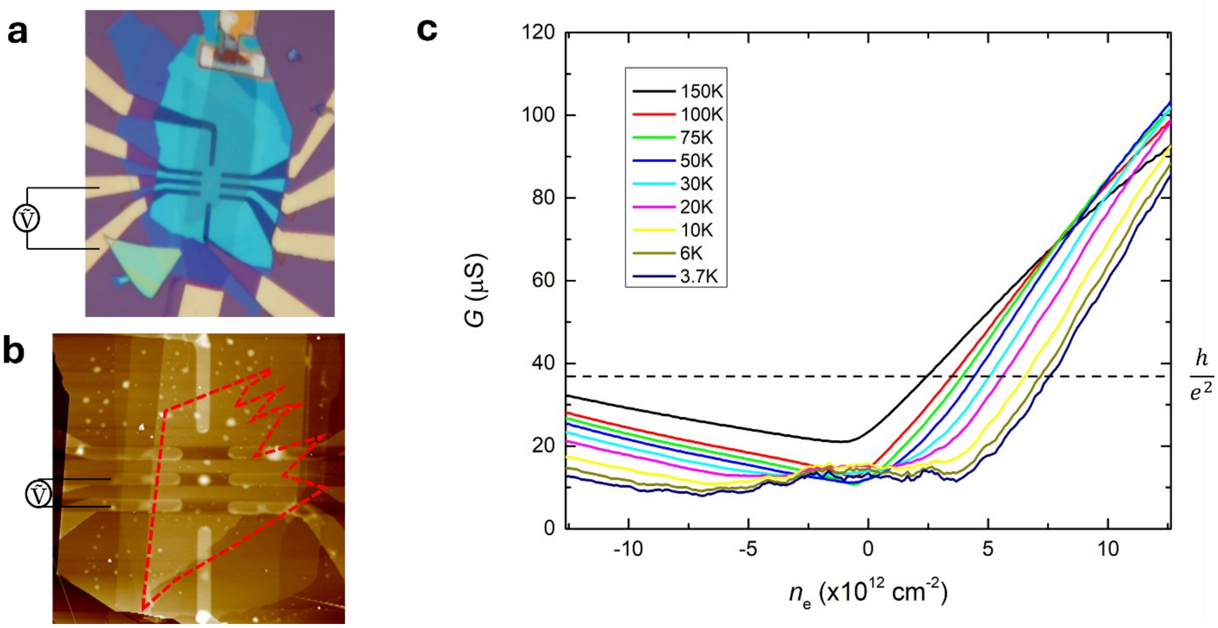

Figure 3.1. Device MW17. **a**, Optical image of the device. Contact pair used to make two-terminal measurements shown in schematic. **b**, AFM image of the device. Red dashed line is used to show the location of the monolayer WTe_2 flake. Again, contact pair is highlighted. Contact spacing is roughly ~1 μm. **c**, Two-terminal conductance of the device versus electron doping, at temperatures above 2 K. We observe an edge plateau appear for doping levels between -7 and $+5\times10^{12}$ cm^{-2}. The value of the conductance quantum is marked on the plot. Our edge plateau falls short of the quantized value, which is expected for an edge of this length.

The device is cooled, with sweeps of the electron density taken at fixed temperature while measuring the two-terminal conductance. This data is plotted in Figure 3.1c. We observe a conductance plateau forming at a level of ~12 μS down to our base temperature of 3.7 K. This value is less than the quantized value one would expect for helical edges, but the edge length between contacts of ~1 μm is much longer than the literature values reported for observing quantization in the edges [44].

Upon cooling the device to 1 K, we see a dramatic suppression of the edge conductance, dropping from a fairly stable value of 12 μS down to less than 4 μS. Figure 3.2 shows the linear conductance when both gates are swept, with the electron density plotted on the horizontal axis and the displacement field plotted along the vertical axis. In the top-left panel, at 1 K, we observe mesoscopic fluctuations of the conductance as the electron density is swept, with no dependence on the displacement field. The device is cooled further, in steps of 100 mK, down to 200 mK, where hardly any current can be measured in the linear response regime.

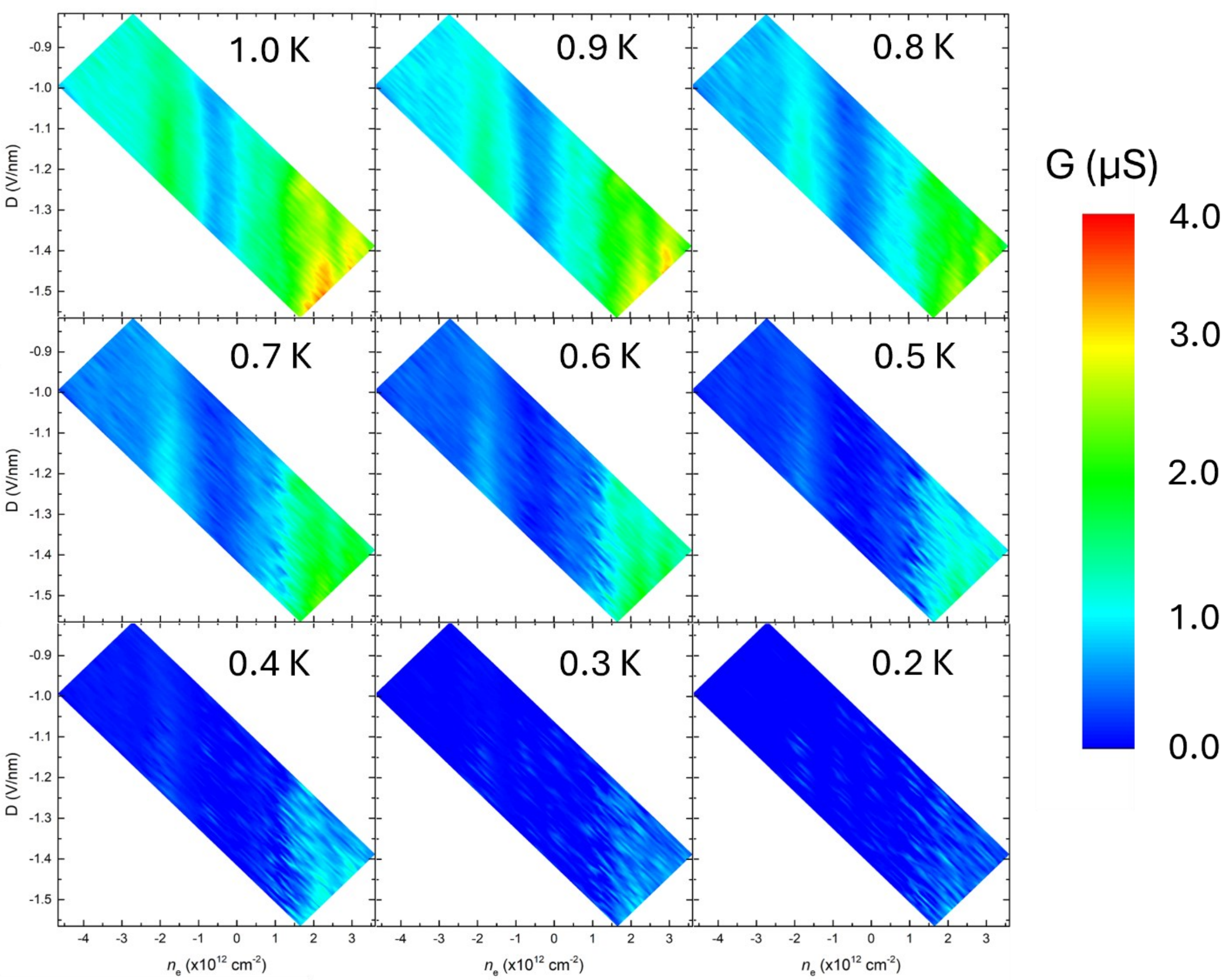

Figure 3.2. Edge conductance below 1 K. Conductance is measured in temperature steps of 100 mK, over a gate regime in n-D space where the bulk is insulating. The response is modulated only by the density, typical of a WTe_2 edge. By 0.2 K, only the faintest traces of edge conduction remain from the signal seen at 1 K.

In Figure 3.3 we show the conductance of the device as a function of both gates near the base temperature, at 100 mK. At this temperature, only the faintest traces of conduction in the insulating regime are visible. Additionally, we see observe a larger-than-usual gate voltage required to turn on the bulk conduction- around 1×10^{13} cm^{-2} equivalent density as calculated by the capacitance of each gate on the electron side, and at the highest hole densities of 2.2×10^{13} cm^{-2}, we do not measure any current. Furthermore, though we achieve the necessary density and temperature required to observe superconductivity in monolayer WTe_2, we see no sign of superconductivity.

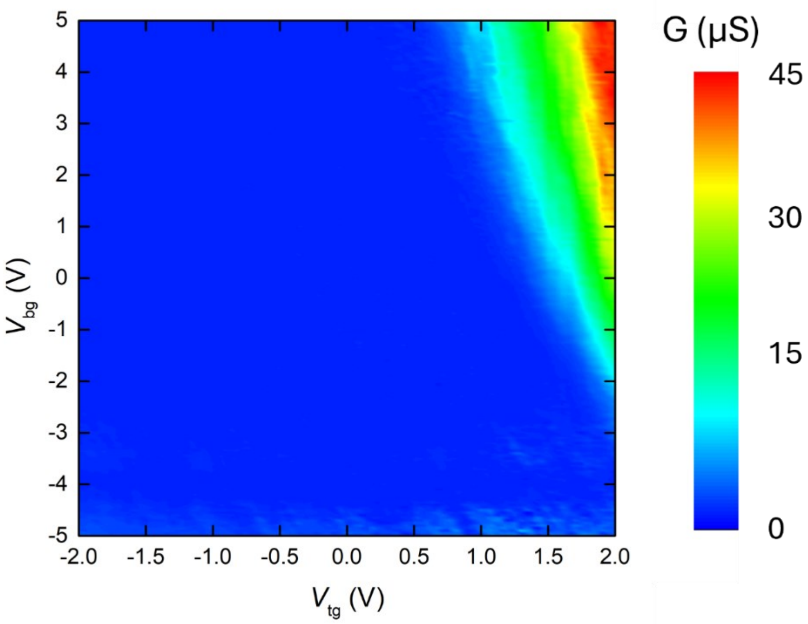

Figure 3.3. Gate-gate map at 100 mK. Conductance is measured as a function of the gate voltages. We observe *n*-type conduction at high positive gate voltages, but see no signs of *p*-type conduction, which we expect given the accessible electric fields the gates can apply.

Even at these temperatures and conditions, edges can still carry current, but not in linear response. By applying a large voltage bias to the contacts, a current can be driven through the device. The behavior of the system in this regime is less theoretically understood and bounded.

3.2 NONLINEAR TRANSPORT CHARACTERISTICS

To study the nonlinear response of the edge, we measure the differential resistance of the device as a function of applied d.c. bias. We sweep a d.c. bias from -1.5 mV to +1.5 mV, while simultaneously applying a small a.c. bias of 10 μV and measuring the a.c. current. The a.c. bias functions to slightly modulate the bias at each d.c. step, allowing for an approximation of the derivative of the current with bias at each step.

3.2.1 *Gate voltage dependence*

First, we sweep the bias at fixed gate voltages. We choose an area of positive top gate voltage and negative bottom gate voltage. In this region, we see some residual edge conduction. Furthermore, the WTe_2 laying on top of the contacts should be screened from the bottom gate by the Pt electrode, thus only responding to the top gate. The idea is that the positive top gate will dope the WTe_2 on the contacts into a slightly conducting regime, resulting in lower contact resistance to our device.

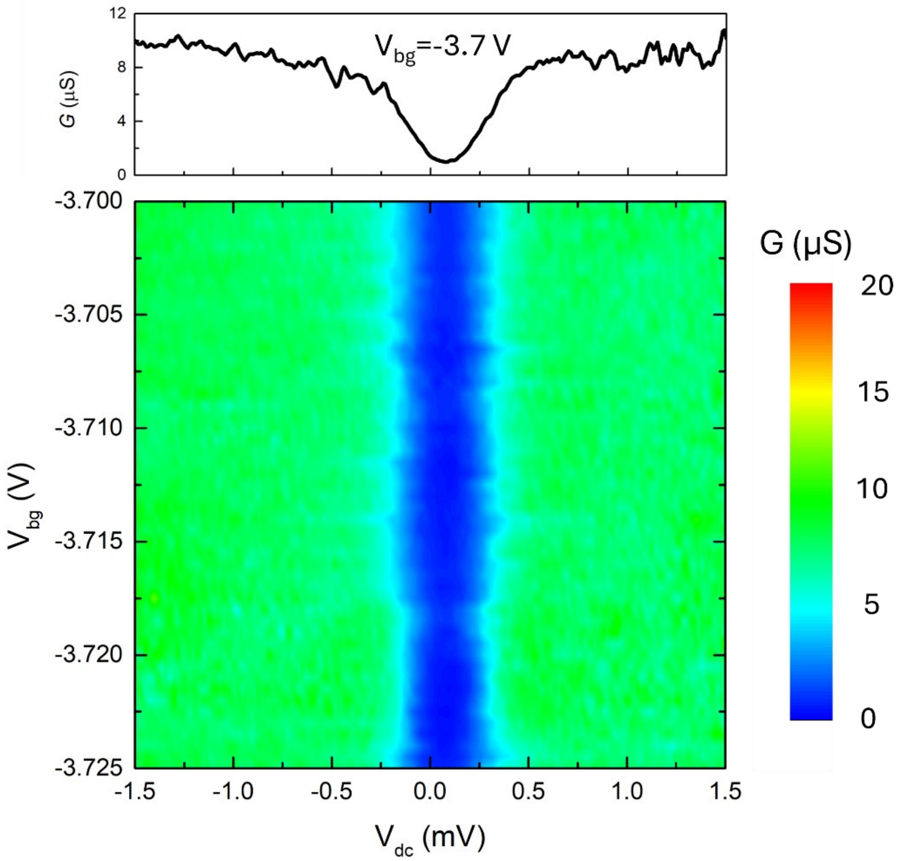

Figure 3.4. Nonlinear conduction at 100 mK. The d.c. bias is swept between +/- 1.5 mV, while a 10 μV ac bias is applied and the a.c. response is measured. The top panel shows a line cut of bias at a backgate voltage of -3.7 V, while the bottom panel shows a colormap finely stepping the backgate voltage.

In Figure 3.4 a trace of conductance versus d.c. bias at a fixed backgate voltage of -3.7 V is plotted. At zero bias, we observe a small, but non-zero, a.c. response from the system. As we increase the d.c. bias in magnitude, the conductance grows quickly, until leveling off after some 'threshold' bias voltage to a value of ~10 μS, close to the value of our edge plateau seen at higher temperatures. We then step the backgate voltage and sweep the bias, holding the temperature constant. We observe broadly similar behavior as a function of gate voltage: very small conductance at zero bias, and an increase in conductance past some threshold bias. We observe mesoscopic fluctuations in both the magnitude of the threshold bias and the value of the conductance, similar to the linear response of the edge states.

3.2.2 *Magnetic field dependence*

Next, we study the effect of an applied magnetic field on the nonlinear conductance. As covered in the previous chapter, the helical edge states of WTe_2 are highly sensitive to magnetic fields, while the bulk conductance is not. We first apply a magnetic field along the z-axis and observe the effect on the conductance in our backgate-bias map. In Figure 3.5, we show data at different fields. We make a few observations with increasing $\boldsymbol{B}$ field: one, the small linear response gets quickly suppressed; two, the threshold bias grows monotonically with increasing field; and three, the mesoscopic behavior of the device with gate voltage becomes more dramatic. The structure of the mesoscopic behavior is not completely repeatable line-to-line, but the overall structure persists upon repeated measurements.

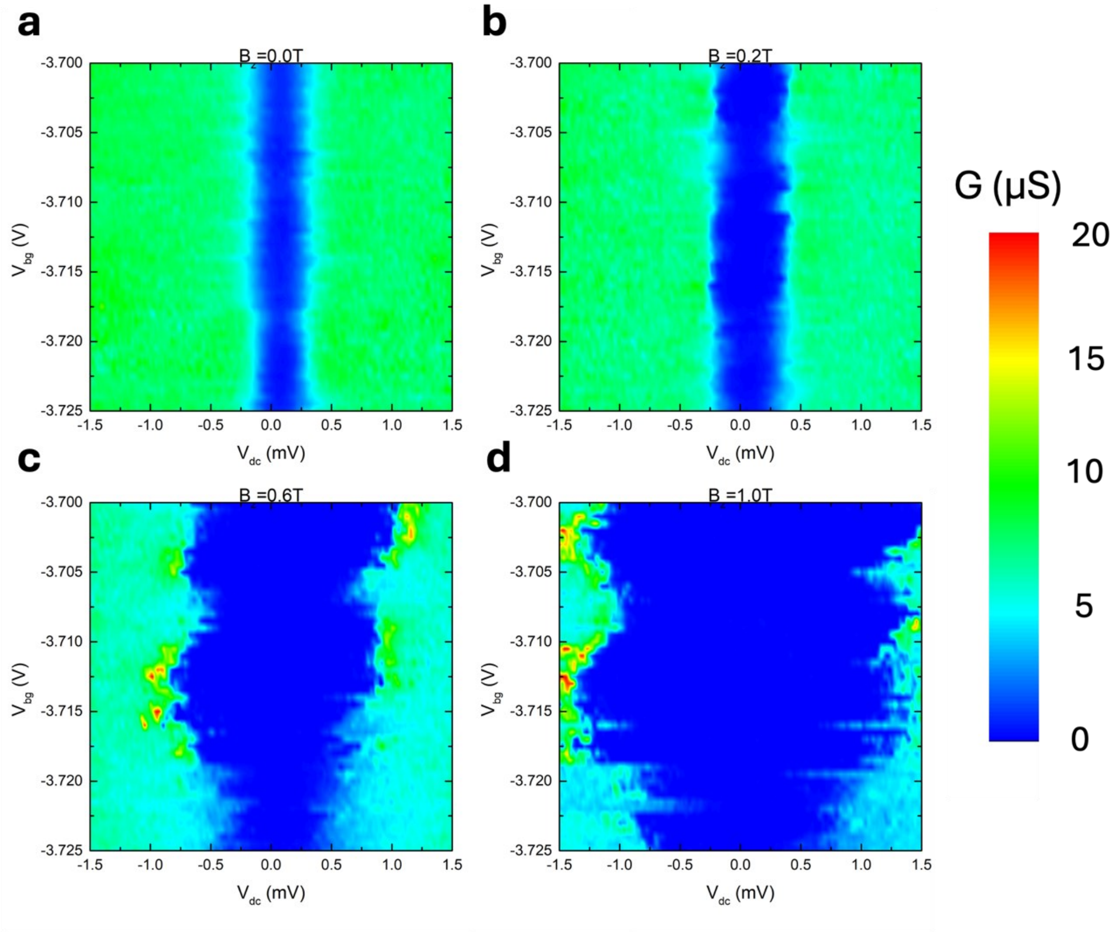

Figure 3.5. Out-of-plane field dependence. The same nonlinear conductance measurement is made at magnetic field values of 0, 0.2, 0.6, and 1.0 T. The threshold bias required to turn on the nonlinear conductance increases with increasing field. The mesoscopics sensitive to the gate voltage are much more prominent with increasing B_z.

Next, we rotate the magnetic field to investigate potential anisotropy in the nonlinear conductance. Taking inspiration from the anisotropy in the linear regime, we proceed as follows: we align the magnetic field 40° from normal to the plane. Since we do not know the crystal axes relative to the magnet axes, we rotate the field around the *z*-axis, maintaining the 40° angle from normal, as shown in Figure 3.6a. We step the angle of the field at constant magnitude, sweeping the d.c. bias at each field orientation, and plot the conductance in Figure 3.6b. We observe a repeating pattern of threshold minima and maxima in φ with period 2π. We hypothesize that this corresponds to the two angles in which the magnetic field is located in the mirror plane of the crystal: when rotating around the z-axis at this angle, it will fall in the mirror plane once while aligned along $\boldsymbol{d}_{\mathrm{so}}$, where the field will have minimal effect on the edge states, then once again 180° away in φ, where the field will be maximally perpendicular to $\boldsymbol{d}_{\mathrm{so}}$ and have the greatest suppression.

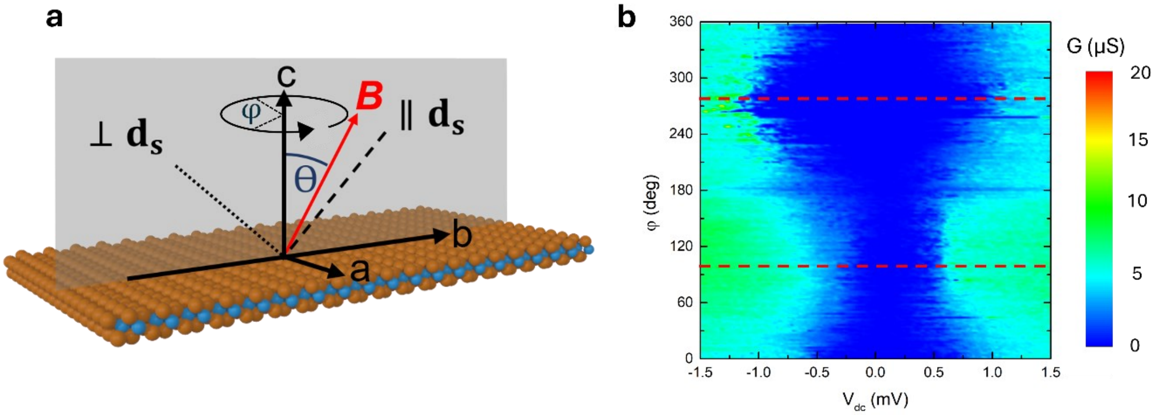

Figure 3.6. Rotation about the z-axis. **a**, The coordinate definitions used for this measurement. We align the magnetic field at θ=40° from normal to the plane. φ is the cylindrical angle about the z-axis, in the magnet's coordinates. **b**, Measurement of conductance stepping φ and sweeping the d.c. bias. The red lines mark the approximate minimum and maximum values of the threshold d.c. bias, occurring at approximately 100° and 280°, respectively. We identify these two angles as the angles in which the field is located within the mirror plane, parallel (for the minimum) to $\boldsymbol{d}_{\mathrm{so}}$ and perpendicular (for the maximum) to $\boldsymbol{d}_{\mathrm{so}}$.

Proceeding under this hypothesis, we align the field at φ=100°, where our threshold voltage is the lowest, and sweep the field in θ, as shown in Figure 3.7a. In the linear regime, we observe π periodicity in this angle, with the field having minimal effect when parallel and antiparallel to $\boldsymbol{d}_{\mathrm{so}}$. In Figure 3.7b. we plot the results of this measurements: we find that the threshold bias is smallest at θ=40° and largest at θ=130°, and repeating with 180° periodicity.

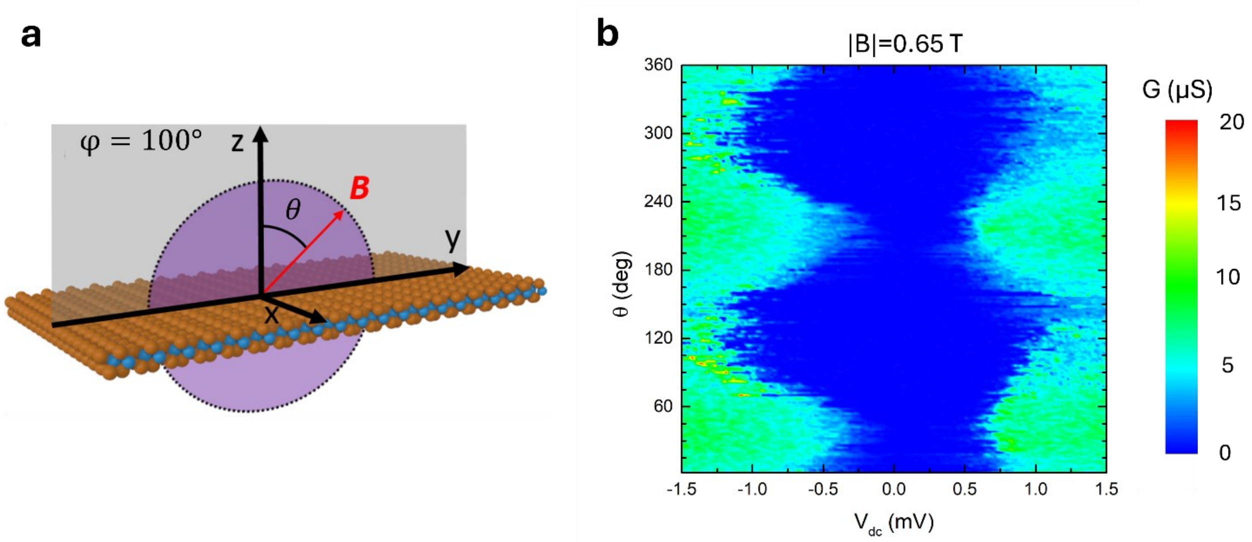

Figure 3.7. Rotation within the mirror plane. **a**, the coordinate definitions used for this measurement. We set *φ*=100° to place the field in the mirror plane, then sweep *θ* from 0° to 360° within the mirror plane. **b**, measurement of the nonlinear conductance versus θ. We observe periodic response in 180° in *θ*, with minima in threshold bias occurring at 40° and 220°, consistent with the field being oriented in the mirror plane and aligning with $\boldsymbol{d}_{\mathrm{so}}$.

In Figure 3.8 we compare the behavior of the system with field strength when aligned parallel to and perpendicular to $\boldsymbol{d}_{\mathrm{so}}$. We step the magnitude of the field and measure the differential conductance as a function of the backgate and bias voltage. We observe that the field has a stronger effect on the threshold voltage when the field is aligned perpendicular to $\boldsymbol{d}_{\mathrm{so}}$, and the mesoscopic behavior is much stronger, in addition to the plateau conductance being lower, compared to the case of aligning the field parallel to $\boldsymbol{d}_{\mathrm{so}}$.

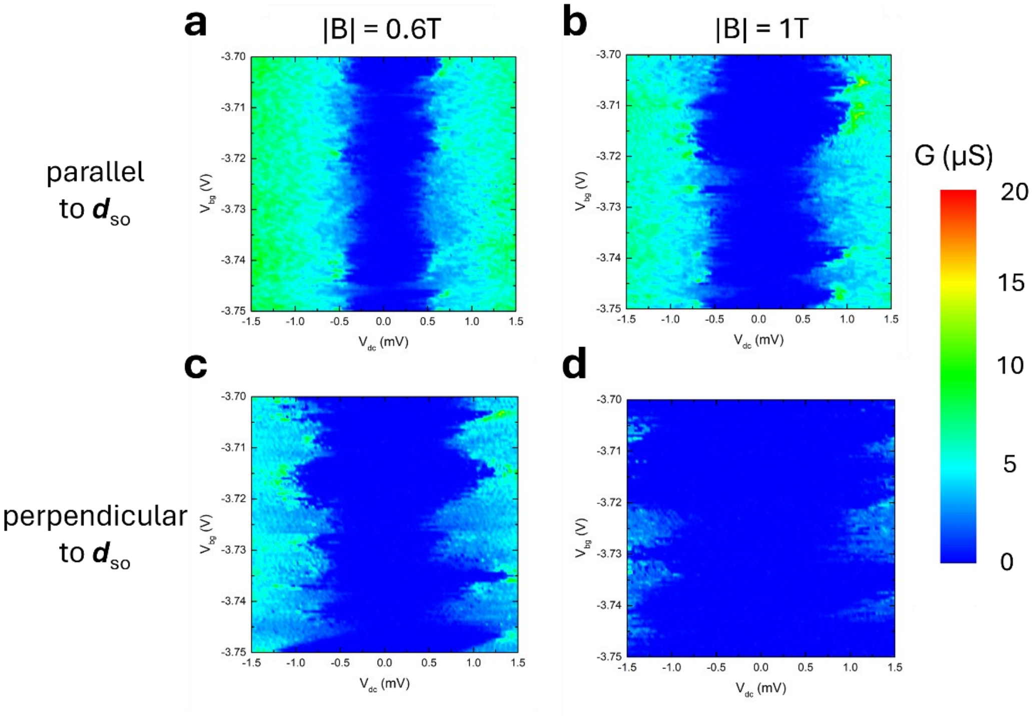

Figure 3.8. Effect of magnetic field oriented parallel and perpendicular to ***d***so. **a**-**b**, nonlinear conductance measured with the field oriented parallel to ***d***so with field magnitudes of 0.6 T and 1.0 T, respectively. **c**-**d**, nonlinear conductance measured with the field oriented perpendicular to ***d***so with field magnitudes of 0.6 T and 1.0 T, respectively. The field suppresses the conductance stronger when oriented perpendicular to ***d***so, and the mesoscopic fluctuations become more pronounced.

In conclusion, we have studied the nonlinear conductance of the edge states of WTe_2 at 100 mK. The edge behavior is sensitive to the mesoscopics of the gate voltage as in the linear regime and is highly sensitive to the presence of a magnetic field. Further, we find that the nonlinear behavior shows anisotropy with the direction of the magnetic field, having a preferred direction 40° from normal, while being maximally suppressed perpendicular to the direction. We identify this axis as ***d***so, defined as in the previous chapter.

Chapter 4. Monolayer WTe_2 in the Ultra-Clean Limit

As condensed matter experimentalists, we are perpetually in search of the highest-quality crystals to get the cleanest picture of the fundamental properties of the material. The science of crystal growth is an entire field upon itself, of which I will not treat here, though I will give a brief overview of the various growth processes to highlight the strides we have made in growing high-quality WTe_2 single crystals.

4.1 CRYSTAL GROWTH

4.1.1 *Flux growth*

The standard growth technique employed for transition metal dichalcogenides is self-flux growth. In a standard flux growth, the constituent elements of the desired crystal are loaded into a crucible alongside a flux medium with a low melting point. The crucible is then heated above the melting point of the flux, dissolving the constituent elements, forming a solution. The crucible is then slowly cooled until the point at which the solution becomes supersaturated, when crystal growth begins. As crystal precipitates out of the solution, the concentration of the constituent elements in the molten flux changes, altering its supersaturation temperature. By cooling slow enough, the growth will trace out a trajectory in the temperature-concentration phase space until no more crystal can grow [78].

The majority of the WTe_2 crystals I have exfoliated during my graduate studies were grown via a Te-rich self-flux as described here. Elemental W powder and Te shot were loaded into crucibles in a 1:50 molar ratio, such that the W melted into a Te flux. The crucible was heated to 1000 °C, just below the melting point of WTe_2, over 12 hours, held at that temperature for 12 hours, then cooled down to 460 °C over approximately 100 hours. At this temperature, the solution is put through a centrifuge to separate the WTe_2 crystal from the Te flux. This procedure regularly produced single crystals of typical dimensions 5 mm × 0.3 mm × 0.01 mm. One gauge of the purity of crystals is from the Residual Resistance Ratio (RRR), the ratio of the resistance at 300 K to the resistance at 0 K. Crystals grown via this flux procedure regularly had RRR values between 800-1200.

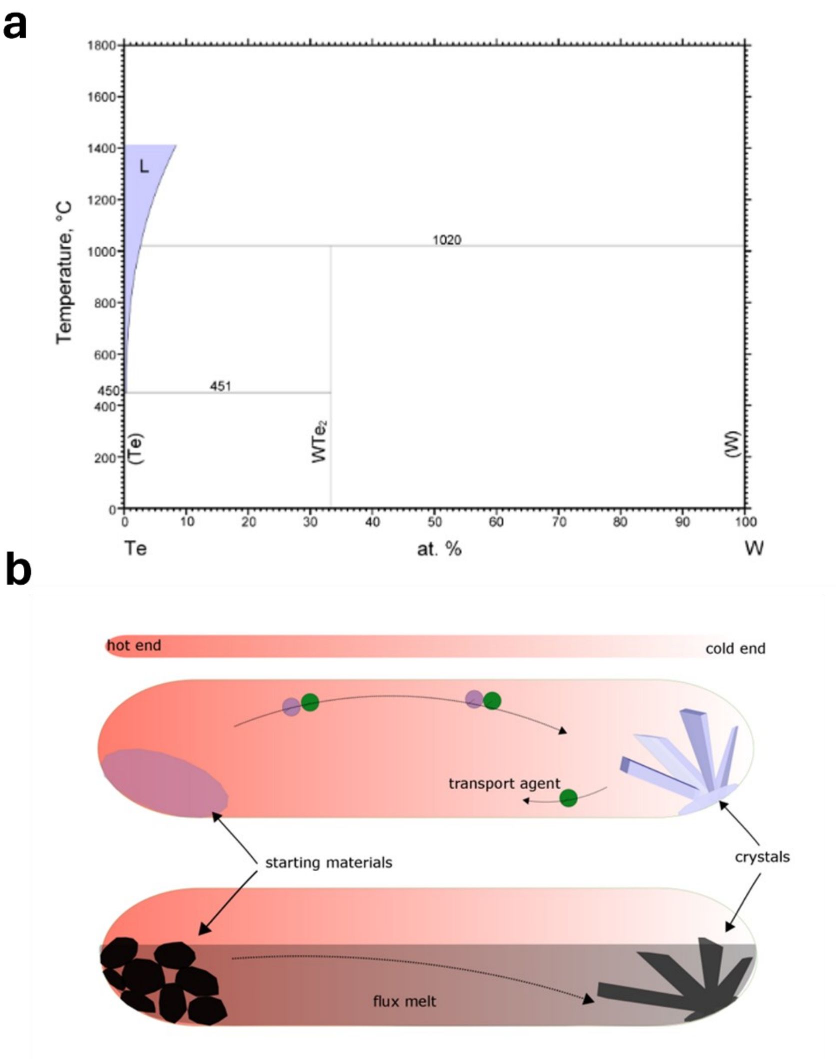

Figure 4.1. Crystal growth techniques. **a**, Crystal growth phase diagram for W-Te. WTe_2 is the only crystal phase in the binary diagram. Reproduced from [79]. **b**, Schematic detailing "horizontal flux growth." A temperature gradient is maintained across the growth chamber, with melted flux (Te) throughout. The starting material (W in this case) is loaded in at the hot end. Some material

will dissolve in the flux and be transported to the cold end, where it will precipitate crystal. Reproduced from [80].

4.1.2 *Horizontal flux growth*

In 2017, Yan et. al. published a paper describing a new technique for flux growths, that they term "horizontal flux growth" [80]. This growth technique has analogues to vapor transport growth. A temperature gradient is maintained across the length of the crucible, above the melting point of the flux such that there is a flux melt throughout. The constituent elements are loaded into the cold end. The flux dissolves the elements at one end and carries them to the cold end, analogous to a vapor transport process, where they can precipitate out into crystal. When mapping out this growth in temperature-concentration phase space (as shown in Figure 4.1a), the trajectory maps out a horizontal line, giving the technique its name.

4.2 SUPERCONDUCTIVITY IN MONOLAYER WTE_2

It has been reported previously by multiple groups [45–47] that at sufficiently low temperatures and sufficiently high electron doping, monolayer WTe_2 will superconduct. This makes WTe_2 one of few gate-tunable 2D superconductors. Other examples of gate-tunable superconductors includes few-layer T_d $MoTe_2$ [81–83], magic-angle twisted bilayer graphene [84], Bernal-stacked bilayer graphene [85,86] and ionic-liquid-gated semiconducting TMDs [87–89]. The ability to tune into and out of a superconducting state with an external gate makes these systems ideal candidates for studying the fundamental physics of superconductors, as well as having promise for technological applications.

We seek to do more detailed follow-up studies on superconducting monolayer WTe_2, though recent attempts to fabricate superconducting monolayer WTe_2 devices with traditional flux-growth crystals have proven fruitless. As exemplified earlier in Figure 3.3, we have made devices that show strong topological edge states and demonstrate bulk conduction while not shown signs of superconductivity. The electron density calculated from the geometric capacitance of our device shows we are several times past the reported doping levels to see metallic behavior, which at millikelvin temperatures should become superconducting. This failure drives our desire to grow higher-purity crystals.

Recently, our collaborators in Jiun-Haw Chu's group at UW have grown WTe_2 crystals using the horizontal-flux growth technique. These have produced crystals with much higher RRR values, ranging from ~1500 to over 3000, indicating higher crystal quality. Given these new high-quality crystals, I fabricated a monolayer device, MW21, in order to study the superconducting state. An optical image of MW21 can be seen in Figure 4.2a. It has dual graphite top- and bottom-gates (outlined in white and black, respectively), and the WTe_2 flake (outlined in red) is contacted by Pt electrodes. The device was measured on a Bluefors dilution fridge with a purported base temperature of ~20 mK and a vector magnet with maximum field magnitudes of 1-1-9 T in the *x*-, *y*-, and *z*-axes, respectively.

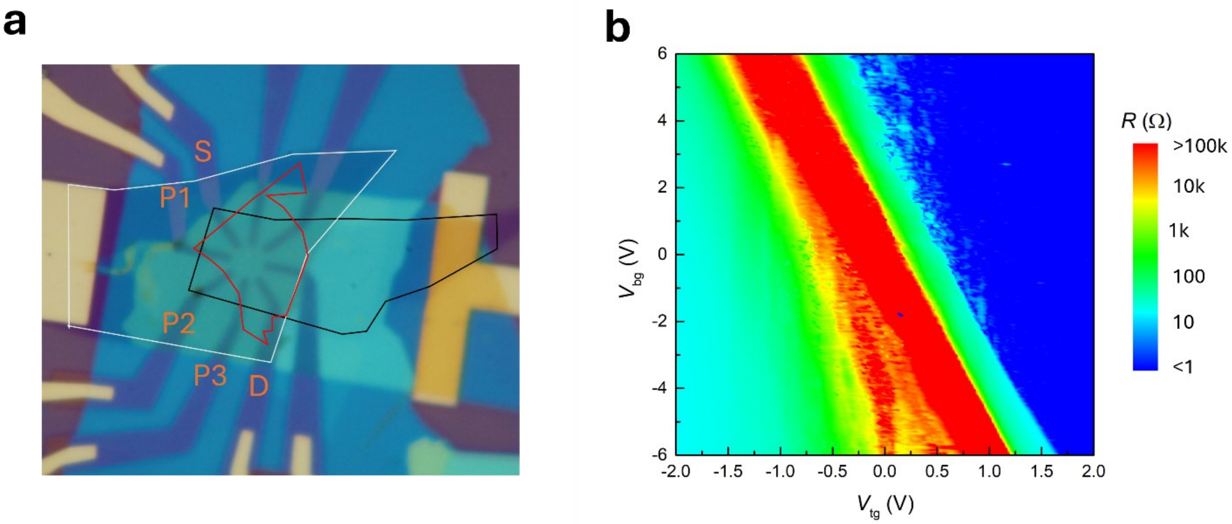

Figure 4.2. Device MW21. **a**, Optical image of the device. Outlined in white is the bottom graphite, and in black is the top graphite. The monolayer WTe_2 flake is outlined in red. The central

region is dual-gated, though portions of the flake are uncovered by the top gate and only gated by the back gate. Contacts labelled S and D were used as source and drain contacts for the current, while contacts labelled P1, P2, and P3 were used as longitudinal voltage probes. **b**, Gate-gate map of the four-terminal resistance of the device at base temperature (~20mK). We observe the quantum spin Hall insulator phase in the red diagonal strip, with resistances becoming unmeasurably large. At moderate electron doping, we observe a sharp drop in the resistance, before dropping beneath the noise floor of our measurement (~1 Ω).

In Figure 4.2b the four-terminal resistance of the device is plotted as a function of the top and bottom gate voltages. A voltage bias of 50 μV is applied between contacts labelled S and D in Figure 4.2a and the corresponding current is measured, while simultaneously measuring the voltage drop between contacts P1 and P2. Dividing the measured voltage drop by the measured current at each point gives us the plotted resistance, in Ohms.

For an electron doping range around charge neutrality, we observe the quantum spin Hall insulator state. At finite hole doping, we observe conduction with resistances of a few kiloohms. And at an electron doping level of about $\sim 3\times10^{12}$ cm^{-2}, we observe a resistance drop down to a noise plateau of ~1 Ohm, which we identify as superconductivity. We observe this resistance drop across all contact pairs in the device; however, we observe contact issues in some pairs such that the resistance value is not of order ~1 Ohm over the entire gate space where $n > \sim 3\times10^{12}$. For this reason, we focus our measurements of the superconducting state in a configuration where we are measuring the voltage drop between contacts P1 and P2.

4.2.1 *Magnetic field dependence*

In order to verify that the resistance drop observed in the device is indeed BCS superconductivity, we apply a magnetic field perpendicular to the plane of the device. Magnetic flux penetrating a superconducting current will generate vortices; for sufficiently high magnetic field values, the total flux will be more than can be compensated for by the formation of vortices, and the superconducting state will break, resulting in a finite resistance measurement. We apply a current bias of 10 nA between contacts S and D, and measure the four-terminal resistance between contacts P1 and P2. In Figure 4.3 the resistance is plotted as a function of the out-of-plane magnetic field, holding fixed the electron density at 12.7×10^{12} cm^{-2} and displacement field D=-0.8 V/nm. We identify a critical transition in magnetic field for field magnitude ~24mT, above which we measure a normal state resistance of ~67 Ohms.

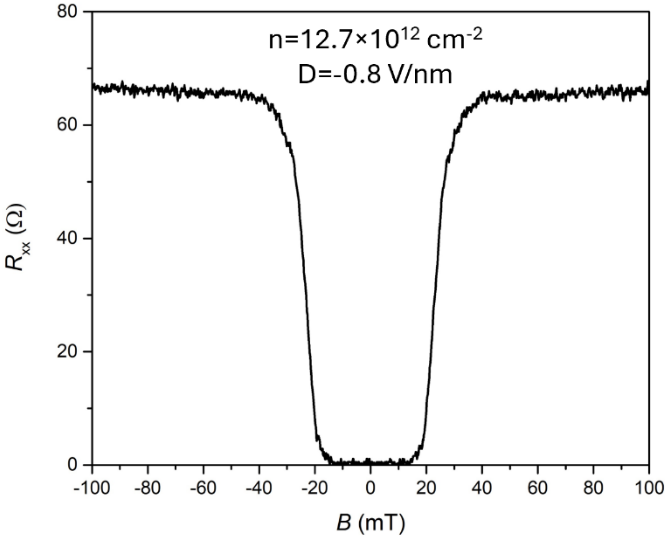

Figure 4.3. Magnetic field response of MW21 at large electron doping. The system is doped to its highest electron doping, $\sim12.7\times10^{12}$ cm^{-2}, with a displacement field of D=-0.8 V/nm. An out-of-plane field is applied, sweeping through zero. We observe critical behavior characteristic of the Meissner effect, with a critical field $R(B_c)=0.5*R_N$ of ~24 mT.

Next, we measure the four-terminal resistance of the device as a function of both electron density and magnetic field, stepping the magnetic field value and sweeping the density from below the superconducting critical density to the maximum value allowed by our gates, plotted in Figure 4.4a. We observe strong density-dependence on the critical field, where, at our lowest temperatures, the critical field rises quickly from our critical density of ~2x10^{12} cm^{-2} up to a maximum value of 150 mT at a density of 4x10^{12} cm^{-2} before falling with increasing density, down to 24 mT at our maximum density value of 12.7x10^{12} cm^{-2}.

To establish the lower bound on critical density of the superconductor, we apply a 500 pA bias to the device, step the electron density, and sweep the out-of-plane magnetic field through zero, plotted in Figure 4.4b. We observe signatures of critical behavior in field down to densities of ~1.2x10^{12} cm^{-2}.

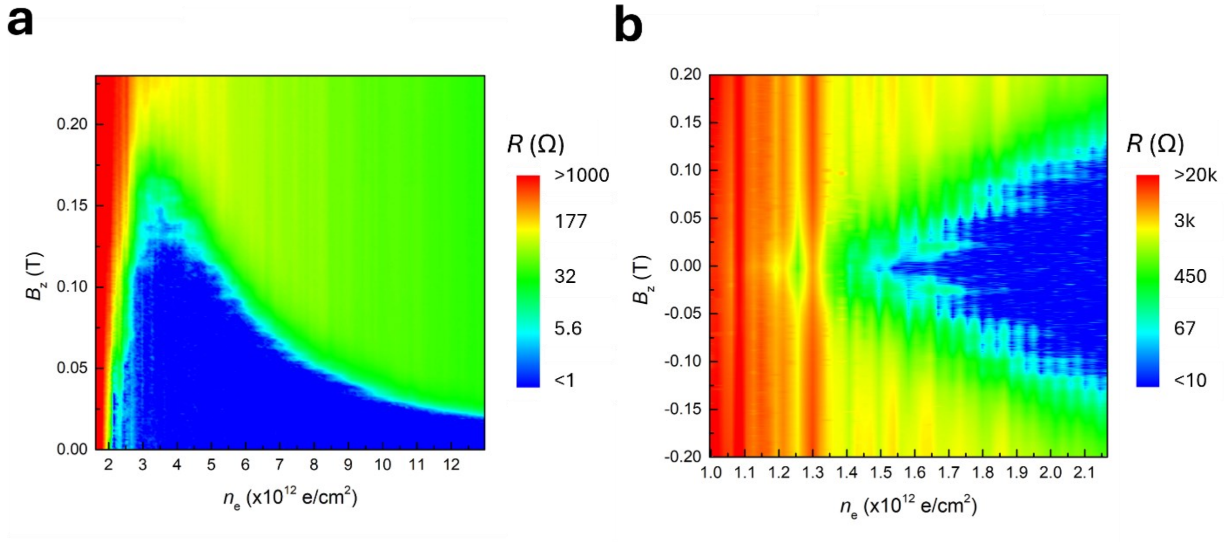

Figure 4.4. Critical field behavior versus doping, at 100 mK. **a**, Four-terminal resistance data taken while stepping the magnetic field and sweeping the electron density. The system begins superconducting at a density <2×10^{12} cm^{-2}. The critical field quickly rises to a value of ~150 mT at 4×10^{12} cm^{-2}, before falling off with increasing density. **b**, We perform another measurement to determine the smallest doping level, n_c, required to induce superconductivity. We apply a 500 pA current bias and measure the resistance, sweeping B through zero while stepping our density. We observe signs of superconductivity down to 1.2×10^{12} cm^{-2}.

This density dependence of the critical field lies in stark contrast to values reported in the literature. Ref. [46] does not report a density-dependence in their critical field measurements, and

Ref. [45] reports a critical field that grows from 0 at their critical density up to a final value of ~30 mT, which is approximately constant upon further electron doping.

The application of a magnetic field larger than our critical field allows us to study the normal state behavior of WTe_2 under these conditions. Bulk conduction in monolayer WTe_2 has very weak magnetoresistance, and as such a 230 mT field applied out-of-plane will dramatically affect the superconducting state but not the metallic state.

With B_{perp}=230 mT we observe monotonically decreasing resistance with increasing electron doping at 100 mK. This behavior can explain the density-dependence of our critical field values: as electron density increases, the diffusion constant of the 2D electron gas will decrease, and the diffusion constant is linearly related to the conductivity of the device. Per Ginzburg-Landau theory, the critical magnetic field supported by a 2D superconductor has this relationship with the diffusion constant [90]:

$$B_c(T) = \frac{\phi_0}{2\sqrt{2}\pi\xi(T)\lambda(T)},$$

where $\xi(T)$ is the coherence length and $\lambda(T)$ is the penetration depth. We observe that the normal-state resistance continues to decrease with increased electron doping, and thus we expect the coherence length to increase. As a result, we expect that by increasing the electron density of our 2D superconductor, we will decrease the critical magnetic field.

We measure the temperature dependence of the critical field behavior versus density, as plotted in Figure 4.5. Data was taken at 0.5 K, 1 K, and 1.4 K. We observe the critical field values decrease for all n_e with increasing temperature. The superconducting density regime shrinks on the low-density side, and by 1.4 K, we observe both a minimum and maximum density under which the device superconducts. Additionally, we observe a shift in the density at which the critical field is highest, from ~4×10^{12} cm^{-2} at 100 mK to ~5×10^{12} cm^{-2} at 1.4 K.

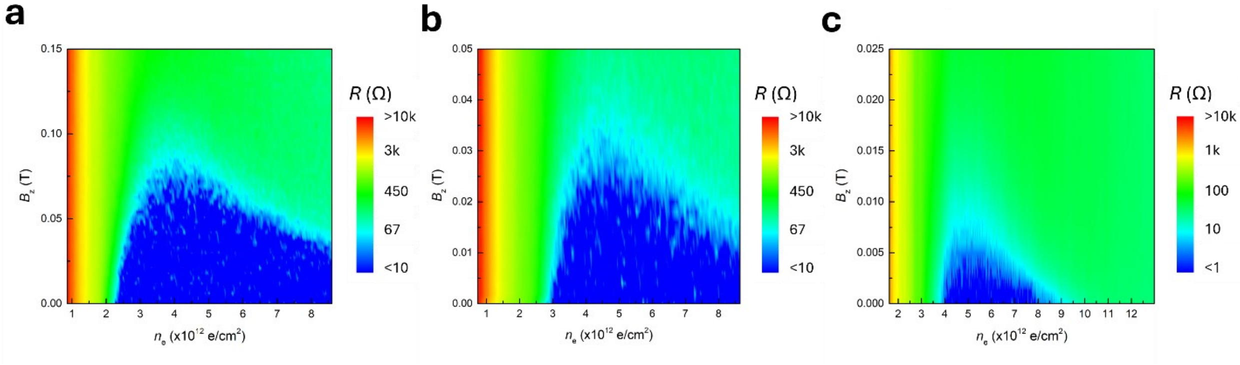

Figure 4.5. Critical field versus doping for a variety of temperatures. **a**, 500 mK **b**, 1 K, **c**, 1.4 K

To get a better measurement of the superconducting dome with respect to temperature and field, we fix the temperature at 1 K, then sweep density and displacement field at fixed magnetic field values. Data for various magnetic field values is plotted in Figure 4.6. As the field is increased, we observe the critical density range decrease on both the lowest and highest ends, until there is no evidence of superconductivity at 50 mT. Furthermore, we note that there is no significant dependence of the superconductivity on the out-of-plane displacement field D.

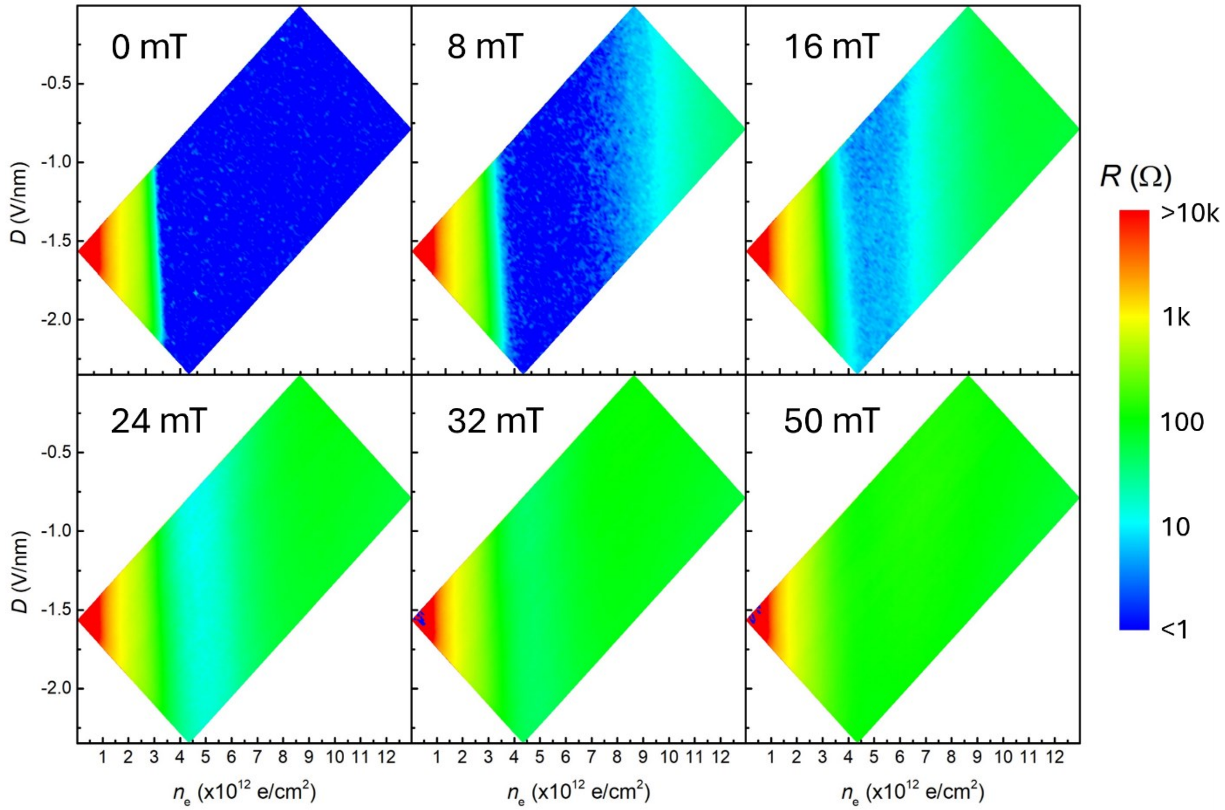

Figure 4.6. Evolution of superconducting state upon application of a magnetic field at 1 K. The superconducting state is most robust to the magnetic field at a moderate doping level of ~5×10^{12} cm^{-2}. No displacement field dependence of the superconducting transition is observed.

We aim to study the effect of the in-plane magnetic field on the superconducting state. The vector magnet in the dilution fridge has a range of +/- 1 T in-plane field. We observe no apparent effect of the in-plane field on the superconducting state up to 1 T. The behavior of the device is consistent with a 1-2° misalignment between the planes of the magnet and sample.

4.2.2 *Critical current measurements*

Next, we study the effect of the critical current on the device. We configure a differential resistance measurement, where we apply a d.c. current bias in addition to a small a.c. current bias and measure the four-terminal a.c. response of the device. By sweeping the d.c. current, we can identify when the superconducting state is unable to support more current by measuring a non-zero response in the a.c. resistance. We fix the electron density of the system and scan the d.c. current from -800nA to +800nA while applying a 1 nA a.c. current at a frequency of 13.777 Hz. The resulting a.c. resistance measurement is plotted in Figure 4.7. We observe an approximately linear relationship between the electron density in the system and the critical current that the superconductor can support. The maximum critical current the system can support tracks to zero near a density of ~1.5x10^{12} cm^{-2}, consistent with the small-bias magnetic field-dependence data.

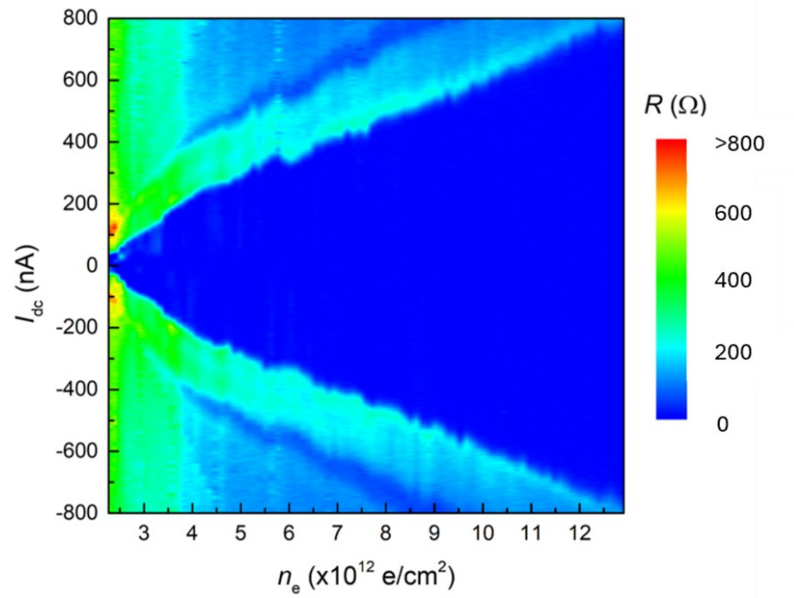

Figure 4.7. Critical current versus density. A small a.c. current is applied (1 nA) while the d.c. current is swept, and the four-terminal a.c. resistance is measured at each electron density. The critical current increases roughly linearly with increasing electron density. The critical density can be estimated by the point at which the critical current tracks to zero. This value is ~1.5×10^{12} cm^{-2}, consistent with the critical field measurement for determining the critical density. Measurement performed at 100 mK.

In Figure 4.8 we show results of measuring the critical current against an applied out-of-plane magnetic field, at a fixed electron density of 12×10^{12} cm^{-2}. In this measurement, we step the magnetic field and sweep the d.c. bias. We make note of a few things from this measurement: one, the dependence of the critical current on increasing magnetic field is roughly linear; two, we observe no signs of Fraunhofer oscillations, suggesting the device is uniformly superconducting, with the supercurrent flowing without forming Josephson junctions in the device. We conduct a similar measurement at an electron density of 5.33×10^{12} cm^{-2}, as plotted in Figure 4.9a. The shape of the superconducting boundary is markedly different at this lower density than higher, forming a concave pattern as opposed to a linear one at higher density. We do not understand the difference in observed behavior.

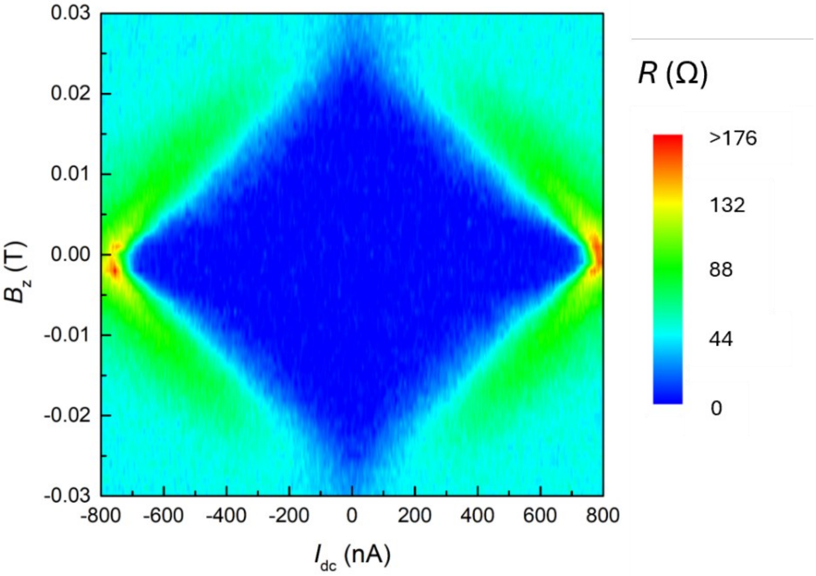

Figure 4.8. Critical current versus magnetic field. Measurement shows no Fraunhofer oscillations, suggesting a uniformly superconducting device. Electron density for this device is 12×10^{12} cm^{-2}.

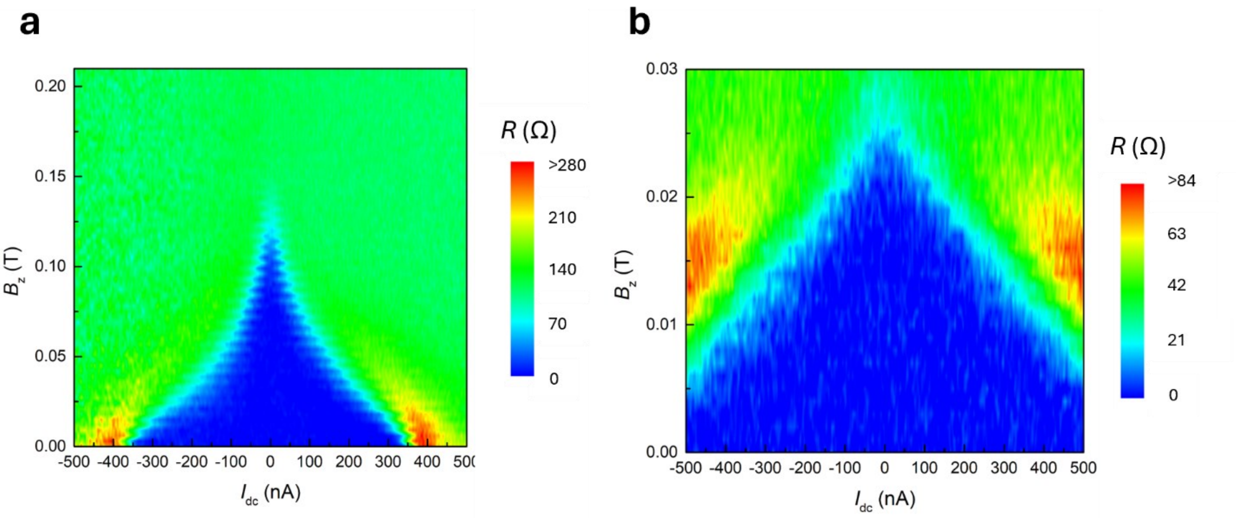

Figure 4.9. Critical current versus magnetic field at different densities. **a**, critical current measured versus field at an electron density of 5.33×10^{12} cm^{-2}. **b**, critical current versus field at 12×10^{12} cm^{-2} for comparison.

4.2.3 *Temperature dependence*

WTe_2 has previously been reported to have strong temperature dependence on its critical doping level. In Refs. [46] and [47], the critical doping level required, at the coldest temperatures, to reach the superconductor transition is ~5-7x10^{12} cm^{-2}. As the temperature is increased, this critical doping value is reported to increase monotonically, requiring larger and larger doping levels to achieve superconductivity.

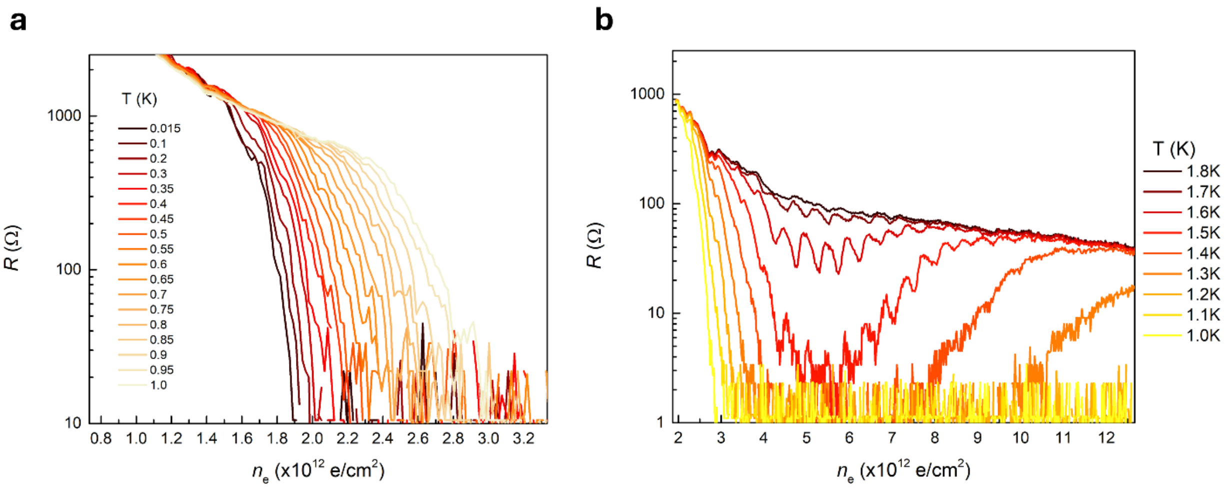

Figure 4.10. Resistance versus temperature as a function of electron doping. **a**, Temperature dependence at both low temperatures and doping. We observe the critical density for the onset of superconductivity increasing monotonically, but the temperature dependence is much weaker than previously reported. **b**, Temperature dependence above 1 K over the full range of electron doping. The minimum critical density increases further past 1 K. Above 1.2 K, a maximum critical density becomes visible. At 1.8 K, little signs of superconductivity remain. Oscillations in the data are due to fluctuations in the temperature.

Here, we report a much weaker dependence of the critical density on the temperature. In Figure 4.10a we show sweeps of resistance versus density at low densities. We observe a monotonic increase in the density required to observe superconductivity, but below 1 K, our critical density is still below the previously reported values for n_c at millikelvin temperatures. Furthermore, as we warm the system further, we observe a maximum critical density emerging, observable in this device for temperatures above 1.2 K, shown in Figure 4.10b. As we warm further, superconductivity remains only for a narrow regime of doping around 5×10^{12} cm^{-2}. In Figure 4.11 we plot the critical temperature against the doping level. We observe a qualitatively similar trend to the behavior of critical field against doping, where it initially grows quickly, peaking around 5×10^{12} cm^{-2}, before falling as the density is increased further. At 1.8 K, we observe no signs of superconductivity at any density.

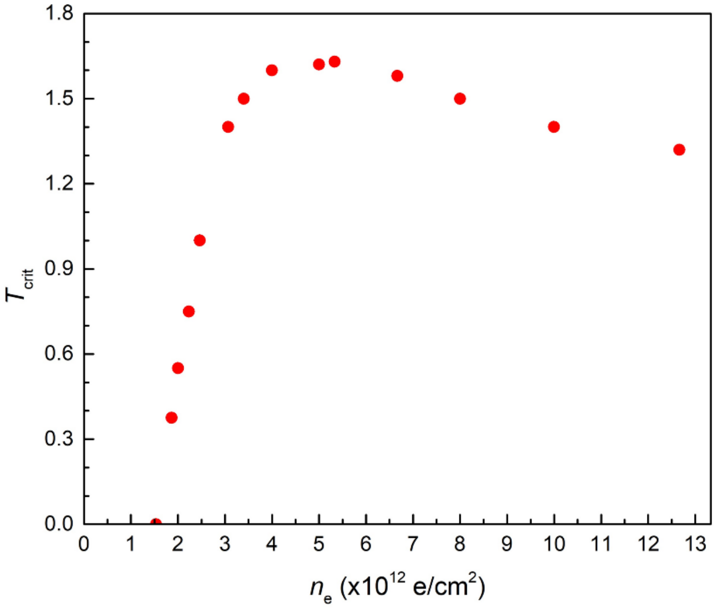

Figure 4.11. Critical temperature versus density. Critical temperature is extracted from the temperature dependence, defining T_c as the temperature where R=0.5*R$_N$.

We further measure the dependence of critical field against temperature at fixed doping levels. We calculate the critical field at each temperature and density. Ginzburg-Landau theory predicts that there should be a linear relationship between the critical field and critical temperature. By fitting our critical field values linearly in temperature, we can get an estimate of the critical temperature by the point where the critical field goes to zero. Plotted in Figure 4.12 are the extracted critical fields versus temperature, and the linear fits in temperature. We find good correspondence between the critical temperature derived this way in addition to the zero field temperature measurements.

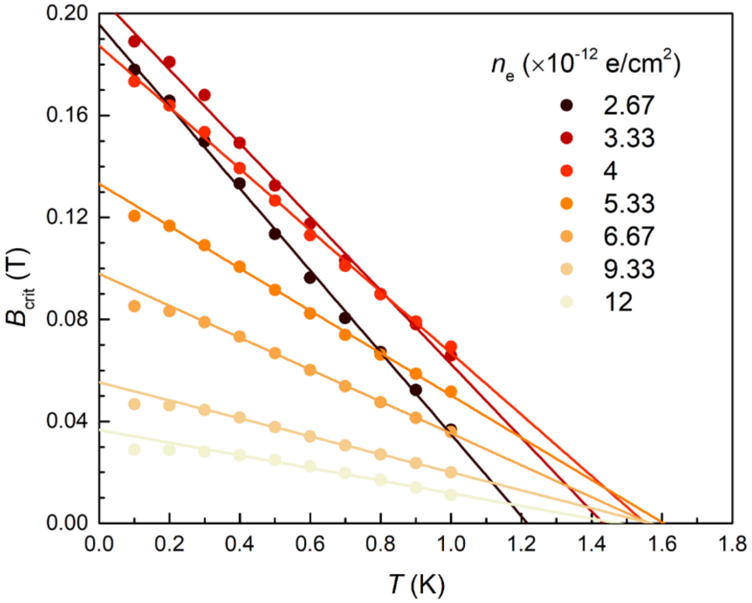

Figure 4.12. Critical magnetic field versus temperature at different electron doping levels. Linear fits are applied for the higher temperature data (>0.6 K). The x-intercept of each line can be used to estimate the critical temperature at each doping level, and gives similar results to the critical temperature curve above.

There has previously been debate about whether a metallic state lies between the quantum spin Hall insulator state and the superconducting state as a function of doping. Plotted here in Figure 4.13b is resistance data near and below the superconducting transition point. We observe a region ~0.7×10^{12} cm^{-2} wide in density in which there is very weak temperature dependence, evincing the presence of a metallic state between the insulator and superconductor in this device.

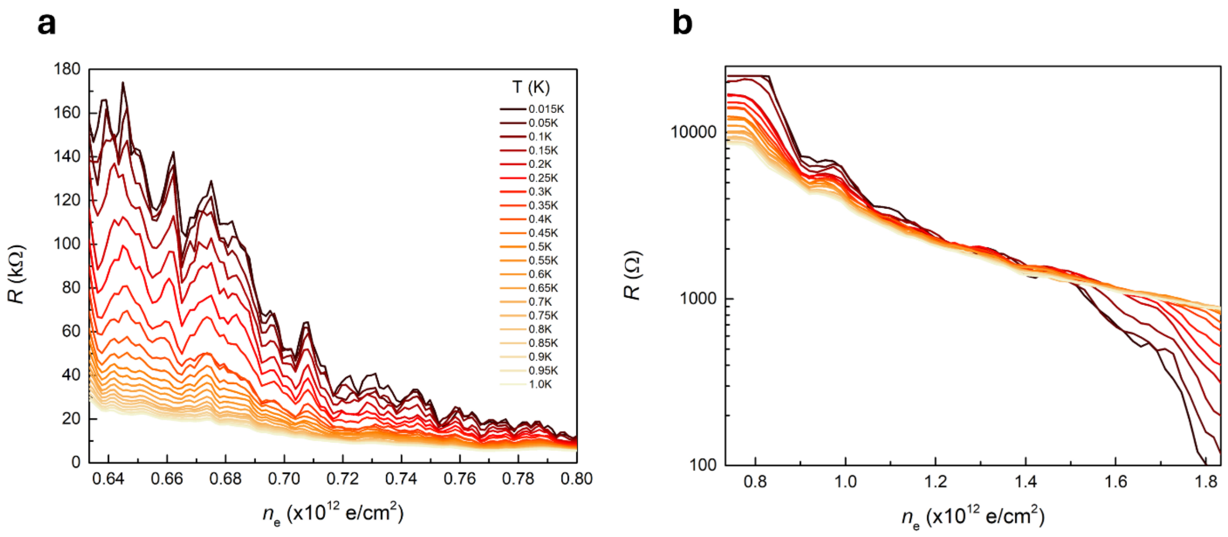

Figure 4.13. Temperature dependence below the critical density. **a**, Below ~1.5×10^{12} cm^{-2} we observe insulating behavior. **b**, Between 1.0×10^{12} cm^{-2} and 1.4×10^{12} cm^{-2} we observe very weak temperature dependence, evidence of the existence of a metallic state between the insulating regime and the superconductor.

4.3 HALL MEASUREMENTS

Given the resiliency of the superconducting state in this device, we set out to measure the Hall effect in order to learn more about the metallic normal state of monolayer WTe_2. There has previously been controversy about the existence (or not) of Shubnikov-de Haas (SdH) oscillations in WTe_2 [31,91,92]. Here, we present incontrovertible evidence of SdH oscillations in monolayer WTe_2 upon both hole and electron doping.

4.3.1 *Shubnikov-de Haas oscillations*

At sufficiently low temperatures and high magnetic fields, the Hamiltonian of a 2D electron gas will become quantized with a form analogous to a simple harmonic oscillator, forming discretely spaced energy levels known as 'Landau levels'. The energy spectrum of these levels goes as:

$$E_n = \hbar\omega_c\left(n + \frac{1}{2}\right),$$

where $\omega_c = \frac{|qB|}{m}$. We can immediately see that as we increase **B**, the energy of each level as well as the spacing between levels will increase [1]. We can observe signatures of the Landau levels in the transport data. At fixed magnetic field, as we sweep the gate voltage (controlling the Fermi level) we will sweep in and out of the Landau levels: when within a Landau level, the partially-filled band will lead to increased conductance, while when between levels, we will observe increased resistance. Similarly, at a fixed gate voltage, sweeping the magnetic field will move the Landau levels through the Fermi energy, seeing oscillating conductance maxima and minima as the Fermi energy is within and between bands, respectively. As such, we can track individual Landau levels as they disperse in field-energy space, each level "fanning" away from the origin.

In Figure 4.14 we plot the resistance as a function of electron density and displacement field with a magnetic field of 9 T applied. In the hole-doped regime, we observe vertical yellow stripes characteristic of SdH oscillations. These features appear consistently over the entire range of displacement field. On the electron side, we observe two distinct sets of vertical lines: one centered around D=0 V/nm and another at D=-1.4 V/nm, with a region without any noticeable lines in between. We attribute this change to a Rashba splitting effect induced by the displacement field, similar to the effect observed by Shcherbakov et. al. in work done on InSe thin films [93].

We note that the spacing of the lines on the electron side is twice that of the lines on the hole side- the separation in the electron oscillations correspond to a degeneracy of four, while the hole oscillations correspond to a degeneracy of two. This is consistent with the band structure of monolayer WTe_2, as there are two symmetric conduction bands (with two electrons each) near the Fermi surface, while there is one valence band near the Fermi surface.

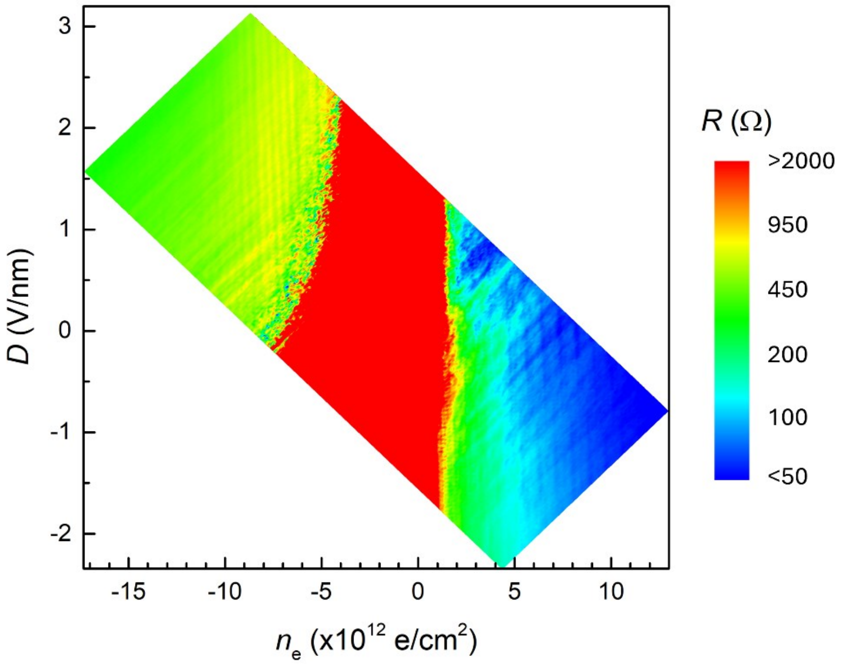

Figure 4.14. Longitudinal resistance versus electron density n_e and displacement field D under a perpendicular magnetic field of 9 T at 100 mK. Above an electron doping of ~5×10^{12} cm^{-2} we observe two sets of vertical stripes: one set centered around D=0 V/nm and the second around D=-1.4 V/nm, with a region without any apparent stripes separating them. Under a constant field, these vertical features are evidence of SdH oscillations. Additionally, in a window of hole doping from ~5 to 10×10^{12} cm^{-2} we observe evidence of SdH oscillations with half the energy spacing as on the electron side.

Motivated by the distinct set of oscillations, we study the SdH oscillations as a function of magnetic field and electron density at fixed displacement fields of D=0 V/nm and D=-1.4 V/nm. In Figure 4.15a, we plot the raw resistance data of the so-called "Landau fan" for D=0 V/nm. We observe features SdH oscillations in dispersing with increasing ***B*** and *n*. In order to confirm that these oscillations are intrinsic to the WTe_2 and not an artifact originating from elsewhere, we extrapolate the trajectory of the features to their meeting point. In Figure 4.15b we plot the resistance data with a linear fit in $\boldsymbol{B}$ subtracted at each value of n, in order to highlight the oscillations. We then superimpose lines, labelled by ν, defined as $\nu = \frac{n}{B\phi_0}$, where ϕ_0 is the magnetic flux quantum. We trace out the set of lines for the low-resistance (blue) features, and label them by the value of ν. We are able to identify features starting at ν = 18 increasing by multiples of 4, which is consistent with the expected degeneracy of WTe_2. These lines meet at zero field close to the calculated geometric density of 0, confirming them originating intrinsically from the WTe_2.

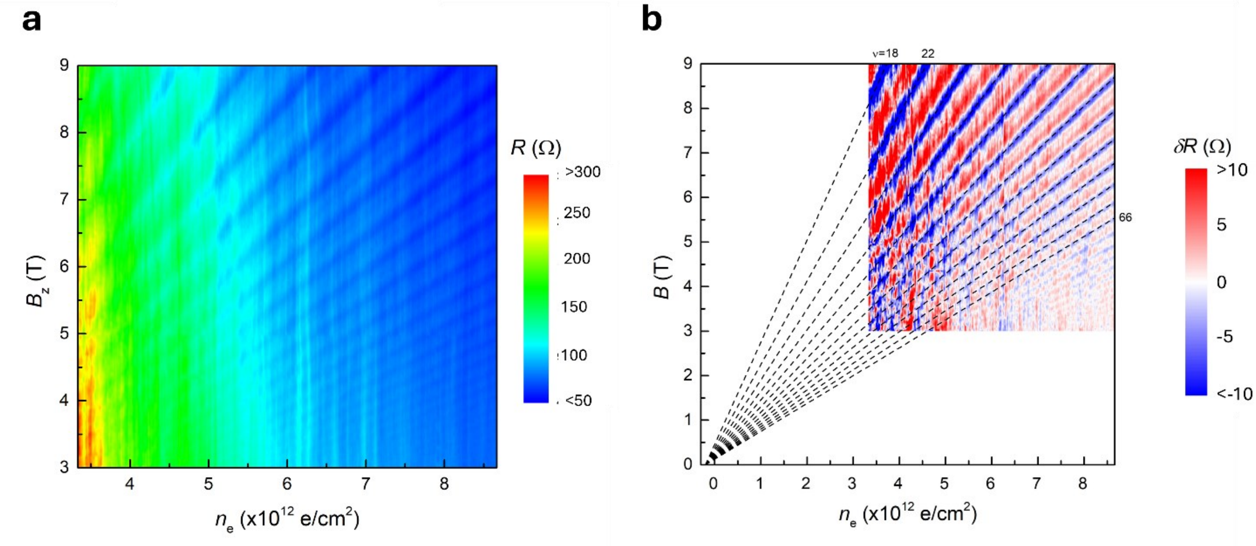

Figure 4.15. Landau fan of electron doping taken at a constant displacement field of D=0 V/nm. **a**, Raw longitudinal resistance data as a function of electron doping and magnetic field strength. **b**, The resistance data from **a** is taken and at each density level, a linear fit in B is calculated then subtracted from the data to emphasize the oscillatory behavior. Plotted is the difference between the raw data and the linear fit over the range of 3-9 T. Lines are superimposed on the plot that correspond to SdH oscillations parameterized by ν, ranging in value from 18 upwards with a step size of 4. The lines extrapolate to zero at a geometric density of $\sim$-2×10^{11} cm^{-2}.

We take an identical measurement at D=-1.4 V/nm, shown in Figure 4.16. We again can identify fan features that trace back near the origin. While the features in the D=0 V/nm fan are consistent along their trajectory, we observe different behavior here. We observe features fanning out from more resistive states to less resistive states upon increasing field and doping. More careful study and analysis of the behavior of the SdH oscillations away from D=0 is needed moving forward.

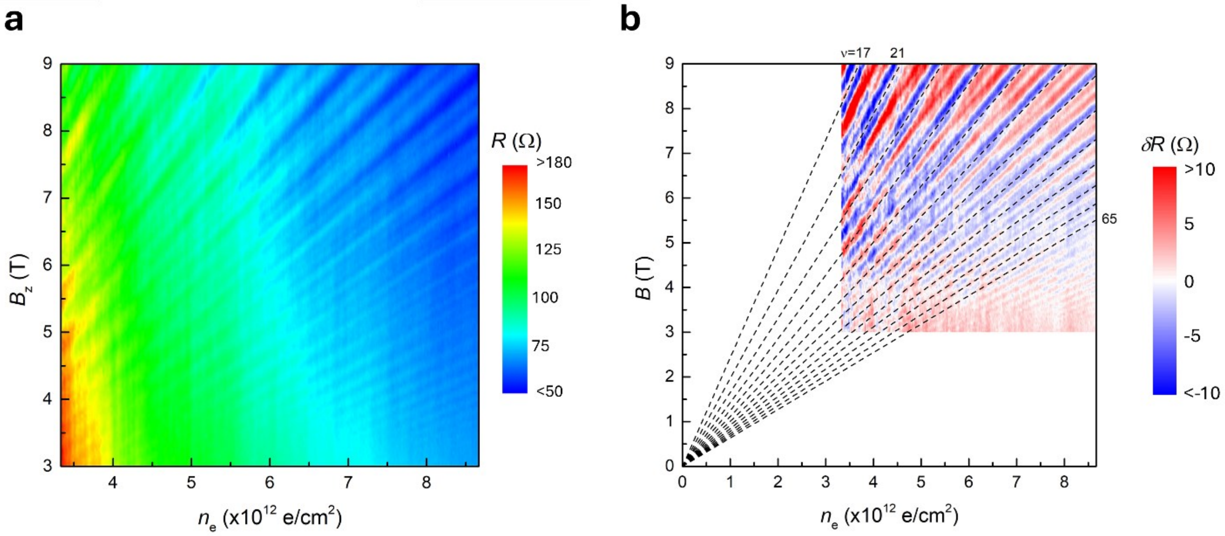

Figure 4.16. Landau fan of electron doping taken at a constant displacement field of D=-1.4 V/nm. **a**, Raw longitudinal resistance data as a function of electron doping and magnetic field strength. **b**, The resistance data from **a** is taken and at each density level, a linear fit in B is calculated then subtracted from the data to emphasize the oscillatory behavior. Plotted is the difference between the raw data and the linear fit over the range of 3-9 T. Lines are superimposed on the plot that correspond to SdH oscillations parameterized by ν, ranging in value from 17 upwards with a step size of 4. The behavior at moderate fields is qualitatively different than at D=0 V/nm. The high-field behavior extrapolates to zero at a density of 0.

4.4 EDGE STATE AND EXCITONIC INSULATOR

Lastly, we study the edge states and the excitonic insulating bulk state. In previous devices, the edge state forms a plateau that develops when the bulk goes insulating at 100 K, down to <10 K, at which point the edges begin to freeze out. For these measurements, we choose a pair of contacts that is connected by one straight edge of the flake. All possible edge lengths are long in this device

(>3 μm each), so we expect the behavior of the edges to be more resistive than the quantized conductance value of $2\frac{e^2}{h}$. In Figure 4.17a, we plot the temperature dependence of the linear edge conduction as a function of top gate voltage. The topological protection of the edges should make the edge behavior robust against the crystal quality. We observe qualitatively similar behavior: the edge plateau begins to form at 100 K, and keeps a good plateau to 10 K, at which point it starts to freeze out. In Figure 4.17b we plot the linear conductance of the edge at 1 K as a function of back gate voltage. We observe peaks in conductance as the back gate voltage is swept, typical of the mesoscopic behavior that governs the edge conductance. In previous devices, the mesoscopic behavior is mostly reproducible, but tends to drift over time. In this device, we observe extremely reproducible mesoscopic behavior at 1 K. The mechanisms that dominate the mesoscopic behavior of the edge conduction are as of now not well theoretically understood; further studies are needed to understand it more completely, but having devices with highly reproducible mesoscopic character provides a platform for consistent study of the edges.

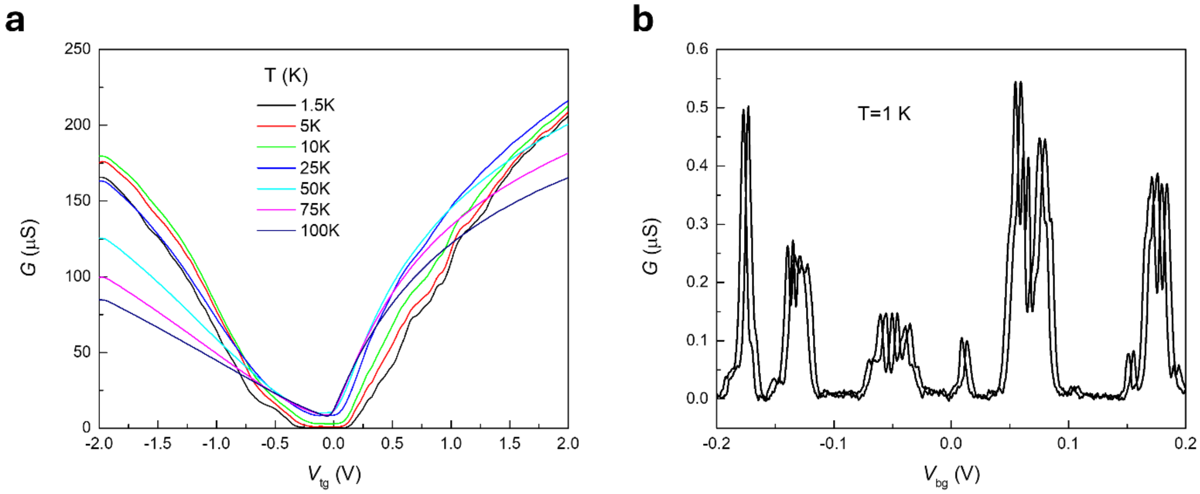

Figure 4.17. Linear edge conduction in MW21. **a**, Temperature dependence of the edge conduction as a function of top gate voltage. The behavior here is consistent with previous devices.

b, Edge conduction at 1 K as a function of back gate voltage. The reproducibility of the mesoscopic behavior is unique to MW21 compared to previous devices.

We further study the behavior of the edges at 100 mK. Since the edges fully freeze out at this temperature, we study the nonlinear conductance of the edges as discussed in Chapter 3. We sweep a d.c. voltage bias on top of a small a.c. bias and measure the a.c. response at fixed gate voltages. In Figure 4.18a, we plot the a.c. conductance versus gate and d.c. bias. We observe mesoscopic behavior as a function of gate voltage as seen previously. Many of these mesoscopic features on either side of zero bias seem to follow a similar trajectory. This behavior is reminiscent of the behavior of quantum dots, where the charging energy of the dots creates diagonal features in energy-bias space.

We further study the magnetoanisotropy of the edges in the nonlinear regime. Following the procedure outlined in Chapter 3, we locate the mirror plane of the WTe_2 and orient the field along $\boldsymbol{d}_{\mathrm{so}}$. In Figure 4.18b, we plot the same measurement of conductance versus bias and gate with a field of 0.8 T applied along $\boldsymbol{d}_{\mathrm{so}}$. We observe only a slight increase in the threshold bias required to pass current through the edges. The mesoscopic structure of the gate dependence has been altered some. Different 'peaks' in gate voltage show varying levels of sensitivity to field, though the overall structure of the gate dependence is very similar. Finally, we rotate the field in the mirror plane so that it is perpendicular to $\boldsymbol{d}_{\mathrm{so}}$, shown in Figure 4.18c. As in Chapter 3, we observe a much larger increase in the threshold voltage, and the mesoscopic structure is changed more dramatically than when the field is aligned parallel to $\boldsymbol{d}_{\mathrm{so}}$.

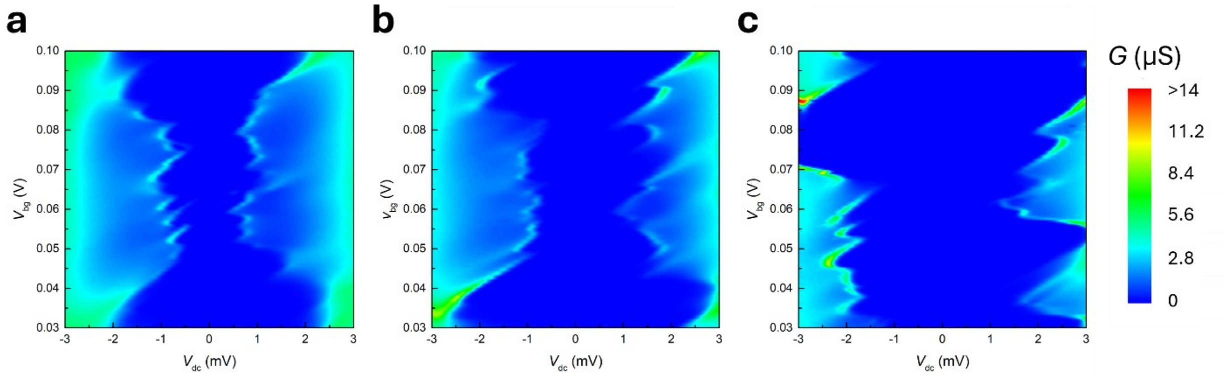

Figure 4.18. Anisotropy of the nonlinear edge conductance of MW21. **a**, Zero field measurement of nonlinear conductance. Diagonal features in the bias-gate space are reminiscent of behavior seen in quantum dots. **b**, Nonlinear measurement taken with 0.8 T applied parallel to $\boldsymbol{d}_{\mathrm{so}}$. **c**, Same measurement taken with 0.8 T field applied in the mirror plane perpendicular to $\boldsymbol{d}_{\mathrm{so}}$. All data taken at 100 mK.

Lastly, we report on studies of the bulk conductance at temperatures above the superconducting critical temperature. In this measurement, we study the two-terminal response between contacts located on opposite sides of the device. We ground the other pins in order to prevent parallel conduction through the edge states; the current path is restricted through central channel of the device. In Figure 4.19a we plot the conductance versus top gate voltage as a function of temperature. Below ~100 K, we observe the conductance going to zero over a range of gate voltage where an edge plateau would be expected, confirming that there is no current flowing through the physical edges nor internal cracks connecting the two contacts. Previous reports have noted metallic behavior for the electron-type carriers in monolayer WTe_2 and insulating behavior for the hole-type carriers. We observe increasing conductance with decreasing temperature on the electron side, as expected, though surprisingly we also observe metallic temperature dependence on the hole side. The observation of quantum oscillations on the hole side as well as metallic temperature behavior suggests the hole conduction is highly sensitive to the crystal quality of the WTe_2.

In Figure 4.19b we zoom in on the apparent neutrality point of the WTe_2. One of the main transport signatures of the excitonic insulator state of WTe_2 is the sharp ‘V’ in conductance at high temperatures. In this device, we see this ‘V’ shape appear in the 98 K trace, consistent with the value reported in the literature. The bottom of the ‘V’ spans roughly 20 mV in top gate voltage, which corresponds to a change in density of $<1\times10^{11}$ cm^{-2}.

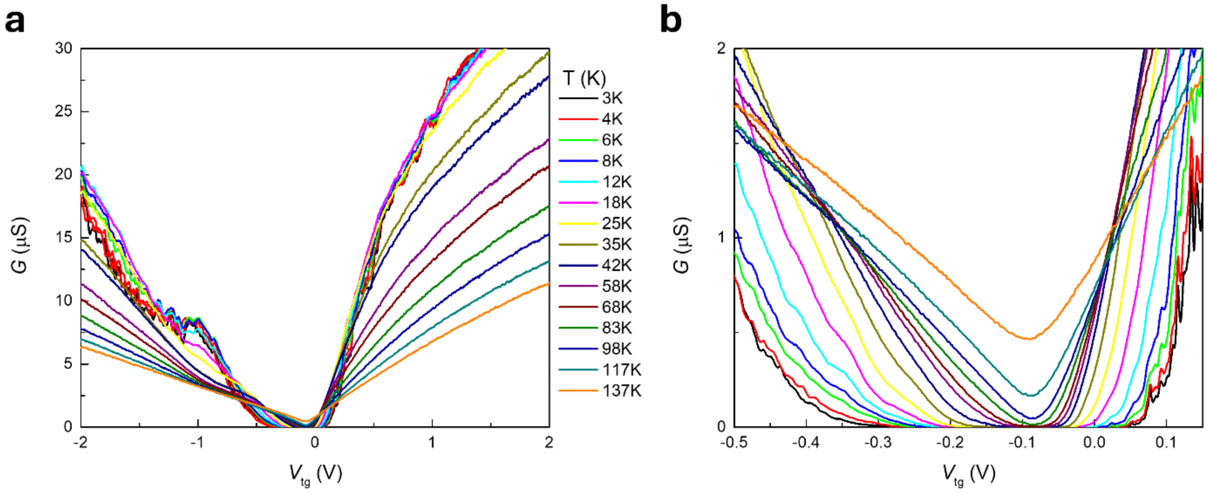

Figure 4.19. Temperature dependence of the WTe_2 bulk. **a**, Temperature dependence of the WTe_2 bulk over the full range of top gate voltage. Metallic behavior is observed on both the electron and hole side. **b**, A zoom-in of the bulk temperature dependence near the apparent neutrality point. We observe a sharp ‘V’ shape forming over a range of only ~20 mV, characteristic of the excitonic insulator behavior of the bulk.

4.5 CONCLUSION AND OUTLOOK

In this chapter, we investigated the transport properties of monolayer WTe_2 devices made from much higher-quality crystals. We observe superconductivity at higher temperatures than has ever been reported in the literature, with a critical density that is much smaller than previous reports.

We find that the critical field required to kill the superconducting state can be tuned dramatically with the electron doping of the system, and that the highest critical field and critical temperature occurs at a moderate doping level.

We also establish the presence of quantum oscillations in WTe_2 on both the electron and hole side. We see effects of Rashba splitting on the Landau fan as we tune the displacement field away from zero. The effect of the displacement field on the oscillations requires more study than was allotted here. Finally, we see that both the electron and hole carriers display metallic temperature dependence.

Chapter 5. Further Studies on Few-Layer WTe_2

Given the results of the previous chapter, there is strong reason to believe there is still much yet to be learned about WTe_2. In this chapter, I will provide some intriguing results from other experiments on WTe_2 that suggest further paths of study, especially given the new high-quality crystals.

5.1 BILAYER WTe_2 UNDER EXTREME CONDITIONS

Bilayer WTe_2 is a topologically-trivial ferroelectric metal. Unlike in its monolayer form, bilayer does not have inversion symmetry; as such, it permits a polar axis. Around charge neutrality it demonstrates insulating behavior, while upon electron doping it undergoes an insulator-to-metal transition [50].

The nature of the insulating state in bilayer WTe_2 is not well-understood. We would like to probe the nature of the insulating state to investigate for correlated behavior as is seen in monolayer [48,49]. I made a bilayer WTe_2 device with graphite contacts in order to study its electronic properties at millikelvin temperatures in the dilution fridge.

In Figure 5.1a I show four-terminal resistance data for the device at 1 K. We note a few interesting features in the resistance data. One, we can observe signs of the ferroelectric switching at $\sim E_\perp=0.07$ V/nm for the sweep direction in this dataset. Strangely, we see moderate resistance around charge neutrality and $E_\perp=0$ V/nm; upon application of a perpendicular electric field, the resistance grows sharply to immeasurably large values. However, in this device we see the resistance then decrease upon increasing the field further. At the highest values of electron doping we see a metallic state, but observe no signs of a superconducting transition.

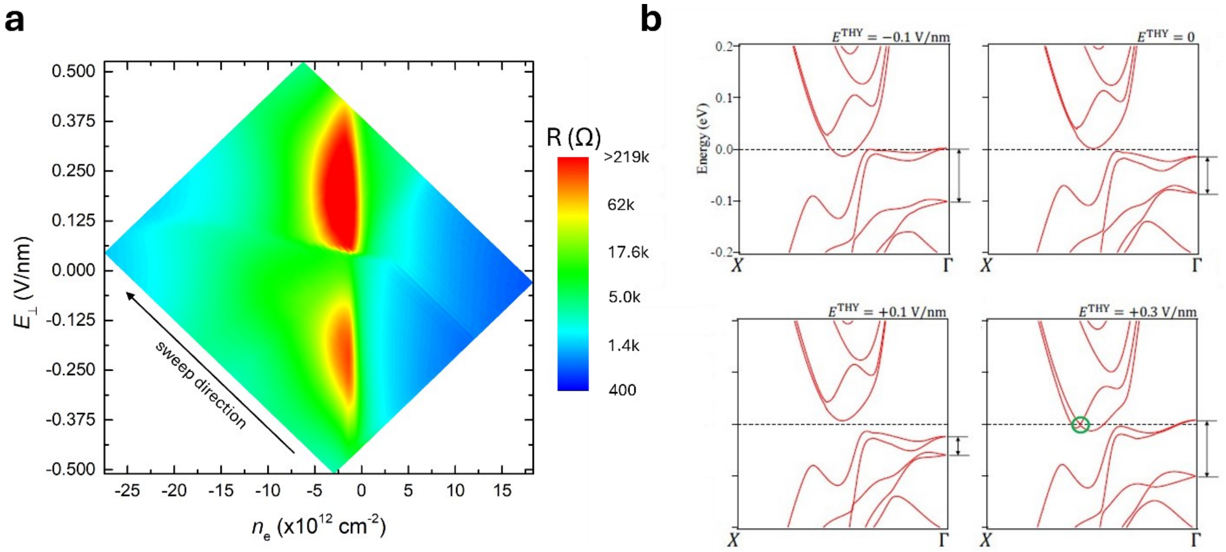

Figure 5.1. Resistance of bilayer WTe_2 at 1 K. **a**, A gate-gate map of resistance. The two vertical lobe features mark the insulating state. The resistive switch is visible at ~$E_\perp$=0.07 V/nm. Upon application of a large electric field, the system becomes more conductive. **b**, Band structure calculations of bilayer WTe_2 as a function of perpendicular electric field, showing the gap opening and closing upon application of an electric field. Reproduced from [39].

In 2019, Ma et. al. reported observation of the nonlinear Hall effect in bilayer WTe_2 [39]. As part of that work, they reported bad structure calculations under application of different values of perpendicular electric field, as reproduced in Figure 5.1b. Their calculations suggest that application of an electric field will open a gap between the conduction and valence bands, but upon increasing the strength of the field, the gap will close again. This seems to be consistent with our measurement here.

This device was made with crystals grown through the traditional self-flux growth method. We would like to make devices with higher-quality horizontal flux-grown crystals to establish the true nature of the bilayer state. While there have been no reports of superconductivity in bilayer to date, the dramatically different superconducting behavior observed in monolayer with the horizontal flux crystals raises the question of if bilayer can support it. Additionally, we would like to study the nature of the insulating state with higher quality crystals, attempting to reproduce the electric field dependence observed here, along with investigating potential signs of correlated behavior.

5.2 WTE$_2$ ON STRONTIUM TITANATE

We undertook the ambitious goal of coupling 2D materials to thin oxide films. The natural crystalline oxide to begin working with is $SrTiO_3$ (STO) (Figure 5.2a) which has the following assets: it is insulating; it is a standard MBE substrate for oxide films and is available in affordable, high-quality wafers; it can easily be treated to have a very high quality surface in ambient conditions; and it has already been shown to have a dramatic influence on a 2D van der Waals capping layer, most notably enhancing the T_c of $FeSe_2$ monolayers from 9 K to as high as 100 K [94], as well as possibly inducing a chiral edge modes in graphene acting through an intervening hBN layer [95]. Of its several notable properties, STO is most importantly a "quantum paraelectric" showing huge enhancement of its linear dielectric constant at low temperatures (Figure 5.2b) [96]. This is likely to modify electron-electron interactions, and therefore alter correlation effects, within a proximal 2D sheet. Hence, we set out to build and study 2D devices directly on an STO as a substrate, rather than using the standard SiO_2/Si wafers.

Using 0.5 mm-thick (100) STO (from Biotain Crystal Co.), we follow the following procedure [97]: anneal the substrate at 1000 °C in air, etch in water, then anneal again at 1000 °C in air. As seen by atomic force microscopy, the resulting surface shows atomic flatness over ~0.5 μm terraces with one-lattice-constant (0.4 nm) steps, shown in Figure 5.2c. Using electron-beam lithography followed by metal evaporation and lift-off we pattern metal contacts directly onto this surface, which remain smooth afterwards, as shown via AFM in Figure 5.2d. We also evaporate gold on the backside of the substrate for back gating, which is possible even through a very thick

STO substrate due to its large dielectric constant. We then transfer stacks of 2D materials onto these substrates using a standard polymer dry-transfer.

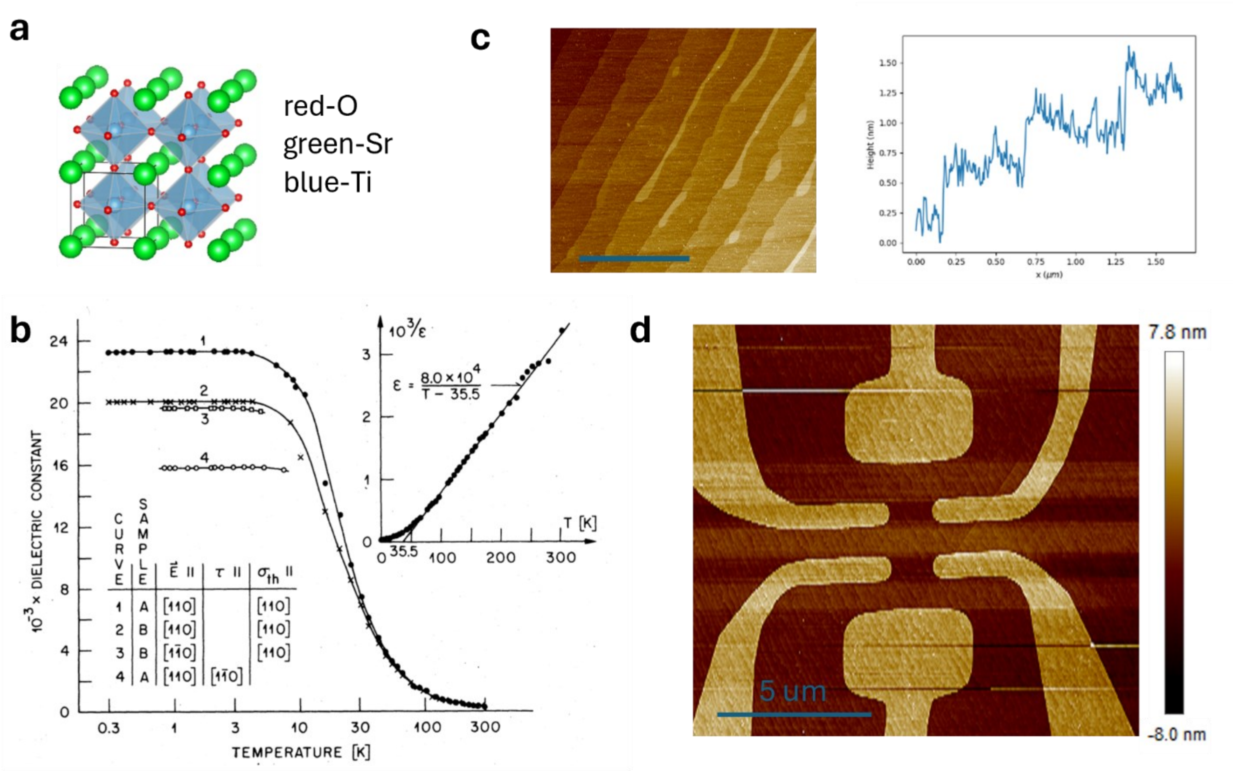

Figure 5.2. Strontium titanate **a**, SrTiO$_3$ crystal structure. **b**, Temperature dependence of the dielectric constant. Reproduced from [96]. **c**, Atomic force microscope image and line-trace of a prepared STO (100) surface. **d**, AFM image of 6-nm thick metal (Pt) electrodes patterned on the surface.

In Figure 5.3 we show results from our attempts to make WTe$_2$ devices on STO. Figure 5.3a shows an optical image of the top-gated WTe$_2$ device, with the flake outlined in red for clarity. In Figure 5.3b we show representative transport data from a dual-hBN-encapsulated WTe$_2$ device, while in Figure 5.3c we show gate dependence for WTe$_2$ on STO at a variety of temperatures. We notice a few features unique to the STO device. First, where in hBN encapsulated devices we observe an edge plateau that has a largely temperature-independence conductance value, on STO we observe edge plateaus forming that are highly temperature dependent. Additionally, the charge neutrality point seemingly drifts with temperature.

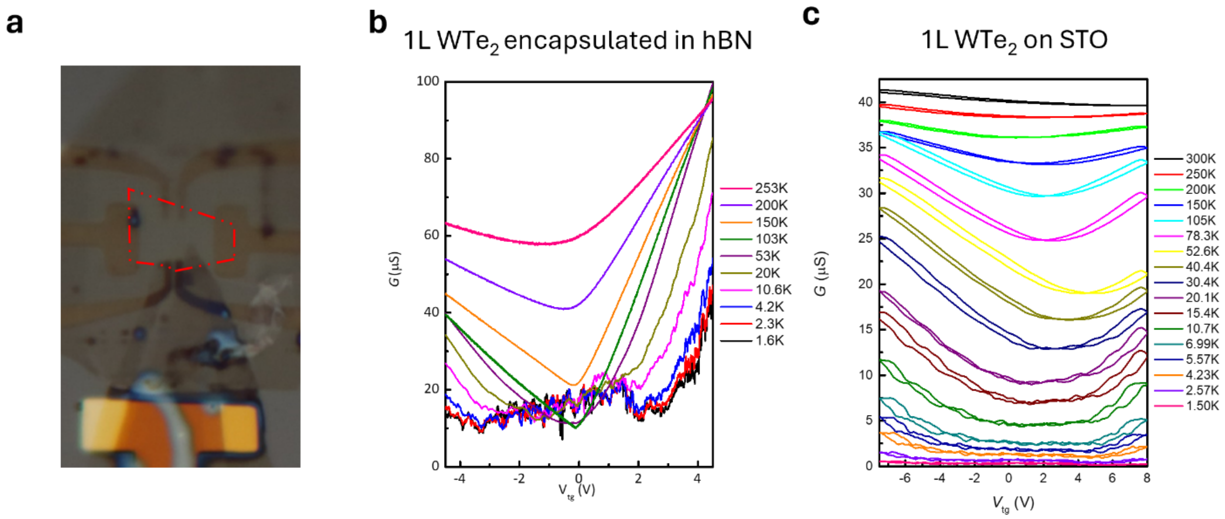

Figure 5.3. Monolayer WTe$_2$ on STO. **a**, Optical image of a 1L WTe$_2$/STO device. WTe$_2$ flake outlined in red. **b**, Two-terminal conductance of monolayer device MW2, fully encapsulating in hBN. **c**, Similar measurements on the STO substrate, where we observe an edge plateau that shows monotonic temperature dependence.

Figure 5.4 shows a bilayer WTe$_2$/STO device with similar layout. In natural bilayer form it is a 2D ferroelectric metal with an insulating state that appears near the charge-neutral point (Figure 5.4b). Remarkably, we see that in this device there is no such insulating state: it remains metallic down to 3.7 K (Figure 5.4c). One intriguing possibility is that the insulated state has a correlated nature and that dielectric screening by the STO reduces the correlations enough to destabilize this state.

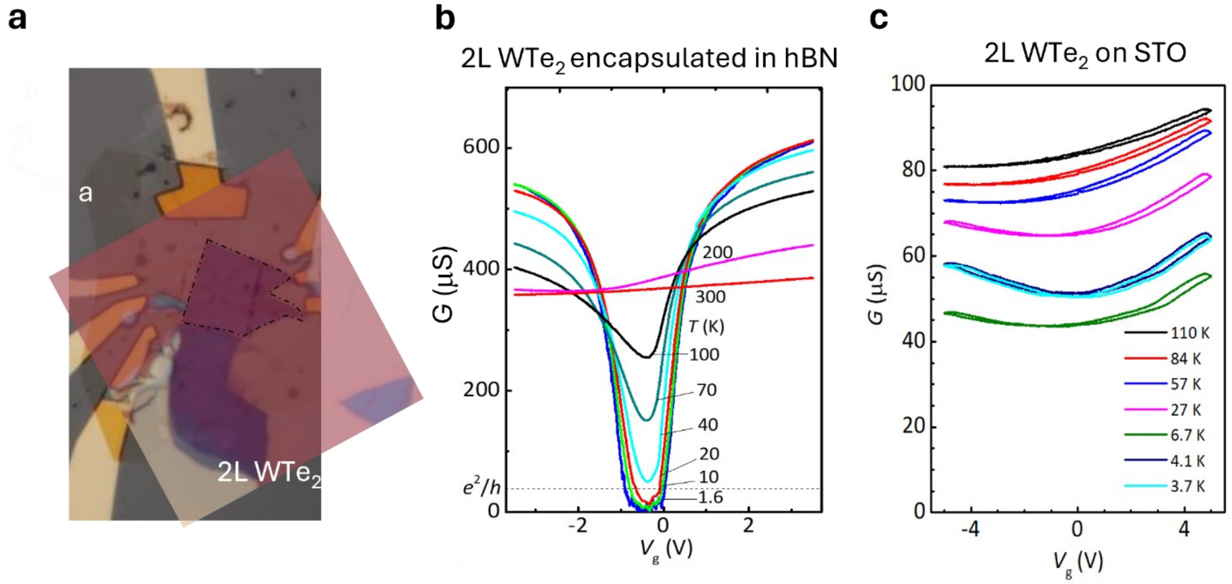

Figure 5.4. Bilayer WTe$_2$ on STO. **a**, Optical image of a 2L WTe$_2$/STO device. **b**, Two-terminal conductance of a normal 2L WTe$_2$ device, fully encapsulating in hBN. Reproduced from [43]. **c**, Similar measurements on the STO substrate, indicating that the insulating state at zero gate voltage has disappeared.

In summary, we have demonstrated that it is possible to make 2D devices strongly coupled to an unconventional oxide substrate and that dramatic alterations to their behavior result. This improves our position for systematically ascertaining the nature and consequences of the coupling in the case of STO to graphene, 2D semimetals, 2D superconductors and 2D magnets, and making similar devices on STO substrates with an MBE-added film having for example magnetic order.

BIBLIOGRAPHY

[1] S. M. Girvin and K. Yang, *Modern Condensed Matter Physics* (Cambridge University Press, Cambridge ; New York, NY, 2019).

[2] A. Y. Cho, *Film Deposition by Molecular-Beam Techniques*, Journal of Vacuum Science and Technology **8**, S31 (1971).

[3] S. M. Sze and K. K. Ng, *Physics of Semiconductor Devices*, 1st ed. (Wiley, 2006).

[4] V. Umansky, M. Heiblum, Y. Levinson, J. Smet, J. Nübler, and M. Dolev, *MBE Growth of Ultra-Low Disorder 2DEG with Mobility Exceeding 35×106cm2/Vs*, Journal of Crystal Growth **311**, 1658 (2009).

[5] A. Ohtomo and H. Y. Hwang, *A High-Mobility Electron Gas at the LaAlO3/SrTiO3 Heterointerface*, Nature **427**, 423 (2004).

[6] M. König, S. Wiedmann, C. Brüne, A. Roth, H. Buhmann, L. W. Molenkamp, X.-L. Qi, and S.-C. Zhang, *Quantum Spin Hall Insulator State in HgTe Quantum Wells*, Science **318**, 766 (2007).

[7] K. S. Novoselov, A. K. Geim, S. V. Morozov, D. Jiang, Y. Zhang, S. V. Dubonos, I. V. Grigorieva, and A. A. Firsov, *Electric Field Effect in Atomically Thin Carbon Films*, Science **306**, 666 (2004).

[8] P. J. Zomer, M. H. D. Guimarães, J. C. Brant, N. Tombros, and B. J. van Wees, *Fast Pick up Technique for High Quality Heterostructures of Bilayer Graphene and Hexagonal Boron Nitride*, Applied Physics Letters **105**, 013101 (2014).

[9] L. Wang et al., *One-Dimensional Electrical Contact to a Two-Dimensional Material*, Science **342**, 614 (2013).

[10] K. Watanabe, T. Taniguchi, and H. Kanda, *Direct-Bandgap Properties and Evidence for Ultraviolet Lasing of Hexagonal Boron Nitride Single Crystal*, Nature Mater **3**, 404 (2004).

[11] K. F. Mak, C. Lee, J. Hone, J. Shan, and T. F. Heinz, *Atomically Thin ${\mathrm{MoS}}_{2}$: A New Direct-Gap Semiconductor*, Phys. Rev. Lett. **105**, 136805 (2010).

[12] D. Xiao, G.-B. Liu, W. Feng, X. Xu, and W. Yao, *Coupled Spin and Valley Physics in Monolayers of ${\mathrm{MoS}}_{2}$ and Other Group-VI Dichalcogenides*, Phys. Rev. Lett. **108**, 196802 (2012).

[13] K. L. Seyler, P. Rivera, H. Yu, N. P. Wilson, E. L. Ray, D. G. Mandrus, J. Yan, W. Yao, and X. Xu, *Signatures of Moiré-Trapped Valley Excitons in MoSe2/WSe2 Heterobilayers*, Nature **567**, 66 (2019).

[14] Z. Y. Zhu, Y. C. Cheng, and U. Schwingenschlögl, *Giant Spin-Orbit-Induced Spin Splitting in Two-Dimensional Transition-Metal Dichalcogenide Semiconductors*, Phys. Rev. B **84**, 153402 (2011).

[15] P. Rivera, K. L. Seyler, H. Yu, J. R. Schaibley, J. Yan, D. G. Mandrus, W. Yao, and X. Xu, *Valley-Polarized Exciton Dynamics in a 2D Semiconductor Heterostructure*, Science **351**, 688 (2016).

[16] M. M. Ugeda et al., *Characterization of Collective Ground States in Single-Layer NbSe2*, Nature Phys **12**, 92 (2016).

[17] K. T. Law and P. A. Lee, *1T-TaS2 as a Quantum Spin Liquid*, Proceedings of the National Academy of Sciences **114**, 6996 (2017).

[18] Y. Nakata et al., *Robust Charge-Density Wave Strengthened by Electron Correlations in Monolayer 1T-TaSe2 and 1T-NbSe2*, Nat Commun **12**, 5873 (2021).

[19] B. Huang et al., *Layer-Dependent Ferromagnetism in a van Der Waals Crystal down to the Monolayer Limit*, Nature **546**, 270 (2017).
[20] Y. Deng et al., *Gate-Tunable Room-Temperature Ferromagnetism in Two-Dimensional Fe3GeTe2*, Nature **563**, 94 (2018).
[21] A. M. Kosevich, *Topology and Solid-State Physics (Review)*, Low Temperature Physics **30**, 97 (2004).
[22] C. L. Kane and E. J. Mele, *Z 2 Topological Order and the Quantum Spin Hall Effect*, Phys. Rev. Lett. **95**, 146802 (2005).
[23] C. L. Kane and E. J. Mele, *Quantum Spin Hall Effect in Graphene*, Phys. Rev. Lett. **95**, 226801 (2005).
[24] L. Fu and C. L. Kane, *Superconducting Proximity Effect and Majorana Fermions at the Surface of a Topological Insulator*, Phys. Rev. Lett. **100**, 096407 (2008).
[25] B. Lian, X.-Q. Sun, A. Vaezi, X.-L. Qi, and S.-C. Zhang, *Topological Quantum Computation Based on Chiral Majorana Fermions*, Proceedings of the National Academy of Sciences **115**, 10938 (2018).
[26] M. Ueta, H. Kanzaki, K. Kobayashi, Y. Toyozawa, and E. Hanamura, *Excitonic Processes in Solids*, Vol. 60 (Springer Berlin Heidelberg, Berlin, Heidelberg, 1986).
[27] L. V. Keldysh and Yu. V. Kopaev, *Possible Instability of the Semimetallic State toward Coulomb Interaction*, Soviet Physics, Solid State **6**, 2219 (1965).
[28] D. W. Snoke, *When Should We Say We Have Observed Bose Condensation of Excitons?*, Physica Status Solidi (b) **238**, 389 (2003).
[29] J. M. Blatt, K. W. Böer, and W. Brandt, *Bose-Einstein Condensation of Excitons*, Phys. Rev. **126**, 1691 (1962).
[30] B. Remez and N. R. Cooper, *Effects of Disorder on the Transport of Collective Modes in an Excitonic Condensate*, Phys. Rev. B **101**, 235129 (2020).
[31] W. Zhao, Electronic Transport of a 2D Quantum Material WTe2, Ph.D. Thesis, University of Washington, 2020.
[32] X. Qian, J. Liu, L. Fu, and J. Li, *Quantum Spin Hall Effect in Two-Dimensional Transition Metal Dichalcogenides*, Science **346**, 1344 (2014).
[33] S. Tang et al., *Quantum Spin Hall State in Monolayer 1T'-WTe2*, Nature Phys **13**, 683 (2017).
[34] I. Cucchi et al., *Microfocus Laser–Angle-Resolved Photoemission on Encapsulated Mono-, Bi-, and Few-Layer 1T'-WTe2*, Nano Lett. **19**, 554 (2019).
[35] P. Li, Y. Wen, X. He, Q. Zhang, C. Xia, Z.-M. Yu, S. A. Yang, Z. Zhu, H. N. Alshareef, and X.-X. Zhang, *Evidence for Topological Type-II Weyl Semimetal WTe2*, Nat Commun **8**, 2150 (2017).
[36] Y. Wu, D. Mou, N. H. Jo, K. Sun, L. Huang, S. L. Bud'ko, P. C. Canfield, and A. Kaminski, *Observation of Fermi Arcs in the Type-II Weyl Semimetal Candidate ${\mathrm{WTe}}_{2}$*, Phys. Rev. B **94**, 121113 (2016).
[37] F. Y. Bruno et al., *Observation of Large Topologically Trivial Fermi Arcs in the Candidate Type-II Weyl Semimetal $\mathrm{WT}{\mathrm{e}}_{2}$*, Phys. Rev. B **94**, 121112 (2016).
[38] M. N. Ali et al., *Large, Non-Saturating Magnetoresistance in WTe2*, Nature **514**, 205 (2014).
[39] Q. Ma et al., *Observation of the Nonlinear Hall Effect under Time Reversal Symmetric Conditions*, Nature **565**, 337 (2019).

[40] H. Wang and X. Qian, *Ferroelectric Nonlinear Anomalous Hall Effect in Few-Layer WTe2*, Npj Comput Mater **5**, 1 (2019).

[41] Y.-B. Choi et al., *Evidence of Higher-Order Topology in Multilayer WTe2 from Josephson Coupling through Anisotropic Hinge States*, Nat. Mater. **19**, 974 (2020).

[42] J. Lee, J. Kwon, E. Lee, J. Park, S. Cha, K. Watanabe, T. Taniguchi, M.-H. Jo, and H. Choi, *Spinful Hinge States in the Higher-Order Topological Insulators WTe2*, Nat Commun **14**, 1801 (2023).

[43] Z. Fei, T. Palomaki, S. Wu, W. Zhao, X. Cai, B. Sun, P. Nguyen, J. Finney, X. Xu, and D. H. Cobden, *Edge Conduction in Monolayer WTe2*, Nature Phys **13**, 677 (2017).

[44] S. Wu, V. Fatemi, Q. D. Gibson, K. Watanabe, T. Taniguchi, R. J. Cava, and P. Jarillo-Herrero, *Observation of the Quantum Spin Hall Effect up to 100 Kelvin in a Monolayer Crystal*, Science **359**, 76 (2018).

[45] V. Fatemi, S. Wu, Y. Cao, L. Bretheau, Q. D. Gibson, K. Watanabe, T. Taniguchi, R. J. Cava, and P. Jarillo-Herrero, *Electrically Tunable Low-Density Superconductivity in a Monolayer Topological Insulator*, Science **362**, 926 (2018).

[46] E. Sajadi, T. Palomaki, Z. Fei, W. Zhao, P. Bement, C. Olsen, S. Luescher, X. Xu, J. A. Folk, and D. H. Cobden, *Gate-Induced Superconductivity in a Monolayer Topological Insulator*, Science **362**, 922 (2018).

[47] T. Song et al., *Unconventional Superconducting Quantum Criticality in Monolayer WTe2*, Nat. Phys. **20**, 269 (2024).

[48] Y. Jia et al., *Evidence for a Monolayer Excitonic Insulator*, Nat. Phys. **18**, 87 (2022).

[49] B. Sun et al., *Evidence for Equilibrium Exciton Condensation in Monolayer WTe2*, Nat. Phys. **18**, 94 (2022).

[50] Z. Fei, W. Zhao, T. A. Palomaki, B. Sun, M. K. Miller, Z. Zhao, J. Yan, X. Xu, and D. H. Cobden, *Ferroelectric Switching of a Two-Dimensional Metal*, Nature **560**, 336 (2018).

[51] W. Zhao et al., *Determination of the Spin Axis in Quantum Spin Hall Insulator Candidate Monolayer WTe 2*, Phys. Rev. X **11**, 041034 (2021).

[52] Y. Chen, W. Zhao, E. Runburg, D. Cobden, and D. A. Pesin, *Magnetotransport on Quantum Spin Hall Edge Coupled to Bulk Midgap States*, Phys. Rev. B **108**, 085436 (2023).

[53] Y. Chen, G. Quaresima, W. Zhao, E. Runburg, D. Cobden, and D. A. Pesin, *Magnetochiral Anisotropy on a Quantum Spin Hall Edge*, (unpublished).

[54] Y.-T. Cui, E. Y. Ma, and Z.-X. Shen, *Quartz Tuning Fork Based Microwave Impedance Microscopy*, Review of Scientific Instruments **87**, 063711 (2016).

[55] Y. Shi et al., *Imaging Quantum Spin Hall Edges in Monolayer WTe $_2$*, Sci. Adv. **5**, eaat8799 (2019).

[56] M. Kim, S. Han, J. H. Kim, J.-U. Lee, Z. Lee, and H. Cheong, *Determination of the Thickness and Orientation of Few-Layer Tungsten Ditelluride Using Polarized Raman Spectroscopy*, 2D Mater. **3**, 034004 (2016).

[57] Y. Tokura and N. Nagaosa, *Nonreciprocal Responses from Non-Centrosymmetric Quantum Materials*, Nat Commun **9**, 3740 (2018).

[58] P. He, S. S.-L. Zhang, D. Zhu, Y. Liu, Y. Wang, J. Yu, G. Vignale, and H. Yang, *Bilinear Magnetoelectric Resistance as a Probe of Three-Dimensional Spin Texture in Topological Surface States*, Nature Phys **14**, 495 (2018).

[59] W. Zhao et al., *Magnetic Proximity and Nonreciprocal Current Switching in a Monolayer WTe2 Helical Edge*, Nat. Mater. **19**, 503 (2020).

[60] A. C. Balram, K. Flensberg, J. Paaske, and M. S. Rudner, *Current-Induced Gap Opening in Interacting Topological Insulator Surfaces*, Phys. Rev. Lett. **123**, 246803 (2019).

[61] C. Xu and J. E. Moore, *Stability of the Quantum Spin Hall Effect: Effects of Interactions, Disorder, and Z 2 Topology*, Phys. Rev. B **73**, 045322 (2006).

[62] P. Novelli, F. Taddei, A. K. Geim, and M. Polini, *Failure of Conductance Quantization in Two-Dimensional Topological Insulators Due to Nonmagnetic Impurities*, Phys. Rev. Lett. **122**, 016601 (2019).

[63] C.-H. Hsu, P. Stano, J. Klinovaja, and D. Loss, *Effects of Nuclear Spins on the Transport Properties of the Edge of Two-Dimensional Topological Insulators*, Phys. Rev. B **97**, 125432 (2018).

[64] B. L. Altshuler, I. L. Aleiner, and V. I. Yudson, *Localization at the Edge of a 2D Topological Insulator by Kondo Impurities with Random Anisotropies*, Phys. Rev. Lett. **111**, 086401 (2013).

[65] J. I. Väyrynen, M. Goldstein, Y. Gefen, and L. I. Glazman, *Resistance of Helical Edges Formed in a Semiconductor Heterostructure*, Phys. Rev. B **90**, 115309 (2014).

[66] L. Shi and J. C. W. Song, *Symmetry, Spin-Texture, and Tunable Quantum Geometry in a WTe 2 Monolayer*, Phys. Rev. B **99**, 035403 (2019).

[67] Y.-M. Xie, B. T. Zhou, and K. T. Law, *Spin-Orbit-Parity-Coupled Superconductivity in Topological Monolayer WTe 2*, Phys. Rev. Lett. **125**, 107001 (2020).

[68] A. Arora, L. Shi, and J. C. W. Song, *Cooperative Orbital Moments and Edge Magnetoresistance in Monolayer W Te 2*, Phys. Rev. B **102**, 161402 (2020).

[69] J. H. Garcia, M. Vila, C.-H. Hsu, X. Waintal, V. M. Pereira, and S. Roche, *Canted Persistent Spin Texture and Quantum Spin Hall Effect in WTe 2*, Phys. Rev. Lett. **125**, 256603 (2020).

[70] L. Muechler, A. Alexandradinata, T. Neupert, and R. Car, *Topological Nonsymmorphic Metals from Band Inversion*, Phys. Rev. X **6**, 041069 (2016).

[71] D.-H. Choe, H.-J. Sung, and K. J. Chang, *Understanding Topological Phase Transition in Monolayer Transition Metal Dichalcogenides*, Phys. Rev. B **93**, 125109 (2016).

[72] X. Lin and J. Ni, *Topological Phase Transition Due to Strain-Controlled Evolution of the Inverted Bands in 1 T ′ − M X 2*, Phys. Rev. B **95**, 245436 (2017).

[73] A. Lau, R. Ray, D. Varjas, and A. R. Akhmerov, *Influence of Lattice Termination on the Edge States of the Quantum Spin Hall Insulator Monolayer 1 T ′ − WTe 2*, Phys. Rev. Materials **3**, 054206 (2019).

[74] F. D. M. Haldane, *Model for a Quantum Hall Effect without Landau Levels: Condensed-Matter Realization of the "Parity Anomaly,"* Phys. Rev. Lett. **61**, 2015 (1988).

[75] T. Morimoto and N. Nagaosa, *Nonreciprocal Current from Electron Interactions in Noncentrosymmetric Crystals: Roles of Time Reversal Symmetry and Dissipation*, Sci Rep **8**, 2973 (2018).

[76] D. Xiao, M.-C. Chang, and Q. Niu, *Berry Phase Effects on Electronic Properties*, Rev. Mod. Phys. **82**, 1959 (2010).

[77] F. Lüpke, D. Waters, S. C. de la Barrera, M. Widom, D. G. Mandrus, J. Yan, R. M. Feenstra, and B. M. Hunt, *Proximity-Induced Superconducting Gap in the Quantum Spin Hall Edge State of Monolayer WTe2*, Nat. Phys. **16**, 526 (2020).

[78] D. Elwell, *Fundamentals of Flux Growth*, in *Crystal Growth in Science and Technology*, edited by H. Arend and J. Hulliger, Vol. 210 (Springer US, Boston, MA, 1989), pp. 133–142.

[79] T. B. Massalski, H. Okamoto, and ASM International, editors , *Binary Alloy Phase Diagrams*, 2nd ed (ASM International, Materials Park, Ohio, 1990).

[80] J.-Q. Yan, B. C. Sales, M. A. Susner, and M. A. McGuire, *Flux Growth in a Horizontal Configuration: An Analog to Vapor Transport Growth*, Phys. Rev. Mater. **1**, 023402 (2017).

[81] A. Jindal et al., *Coupled Ferroelectricity and Superconductivity in Bilayer Td-MoTe2*, Nature **613**, 7942 (2023).

[82] D. A. Rhodes et al., *Enhanced Superconductivity in Monolayer* T $_d$ *-MoTe* $_2$, Nano Lett. **21**, 2505 (2021).

[83] F. Tang, P. Wang, Q. Wang, Y. Gan, J. Lyu, X. Mi, M. He, L. Zhang, and J. H. Smet, *Ambipolar Superconductivity with Strong Pairing Interaction in Monolayer 1T'-MoTe2*, Nano Lett. **23**, 7516 (2023).

[84] Y. Cao, V. Fatemi, S. Fang, K. Watanabe, T. Taniguchi, E. Kaxiras, and P. Jarillo-Herrero, *Unconventional Superconductivity in Magic-Angle Graphene Superlattices*, Nature **556**, 43 (2018).

[85] H. Zhou, L. Holleis, Y. Saito, L. Cohen, W. Huynh, C. L. Patterson, F. Yang, T. Taniguchi, K. Watanabe, and A. F. Young, *Isospin Magnetism and Spin-Polarized Superconductivity in Bernal Bilayer Graphene*, Science **375**, 774 (2022).

[86] C. Li et al., *Tunable Superconductivity in Electron- and Hole-Doped Bernal Bilayer Graphene*, Nature 1 (2024).

[87] W. Shi, J. Ye, Y. Zhang, R. Suzuki, M. Yoshida, J. Miyazaki, N. Inoue, Y. Saito, and Y. Iwasa, *Superconductivity Series in Transition Metal Dichalcogenides by Ionic Gating*, Sci Rep **5**, 12534 (2015).

[88] D. Costanzo, S. Jo, H. Berger, and A. F. Morpurgo, *Gate-Induced Superconductivity in Atomically Thin MoS2 Crystals*, Nature Nanotech **11**, 339 (2016).

[89] J. M. Lu, O. Zheliuk, I. Leermakers, N. F. Q. Yuan, U. Zeitler, K. T. Law, and J. T. Ye, *Evidence for Two-Dimensional Ising Superconductivity in Gated MoS2*, Science **350**, 1353 (2015).

[90] M. Tinkham, *Introduction to Superconductivity*, 2 ed (Dover Publ, Mineola, NY, 2015).

[91] P. Wang et al., *Landau Quantization and Highly Mobile Fermions in an Insulator*, Nature **589**, 225 (2021).

[92] J. Zhu, T. Li, A. F. Young, J. Shan, and K. F. Mak, *Quantum Oscillations in Two-Dimensional Insulators Induced by Graphite Gates*, Phys. Rev. Lett. **127**, 247702 (2021).

[93] D. Shcherbakov et al., *Layer- and Gate-Tunable Spin-Orbit Coupling in a High-Mobility Few-Layer Semiconductor*, Science Advances **7**, eabe2892 (2021).

[94] J.-F. Ge, Z.-L. Liu, C. Liu, C.-L. Gao, D. Qian, Q.-K. Xue, Y. Liu, and J.-F. Jia, *Superconductivity above 100 K in Single-Layer FeSe Films on Doped SrTiO3*, Nature Mater **14**, 285 (2015).

[95] L. Veyrat et al., *Helical Quantum Hall Phase in Graphene on SrTiO3*, Science **367**, 781 (2020).

[96] K. A. Müller and H. Burkard, *SrTi O 3 : An Intrinsic Quantum Paraelectric below 4 K*, Phys. Rev. B **19**, 3593 (1979).

[97] J. G. Connell, B. J. Isaac, G. B. Ekanayake, D. R. Strachan, and S. S. A. Seo, *Preparation of Atomically Flat SrTiO3 Surfaces Using a Deionized-Water Leaching and Thermal Annealing Procedure*, Applied Physics Letters **101**, 251607 (2012).

VITA

Elliott was born in Chicago Heights, Illinois, to Gregg Runburg and Jan Bonavia. He was raised in a loving home in the south suburbs of Chicago, attending Homewood-Flossmoor Community High School, before matriculating to the University of Notre Dame. He graduated from there in 2017 with his Bachelors of Science with a double major in physics and math. In Fall of 2017, he moved to Seattle to start his Ph.D. program at the University of Washington, where he quickly joined Prof. David Cobden’s 2D materials lab, where he’d remain for his 7 year graduate school journey.